Masterarbeit
Zur Erlangung des akademischen Grades Master of Science

Effects of Exchange-Correlation Functionals on Magnetic Properties of Cobalt and La_2CuO_4 in an All-Electron Framework

eingereicht von: Fabian Calogero Nemitz

Gutachter/innen: Prof. Dr. Dr. h.c. Claudia Draxl
PD Dr. Denis Usvyat

Eingereicht am Institut für Physik der Humboldt-Universität zu Berlin am:

22.07.2025

Abstract

An investigation of exchange-correlation functionals applied to ferromagnetic cobalt and antiferromagnetic pristine La_2CuO_4 is presented. LSDA, GGA, mGGA, and hybrid functionals are benchmarked based on their predictions on the magnetic structure of the systems, with a focus on the results of the full-potential all-electron code `exciting`. The mGGA and HSE functionals are shown to increase magnetization in both systems when compared to semi-local functionals. The magnetization in cobalt is overestimated with respect to the PBE result of $1.65\,\mu_B$, which agrees with experiment. For La_2CuO_4, the SCAN functional is found to give experimental results of the band gap 1.08 eV and copper magnetic moments $0.54\,\mu_B$ while stabilizing the antiferromagnetic phase. Computational methods of magnetic systems are outlined and an extension to hybrid-functionals calculations in `exciting` is proposed.

Contents

List of Abbreviations

LCO	La_2CuO_4
Co	(Bulk) Cobalt
DFT	Density Functional Theory
KS	Kohn-Sham
XC	Exchange-Correlation
SCF	Self-Consistent Field (Cycle)
BZ	Brillouin Zone
(L)APW(+lo)	(Linearized) Augmented Plane Waves (+ Local Orbitals)
MT	Muffin Tin (Sphere)
I	Intersititial (Region)
SOC	Spin-Orbit Coupling
FV / SV	First / Second Variation
LSDA	Local Spin-Density Approximation
GGA	Generalized Gradient Approximation
fcc	Face-centered cubic
NM / FM / AFM	Non-, Ferro-, Antiferromagnetic
EoS	Equation of State
DoS	Density of States
HTT	High-Temperature Tetragonal (Phase of LCO)
LTO	Low-Temperature Orthorombic (Phase of LCO)
VBM	Valence-Band Maximimum
CBM	Conduction-Band Minimum
MPB	Mixed-Product Basis

Introduction

In 1986 J.G. Bednorz and K.A. Müller published their findings [1] about the existence of a superconducting phase in, later specified to be, $La_{2-x}Ba_xCuO_4$. Remarkable about this discovery was the for the time, high critical temperature T_C of 30 K. This discovery led to the search for similar materials, which are now known as *cuprate* superconductors. Modern cuprate compounds can have critical temperatures up to $T_C \approx 164$ K [2]. Cuprates are considered unconventional superconductors, meaning that the theory proposed by J. Bardeen, L. Cooper and J.R. Schrieffer [3] is not suitable for describing their superconducting mechanism. Further, the superconducting phase emerges only under hole-doping of the parent compound, *i.e.*, La_2CuO_4 (LCO), which induces an insulator-to-metal transition [4]. Due to this, these materials have been of special interest for theoretical solid-state physics and, specifically, density-functional theory (DFT) [5]. This work represents a study of the insulating, undoped ground-state structure of LCO using Kohn-Sham DFT [6]. This study is put into the picture of the exchange-correlation (XC) functionals within DFT and their distinctive features. The antiferromagnetic ground state of LCO has historically been a particularly difficult system for functionals depending only on the electronic density and its gradient (LDA, GGA) [7–9], and modern orbital-based functionals (meta-GGA, hybrid) offer improvement. Mainly used for calculations, is the `exciting` open-source software package [10], a full-potential all-electron code, which allows for high-precision benchmark results. The meta-GGA functionals were, however, only recently implemented in this DFT code [11]. The implementation has thus not been applied to a complex material like LCO, and to ensure the robustness and accuracy of the findings achieved with meta-GGA functionals in `exciting`, the licensed all-electron code `FHI-aims` is used for cross-validation.

LCO is not the only material of interest in this work. Preceding its investigation is the study of the ferromagnetic metal cobalt. By first analyzing the well-characterized [12, 13] cobalt and the effects of the various functionals

on its magnetic and electronic properties, a baseline for the comparison of the functionals can be set. Elemental cobalt is generally classified as an itinerant ferromagnet, where the magnetic moment arises from delocalized $3d$ electrons [14] and is well understood within a band picture. Comparing the starkly contrasting nature of cobalt with the strongly-correlated LCO then allows for broader arguments about the nature of exchange-correlation effects on magnetic materials.

The thesis is structured as follows: Chapter 1 outlines the theoretical background necessary for the arguments of the later chapters, defining and introducing key concepts and computational parameters for the study of magnetic materials using Kohn-Sham DFT. In the following Chapter 2, cobalt is studied, both through the computational lens of a comparison between the `exciting` code with other DFT packages, and the physical lens of density-functional approximations. The computational methodology of the work is showcased in this chapter, and is applied similarly in the study of LCO. These are split into two chapters due to the level of details included. Chapter 3 first deals with ground-state calculations of the material performed using the generalized gradient approximation. The practical details are examined more closely, and the nonmagnetic and antiferromagnetic ground states are investigated separately. The relevant physical aspects, as well as comparison to literature, are the focus of Chapter 4. The functionals are ordered in accordance with the metaphorical "Jacob's ladder" [15], which orders the presented results into the broader framework of DFT literature.

Chapter 1

Theoretical Background

This chapter introduces the theoretical framework underlying this work. To begin, density-functional theory (DFT) and its application to bulk solids and their ground-state electronic structure is introduced. As computations are the main focus, the fundamentals of the basis functions implemented in the used software-packages are outlined. Of special importance are magnetic systems, therefore spin-polarized DFT and its methods are thoroughly summarized with a focus on computational aspects. At the core of both DFT and this work lies the *exchange-correlation energy functional*. The approximations of interest to this functional are introduced and their relevant properties highlighted. Unless stated otherwise, atomic units are used throughout this chapter.

1.1 Basics of density-functional theory

Solid materials can be modeled as periodic crystal structures composed of N electrons and N_n nuclei. To describe such systems in quantum mechanics, one has to solve the many-body Schrödinger equation

$$\hat{H}\,\Psi\big(\mathcal{R}_\mathrm{e},\mathcal{R}_\mathrm{n}\big) = E\,\Psi\big(\mathcal{R}_\mathrm{e},\mathcal{R}_\mathrm{n}\big)\ , \tag{1.1.1}$$

for the wave function of the crystal, Ψ. It depends on both the electronic $\mathcal{R}_\mathrm{e} = \{\mathbf{r}_1,\mathbf{r}_2,\ldots,\mathbf{r}_N\}$ and nuclear configurations $\mathcal{R}_\mathrm{n} = (\mathbf{R}_1,\mathbf{R}_2,...,\mathbf{R}_{N_\mathrm{n}})$. The exponential increase in computational complexity with system size renders a direct solution of the Schrödinger equation intractable, both numerically [16] and analytically. To simplify the situation, the Born-Oppenheimer approximation [17] is commonly employed. It assumes that, due to the large difference in mass of the nuclei and electrons, their wave functions may be treated

separately. The result is a purely electronic problem that can be solved by using DFT. The DFT approach is based on the *Hohenberg-Kohn theorems* [5]. The main result of the first theorem is that the ground-state electronic energy, E_{GS}, is a functional of the ground-state electron density, $\rho_{\mathrm{GS}}(\mathbf{r})$. The second theorem states that the functional $E_{\mathrm{GS}}[\rho]$ is minimized by $\rho_{\mathrm{GS}}(\mathbf{r})$. This reduces the complexity of the many-body electronic problem to a description involving only the electronic density, which depends only on three spatial variables. In order to simplify the notation, the label GS is omitted in the following.

The ground-state energy functional can be separated into two different contributions:

$$E \equiv E[\rho] = F[\rho] + \int v_{\mathrm{ext}}(\mathbf{r})\, \rho(\mathbf{r})\, \mathrm{d}\mathbf{r}\,. \tag{1.1.2}$$

Here, F is a universal functional of ρ. Additionally, $v_{\mathrm{ext}}(\mathbf{r})$ is the external potential, mostly consisting of, but not limited to, the Coulomb potential between one electron at $\mathbf{r}$ and all nuclei. Even though the first Hohenberg-Kohn theorem proves the existence of the functional $F[\rho]$, the exact form of this functional is unknown.

As the second Hohenberg-Kohn theorem states, the ground-state density is the one which minimizes the ground-state energy functional under the constraint that the integral of the density reproduces the number of electrons, N. Then, with μ being the chemical potential, this leads to the requirement:

$$\delta\big(E[\rho] - \mu\, N\big) \stackrel{!}{=} 0\,. \tag{1.1.3}$$

To minimize the (ground-state) energy functional in Eq. (1.1.2), a suitable approximation for the universal functional $F[\rho]$ is needed. Towards this end, the approach outlined by Kohn and Sham [6] is followed.

1.1.1 Kohn-Sham-DFT

In the Kohn-Sham (KS) approach to DFT, an auxiliary, non-interacting, electron system (consisting of KS electrons) is introduced. The ground-state electron density of the auxiliary system is assumed to be identical to the one of the actual interacting electron system. In KS DFT, the ground-state electron density can be expressed in terms of the so-called *Kohn-Sham orbitals* $\{\varphi_i(\mathbf{r})\}$:

$$\rho(\mathbf{r}) = \sum_{i}^{N} |\varphi_i(\mathbf{r})|^2\,. \tag{1.1.4}$$

A common expansion of the ground-state energy functional in this framework looks as follows [18]:

$$E[\rho] = T_0[\rho] + E_{\mathrm{H}}[\rho] + E_{\mathrm{xc}}[\rho] + \int v_{\mathrm{ext}}(\mathbf{r})\,\rho(\mathbf{r})\,\mathrm{d}\mathbf{r}\,. \tag{1.1.5}$$

Here, $T_0[\rho]$ is the kinetic-energy functional of the system of KS-electrons with density $\rho(\mathbf{r})$ and $E_{\mathrm{H}}[\rho]$ is the so-called *Hartree energy*, defined as

$$E_{\mathrm{H}}[\rho] = \frac{1}{2}\int \frac{\rho(\mathbf{r})\,\rho(\mathbf{r}')}{|\mathbf{r}-\mathbf{r}'|}\,\mathrm{d}\mathbf{r}\mathrm{d}\mathbf{r}'\,, \tag{1.1.6}$$

which can be understood as the energy contribution corresponding to the classical Coulomb interaction between the electron densities. Notably, this includes the spurious interaction of an electron with itself. $E_{\mathrm{xc}}[\rho]$ denotes the unknown *exchange-correlation* energy functional. This energy functional has no classical counterpart and exists due to purely quantum-mechanical interactions of the many-electron system such as the Pauli-exchange energy. This energy can be further decomposed into an exchange and a correlation contribution, thus, $E_{\mathrm{xc}} = E_{\mathrm{x}} + E_{\mathrm{c}}$.

The minimization of the energy functional leads to the *KS equations* for the KS orbitals, with $\{\epsilon_i\}$ as the KS eigenvalues:

$$\Bigg\{ -\frac{1}{2}\nabla^2 + \underbrace{v_{\mathrm{ext}}(\mathbf{r}) + \int \frac{\rho(\mathbf{r}')}{|\mathbf{r}-\mathbf{r}'|}\,\mathrm{d}\mathbf{r}' + v_{\mathrm{xc}}(\mathbf{r},[\rho])}_{v_{\mathrm{eff}}(\mathbf{r},[\rho])} \Bigg\}\varphi_i(\mathbf{r}) \equiv \hat{H}_{\mathrm{KS}}\,\varphi_i(\mathbf{r}) = \epsilon_i\,\varphi_i(\mathbf{r})\,, \tag{1.1.7}$$

where

$$v_{\mathrm{xc}}(\mathbf{r},[\rho]) := \frac{\delta E_{\mathrm{xc}}[\rho]}{\delta\rho(\mathbf{r})}\,, \tag{1.1.8}$$

and the KS Hamiltonian is defined as:

$$\hat{H}_{\mathrm{KS}} = -\frac{1}{2}\nabla^2 + v_{\mathrm{eff}}(\mathbf{r},[\rho])\,. \tag{1.1.9}$$

This procedure turns the many-body problem of minimizing the functional in Eq. (1.1.5) into a series of single-particle equations. It is important to note that the effective potential $v_{\mathrm{eff}}(\mathbf{r},[\rho])$ itself depends on the density. Simultaneously, the potential determines the orbitals and, thus, the density. Therefore, these equations need to be solved *self-consistently*. Starting from an approximate initial density $\rho_{\mathrm{init}}(\mathbf{r})$, one calculates the potential from it and then solves Eq. (1.1.7). The resulting Kohn-Sham orbitals are then used to generate a new

density and potential, and so on. This continues, until the change between consecutive iterations in resulting energy, potential, charge distribution, or other chosen convergence criteria, reaches some predefined convergence criterion. More stable and faster calculations can be achieved by an appropriate choice of $\rho_{\text{init}}(\mathbf{r})$, as well as optimizing the *self-consistent field* (SCF) cycle, *e.g.*, by mixing several previous iterations of the density to generate the new one.

1.1.2 DFT for periodic crystals

In this work, exclusively bulk materials are studied. Consequently, the discrete quantum number (i) has to be replaced by $(n\mathbf{k})$, describing the band index n and the wave vector $\mathbf{k}$. As a consequence of Bloch's theorem [19], the first Brillouin zone (BZ) suffices as the domain of $\mathbf{k}$-values. Then, the explicit calculation of the ground-state energy and density requires an integration over the wave vectors. This integration is typically approximated by a finite sum over a suitably dense grid of $\mathbf{k}$-points in the first BZ. Symmetry considerations reduce the necessary number of $\mathbf{k}$-points. For instance, the expression of the density becomes:

$$\rho(\mathbf{r}) = \sum_{n}^{\infty} \sum_{\mathbf{k}}^{\text{BZ}} w_{\mathbf{k}} \left|\varphi_{n\mathbf{k}}(\mathbf{r})\right|^2 , \tag{1.1.10}$$

where $w_{\mathbf{k}}$ are the weight factors of the $\mathbf{k}$-point. For simplicity, these weights will be omitted from following expressions.

1.2 Basis functions

An important part in numerical DFT calculations is the expansion in suitable basis functions. Finite computational resources naturally demand austerity in the number of basis function used to describe the wave functions, potential, and density. A major challenge when describing solids is that the wave functions must be expanded into a basis set suitable for both the strongly bound electrons and the valence electrons which are only weakly bound. Core electrons are typically treated separately from the valence electrons. This section, therefore, focuses on the valence problem.

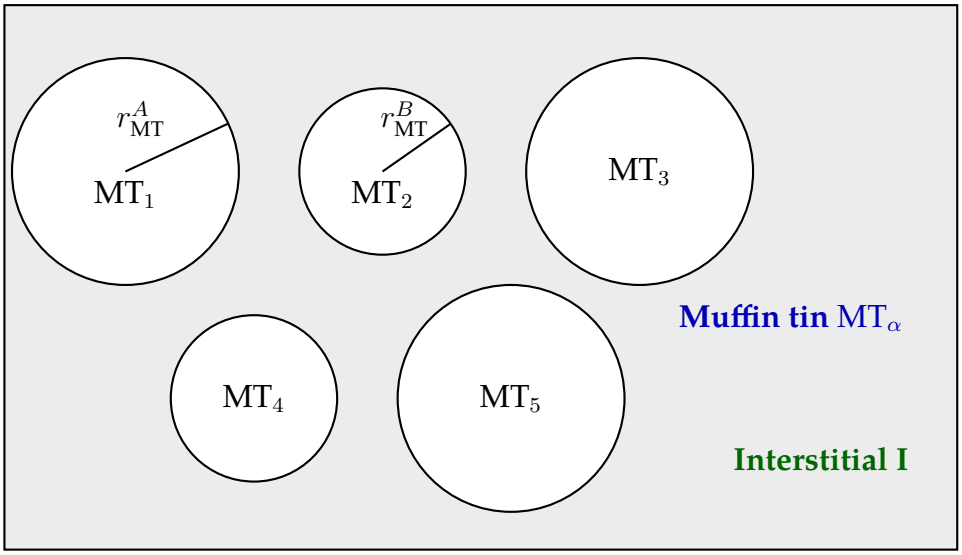

Figure 1.1: Partition of space into muffin-tin spheres MT_α of species A and species B with corresponding muffin-tin radii r^A_{MT} and r^B_{MT}. The shaded region represents the interstitial region I.

1.2.1 The LAPW+lo scheme

Of special importance is the linearized augmented plane wave (LAPW) + local orbitals (lo) method [20–22]. While plane waves are ideal for describing delocalized valence electrons in periodic systems, they fail to efficiently capture the rapidly varying behavior near nuclei, motivating the use of mixed basis sets which includes also atomic-like orbitals. A core principle is the separation of space into the so-called *muffin-tin* spheres (MT_α) centered around the atoms $\mathbf{R}_\alpha$, with the remaining space being called the interstitial region (I). This division of space is illustrated in Figure 1.1.

Explicitly, the wave function is expanded over reciprocal lattice vectors $\mathbf{G}$ into the augmented plane waves [10, 23]:

$$\varphi_{n\mathbf{k}}(\mathbf{r}) = \sum_{\mathbf{G}} C_{n\mathbf{k}}\, \phi_{\mathbf{G}+\mathbf{k}}(\mathbf{r})\,, \tag{1.2.1}$$

with the augmented plane wave (APW) functions $\phi_{\mathbf{G}+\mathbf{k}}(\mathbf{r})$

$$\phi_{\mathbf{G}+\mathbf{k}}(\mathbf{r}) := \begin{cases} \sum_{lm} A^{lm\alpha}_{\mathbf{G}+\mathbf{k}}\, u_{l\alpha}(r_\alpha)\, Y_{lm}(\hat{\mathbf{r}}_\alpha), & \mathbf{r} \in \mathrm{MT}_\alpha \\ \frac{1}{\sqrt{\Omega}}\, \mathrm{e}^{\mathrm{i}(\mathbf{G}+\mathbf{k})\cdot\mathbf{r}}, & \mathbf{r} \in \mathrm{I}\,. \end{cases} \tag{1.2.2}$$

The basis functions are expanded inside the muffin-tin sphere into radial functions and spherical harmonics. In the interstitial region the basis functions are

plane waves. The unit-cell volume is denoted by Ω, $\mathbf{r}_\alpha := \mathbf{r} - \mathbf{R}_\alpha$ is the relative position within the MT region, and $\hat{\mathbf{r}}_\alpha = \mathbf{r}_\alpha / r_\alpha$ is the radial unit vector. The continuity of the functions at the MT boundary is enforced by the coefficients $A^{lm\alpha}_{\mathbf{G}+\mathbf{k}}$. As they are generally not orthogonal, for computations the overlap matrix S will become necessary:

$$S_{\mathbf{G}\mathbf{G}'}(\mathbf{k}) := \langle \phi_{\mathbf{G}+\mathbf{k}} | \phi_{\mathbf{G}'+\mathbf{k}} \rangle \,. \tag{1.2.3}$$

A closer look at the radial functions $v_{l\alpha}(r_\alpha)$ reveals a problem of the APW basis set. The radial functions are given as solutions of the Schrödinger equation in the spherical symmetric part of the effective potential:

$$\left\{ -\frac{\partial^2}{\partial r_\alpha^2} + \frac{l(l+1)}{r_\alpha^2} + v_{\text{eff}}(r_\alpha) - \epsilon_{nl\mathbf{k}} \right\} r_\alpha \, u_{l\alpha}(r_\alpha) = 0 \,. \tag{1.2.4}$$

As can be seen, the energies are needed to obtain the radial functions, which are themselves needed to solve the KS equations for those energies, yielding a nonlinear problem.

In the linearized APW (LAPW) set, the energies in Eq. (1.2.4) are changed to be *parameters* $\epsilon_{l\alpha}$. To compensate this, one expands the radial functions around these stationary band energies up to first order [18]. This ultimately modifies the basis functions to:

$$\phi_{\mathbf{G}+\mathbf{k}}(\mathbf{r}) = \begin{cases} \sum_{lm} [A^{lm\alpha}_{\mathbf{G}+\mathbf{k},lm} \, u_{l\alpha}(r_\alpha, \epsilon_{l\alpha}) + B^{lm\alpha}_{\mathbf{G}+\mathbf{k}} \, \dot{u}_{l\alpha}(r_\alpha, \epsilon_{l\alpha})] \, Y_{lm}(\hat{\mathbf{r}}_\alpha) \,, & \mathbf{r} \in \mathrm{MT}_\alpha \\ \frac{1}{\sqrt{\Omega}} \, \mathrm{e}^{\mathrm{i}(\mathbf{G}+\mathbf{k})\cdot\mathbf{r}} \,, & \mathbf{r} \in \mathrm{I} \,. \end{cases} \tag{1.2.5}$$

The coefficients $B^{\alpha}_{\mathbf{G}+\mathbf{k},lm}$ ensure its smoothness at the MT boundary.

Instead of this linearization, physically important local orbitals may be added explicitly to the basis set. A local orbital is of the form

$$\phi_{\mu\alpha}(\mathbf{r}) = \begin{cases} [a_\mu \, u_{l\alpha}(r_\alpha) + b_\mu \, \dot{u}_{l\alpha}(r_\alpha)] \, Y_{lm}(\hat{\mathbf{r}}_\alpha) \,, & \mathbf{r} \in \mathrm{MT}_\alpha \\ 0 \,, & \mathbf{r} \in \mathrm{I} \,, \end{cases} \tag{1.2.6}$$

and is only nonzero for a specific atom. The linearization energies are fixed parameters. These local orbitals then introduce sufficient variational freedom that was lost when the energies were assumed to be fixed. Furthermore, these local orbitals are well suited for the semi-core states within the MT region.

It is important to highlight the newly introduced parameters and their importance for DFT calculations using this basis set. One immediate parameter is the radius of the muffin tin spheres around the atoms, R_{MT}. As summations as in Eq. (1.2.1) have to be finite, a cutoff, G_{max}, is needed. It restricts the reciprocal lattice vectors through $|\mathbf{G}+\mathbf{k}| < G_{\mathrm{max}}$. A smaller MT region means that more plane waves are needed in the interstitial region. Therefore the two previous parameters can be combined into one product $R_{\mathrm{MT}}\, G_{\mathrm{max}}$. Crucial for an accurate calculation is the inclusion of necessary local orbitals $\phi_{\mu\alpha}(\mathbf{r})$ for each atom, in practice for each element, in the calculation. The choice of suitable linearization energies is non-trivial and methodology may differ between different implementations, calculated quantity, and level of precision.

For this work highly relevant is the **exciting** open source code [10]. It uses the (L)APW(+lo) basis, which is to be understood as a combination of the above introduced APW+lo and LAPW sets, for simplicity from now on just called the LAPW+lo basis. Typically, **exciting** is used for high precision calculations on which other, more efficient methods may be benchmarked. Within **exciting**, core electrons are treated fully relativistically via the Dirac equation. In **exciting** the potential and density in the interstitial region have a separate plane-wave cutoff, here called G_{maxVR}.

1.2.2 Numeric atom-centered orbitals

This basis set circumvents the challenges associated with the radial functions by referring to numerically tabulated values for the function. Through this, the atom-like functions of the muffin tin spheres used previously are now extended to the entire unit cell. The basis functions take the form [24]:

$$\phi_{ilm}(\mathbf{r}) = \frac{u_i(r)}{r}\, Y_{lm}(\hat{\mathbf{r}})\,. \tag{1.2.7}$$

Additionally, the orbitals may be further restricted in their extension in space through a cutoff potential. This methodology can allow for a great level of flexibility in customizing the basis set to each type of atom specifically, as well as very good scalability for larger unit cells and number of atoms. However, it relies on accurate values for the radial functions and also demands exactly that great level of customization to each atom for accurate results. The licensed code **FHI-aims** [24] implements this numerical atomic orbital basis set. It can provide a high level of precision [25–27] and is mainly used as a benchmark for **exciting** in this work.

1.3 Spin-polarized DFT

This section introduces the necessary tools to describe solids with non-trivial spin structure within DFT. A distinction is made between collinearly and non-collinearly aligned spins. Furthermore, the interaction of the solid with an external magnetic field is included. The computational aspects of the collinear approximation are highlighted, with a focus on the `exciting` code.

1.3.1 Non-collinear spins

For a general spin alignment, the single-particle KS orbitals need to be expressed as Dirac spinors:

$$\underline{\varphi}_{n\mathbf{k}}(\mathbf{r}) = \begin{pmatrix} \alpha_{n\mathbf{k}}(\mathbf{r}) \\ \beta_{n\mathbf{k}}(\mathbf{r}) \end{pmatrix}, \qquad \rho(\mathbf{r}) = \sum_{n}^{N} \sum_{\mathbf{k}}^{\mathrm{BZ}} \underline{\varphi}^{\dagger}_{n\mathbf{k}}(\mathbf{r})\, \underline{\varphi}_{n\mathbf{k}}(\mathbf{r}) \,. \tag{1.3.1}$$

An important quantity for the description of spin-polarized systems is the *magnetization density*, defined as:

$$\mathbf{m}(\mathbf{r}) := \sum_{n}^{N} \sum_{\mathbf{k}}^{\mathrm{BZ}} \underline{\varphi}^{\dagger}_{n\mathbf{k}}(\mathbf{r})\, \boldsymbol{\sigma}\, \underline{\varphi}_{n\mathbf{k}}(\mathbf{r}) \,. \tag{1.3.2}$$

In the equation above, $\boldsymbol{\sigma} = (\underline{\underline{\sigma}}_x, \underline{\underline{\sigma}}_y, \underline{\underline{\sigma}}_z)$ is a vector with the Pauli matrices as components. The magnetization encapsulates the information about the spin polarization. To continue using the total electron density, which disregards the spin degree of freedom, the energy functionals become explicitly dependent on the magnetization, *e.g.*,

$$E_{\mathrm{xc}}[\rho] \;\rightarrow\; E_{\mathrm{xc}}[\rho, \mathbf{m}] \,. \tag{1.3.3}$$

Assuming the functional dependence in the r.h.s. of Eq. (1.3.3), the minimization of the ground-state energy functional yields a new term in the KS equations, the *exchange-correlation magnetic field*:

$$\mathbf{b}_{\mathrm{xc}}(\mathbf{r}) = \frac{\delta E_{\mathrm{xc}}[\rho, \mathbf{m}]}{\delta \mathbf{m}(\mathbf{r})} \,. \tag{1.3.4}$$

In other words, the effects of the magnetization of the electron density can be interpreted through a local magnetic field. An external magnetic field $\mathbf{b}_{\mathrm{ext}}(\mathbf{r})$ can be added to this internal field, and both are combined as part of an ef-

fective magnetic field in $\mathbf{b}_{\text{eff}}(\mathbf{r}) := \mathbf{b}_{\text{xc}}(\mathbf{r}) + \mathbf{b}_{\text{ext}}(\mathbf{r})$, which enters into the KS equations as follows:

$$\left\{-\frac{1}{2}\nabla^2 + v_{\text{eff}}(\mathbf{r}, [\rho, \mathbf{m}]) + \mathbf{b}_{\text{eff}}(\mathbf{r})\cdot\boldsymbol{\sigma} - \epsilon_{n\mathbf{k}}\right\} \underline{\varphi}_{n\mathbf{k}}(\mathbf{r}) = 0\,. \tag{1.3.5}$$

A nuance of the spin-polarized SCF cycle must be noticed here: Starting from a non-polarized density $\rho_{\text{init}}(\mathbf{r})$ in the absence of an external field will always result in a non-polarized density, as only the third term in Eq. (1.3.5) couples the two spinor contributions. To obtain a magnetic ground state, an initial magnetization $\mathbf{m}_0(\mathbf{r}) \neq \mathbf{0}$ or an external field $\mathbf{b}_{\text{ext}}(\mathbf{r}) \neq \mathbf{0}$ must be included. Once the magnetization has stabilized, $\mathbf{b}_{\text{ext}}(\mathbf{r})$ may then be turned off.

The general spin treatment has two important limitations. First, the energy functionals employed in this work were derived under the assumption of collinear spins and often exhibit numerical instability when extended to the general case. Second, this methodology greatly increases the computational cost compared to the non-spin-polarized procedure. Assuming that the KS Hamiltonian is expressed in a basis set as a matrix of dimension $N_b \times N_b$ for the non-polarized case, the spinor treatment demands a matrix of dimension $2N_b \times 2N_b$. As the diagonalization of a matrix of dimension N_b scales in order $\sim\mathcal{O}(N_b^3)$, this treatment can significantly increase the computational cost.

1.3.2 Spin-orbit coupling

To fully incorporate all relativistic effects, such as Spin-orbit coupling (SOC), it is necessary to solve the full Dirac equation for the KS system within the non-collinear framework [28]:

$$\begin{pmatrix} v_{\text{eff}}(\mathbf{r}) & c\,\mathbf{p}\cdot\boldsymbol{\sigma} \\ c\,\mathbf{p}\cdot\boldsymbol{\sigma} & v_{\text{eff}}(\mathbf{r}) - 2c^2 \end{pmatrix} \begin{pmatrix} \alpha_{n\mathbf{k}}(\mathbf{r}) \\ \beta_{n\mathbf{k}}(\mathbf{r}) \end{pmatrix} = \epsilon_{n\mathbf{k}} \begin{pmatrix} \alpha_{n\mathbf{k}}(\mathbf{r}) \\ \beta_{n\mathbf{k}}(\mathbf{r}) \end{pmatrix}\,, \tag{1.3.6}$$

with c the speed of light and $\mathbf{p}$ the momentum operator. A description of the iterative solution of this equation can be found in Ref. [29]. It is very common, however, to only focus on SOC and include it as a correction to Eq. (1.3.5):

$$\left\{-\frac{1}{2}\nabla^2 + v_{\text{eff}}(\mathbf{r}, [\rho, \mathbf{m}]) + \mathbf{b}_{\text{eff}}(\mathbf{r})\cdot\boldsymbol{\sigma} + \hat{H}_{\text{SOC}} - \epsilon_{n\mathbf{k}}\right\} \underline{\varphi}_{n\mathbf{k}}(\mathbf{r}) = 0\,. \tag{1.3.7}$$

For details on how $\hat{H}_{\text{SOC}}$ can be chosen, see Refs. [30, 31].

1.3.3 Collinear polarization

A common and important approximation regarding magnetic materials is the assumption of collinear spin ordering. This means that all electron spins in the system align to one axis, *e.g.*, the z-axis. The spins then only differ by sign, *i.e.*, one can speak of only *spin-up* ($\uparrow$) and *spin-down* ($\downarrow$) electrons. Specifically this means, that all KS spinors are of the form

$$\underline{\varphi}_{n\mathbf{k}}(\mathbf{r}) = \begin{pmatrix} \varphi^{\uparrow}_{n\mathbf{k}}(\mathbf{r}) \\ 0 \end{pmatrix} \quad \text{or} \quad \underline{\varphi}_{n\mathbf{k}}(\mathbf{r}) = \begin{pmatrix} 0 \\ \varphi^{\downarrow}_{n\mathbf{k}}(\mathbf{r}) \end{pmatrix} . \tag{1.3.8}$$

For these states, the density is evaluated through the spin-resolved densities:

$$\rho(\mathbf{r}) = \rho_{\uparrow}(\mathbf{r}) + \rho_{\downarrow}(\mathbf{r}) , \tag{1.3.9}$$

which are from spin resolved orbitals, carrying the spin index σ:

$$\rho_{\sigma}(\mathbf{r}) = \sum_{n}^{N} \sum_{\mathbf{k}}^{\mathrm{BZ}} \left|\varphi^{\sigma}_{n\mathbf{k}}(\mathbf{r})\right|^2 , \qquad \sigma \in \{\uparrow,\downarrow\} \equiv \{+1,-1\} . \tag{1.3.10}$$

The magnetization in this case works out to be [32]:

$$\mathbf{m}(\mathbf{r}) = \big(0, 0, m(\mathbf{r})\big), \quad m(\mathbf{r}) = \rho_{\uparrow}(\mathbf{r}) - \rho_{\downarrow}(\mathbf{r}) . \tag{1.3.11}$$

And the inverse transformations may be written as:

$$\rho_{\uparrow}(\mathbf{r}) = \frac{1}{2}\big[\rho(\mathbf{r}) + m(\mathbf{r})\big], \quad \rho_{\downarrow}(\mathbf{r}) = \frac{1}{2}\big[\rho(\mathbf{r}) - m(\mathbf{r})\big] . \tag{1.3.12}$$

With this, the dependency can be shifted away from the magnetization, towards the spin-resolved densities:

$$E_{\mathrm{xc}}[\rho, m] \;\rightarrow\; E_{\mathrm{xc}}[\rho_{\uparrow}, \rho_{\downarrow}] . \tag{1.3.13}$$

Necessary for the inclusion of magnetic interaction has previously been the exchange-correlation magnetic field. For collinear systems, the magnetic field is considered to have only a non-vanishing z-component.

Inserting Eq. (1.3.12) into Eq. (1.3.4), the collinear exchange-correlation magnetic field can be evaluated as:

$$b_{\mathrm{xc}}(\mathbf{r}) = \frac{1}{2}\frac{\delta E_{\mathrm{xc}}[\rho_{\uparrow}, \rho_{\downarrow}]}{\delta \rho_{\uparrow}(\mathbf{r})} - \frac{1}{2}\frac{\delta E_{\mathrm{xc}}[\rho_{\uparrow}, \rho_{\downarrow}]}{\delta \rho_{\downarrow}(\mathbf{r})} =: \frac{1}{2} v^{\uparrow}_{\mathrm{xc}}(\mathbf{r}) - \frac{1}{2} v^{\downarrow}_{\mathrm{xc}}(\mathbf{r}) . \tag{1.3.14}$$

In a similar fashion the exchange-correlation potential becomes:

$$v_{\mathrm{xc}}(\mathbf{r}) = \frac{1}{2}\frac{\delta E_{\mathrm{xc}}[\rho_\uparrow, \rho_\downarrow]}{\delta \rho_\uparrow(\mathbf{r})} + \frac{1}{2}\frac{\delta E_{\mathrm{xc}}[\rho_\uparrow, \rho_\downarrow]}{\delta \rho_\downarrow(\mathbf{r})} = \frac{1}{2} v_{\mathrm{xc}}^{\uparrow}(\mathbf{r}) + \frac{1}{2} v_{\mathrm{xc}}^{\downarrow}(\mathbf{r}) \,. \tag{1.3.15}$$

It is $v_{\mathrm{xc}}(\mathbf{r}) \pm b_{\mathrm{xc}}(\mathbf{r})$ (respective the spin) which enters into the KS equations of Eq. (1.3.5), which decouples the opposite spin-contributions. At last, this simplifies the KS equations into two, separated for spin, sets of equations [18]:

$$\left\{ -\frac{1}{2}\nabla^2 + v_{\mathrm{eff}}^{\sigma}(\mathbf{r}, [\rho_\uparrow, \rho_\downarrow]) + \mathrm{sign}(\sigma)\, b_{\mathrm{ext}}(\mathbf{r}) - \epsilon_{n\mathbf{k}}^{\sigma} \right\} \varphi_{n\mathbf{k}}^{\sigma}(\mathbf{r}) = 0 \,, \tag{1.3.16}$$

with two separate effective potentials :

$$v_{\mathrm{eff}}^{\sigma}(\mathbf{r}, [\rho_\uparrow, \rho_\downarrow]) = v_{\mathrm{ext}}(\mathbf{r}) + \int \frac{\rho(\mathbf{r}')}{|\mathbf{r} - \mathbf{r}'|}\, \mathrm{d}\mathbf{r}' + v_{\mathrm{xc}}^{\sigma}(\mathbf{r}) \,. \tag{1.3.17}$$

Worthy of notice is that for the Hartree energy, the total density $\rho(\mathrm{r})$ is considered, not a spin-resolved one. It is only the exchange-correlation potential v_{xc}^{σ}, that is explicitly spin-dependent and that has absorbed the interactions previously encapsulated in b_{xc}.

1.3.4 Second-variation scheme

Above it was shown that within the collinear approximation the KS equations only require the spin-dependent exchange-correlation potentials v_{xc}^{σ}. With this, the two sets of KS equations can be solved independently. In principle, this doubles the computational cost with respect to the non-polarized system. As the bulk of the calculations presented in this work were done using the **exciting** code, this section serves to present an alternative, that is implemented in that package. This alternative is known as the *second-variation* (SV) method. The basic assumption of the method, is that spin-dependent effects are generally a small variation of the non-polarized ground state. The purpose is to reduce the number of basis functions, in which the spin-dependent Hamiltonian is expanded in, a problem outlined in Section 1.3.1.

The term "first variation" (FV) refers to the diagonalization of the non-polarized Hamiltonian, expanded in the LAPW+lo basis set used in **exciting**

$$H_{\mathbf{G}\mathbf{G}'}^{\mathrm{FV}}(\mathbf{k}) := \langle \phi_{\mathbf{G}+\mathbf{k}} | -\frac{1}{2}\nabla^2 + v_{\mathrm{eff}}(\mathbf{r}) | \phi_{\mathbf{G}'+\mathbf{k}} \rangle \,. \tag{1.3.18}$$

Details on the diagonalization methods in **exciting** can be found in Ref. [10].

Resulting from this are the FV eigenvalues:

$$\sum_{\mathbf{G}'} H^{\mathrm{FV}}_{\mathbf{G}\mathbf{G}'}(\mathbf{k})\, C^{\mathrm{FV}}_{\mathbf{G}'n}(\mathbf{k}) = \sum_{\mathbf{G}''} \epsilon^{\mathrm{FV}}_{n\mathbf{k}}\, S_{\mathbf{G}\mathbf{G}''}(\mathbf{k})\, C^{\mathrm{FV}}_{\mathbf{G}''n}(\mathbf{k})\,. \tag{1.3.19}$$

The FV eigenstates:

$$|\varphi^{\mathrm{FV}}_{n\mathbf{k}}\rangle = \sum_{\mathbf{G}} C^{\mathrm{FV}}_{\mathbf{G}n}(\mathbf{k})|\phi_{\mathbf{G}+\mathbf{k}}\rangle \tag{1.3.20}$$

do not include any information about spin-resolution. This is included only in the SV through b_{eff}, which solves the full spinor equation. Considered here is the only the collinear approximation, though the extension to the non-collinear case is natural in this formulation. The Hamiltonian is therefore block-diagonal. The main benefit in this, is the fact that through the diagonalization of the FV-Hamiltonian an effective and smaller basis set has been obtained. Instead of the previous LAPW+lo functions, the Hamiltonian is expanded into the FV eigenstates, with its matrix elements expressed as:

$$H^{\mathrm{SV},\sigma}_{nn'}(\mathbf{k}) := \langle\varphi^{\mathrm{FV}}_{n\mathbf{k}}|\hat{H}^{\mathrm{FV}}(\mathbf{k}) + \mathrm{sign}(\sigma)\, b_{\mathrm{eff}}(\mathbf{r})|\varphi^{\mathrm{FV}}_{n'\mathbf{k}}\rangle\,. \tag{1.3.21}$$

The number of FV eigenstates is the number of valence electrons in the unit cell plus the number of empty states considered. As a reference, a typical ground-state calculation of Chapter 4 contains $N_b = 3920$ basis functions, but only 1172 FV eigenstates. The final, spin-resolved, SV eigenstates are calculated through the solution of:

$$\begin{pmatrix} \mathbb{1}\cdot\epsilon^{\mathrm{FV}}_{\mathbf{k}} + b_{\mathrm{eff}}(\mathbf{k}) & 0 \\ 0 & \mathbb{1}\cdot\epsilon^{\mathrm{FV}}_{\mathbf{k}} - b_{\mathrm{eff}}(\mathbf{k}) \end{pmatrix} \begin{pmatrix} C^{\mathrm{SV},\uparrow}(\mathbf{k}) \\ C^{\mathrm{SV},\downarrow}(\mathbf{k}) \end{pmatrix} = \begin{pmatrix} \epsilon^{\mathrm{SV},\uparrow}_{\mathbf{k}} \\ \epsilon^{\mathrm{SV},\downarrow}_{\mathbf{k}} \end{pmatrix} \begin{pmatrix} C^{\mathrm{SV},\uparrow}(\mathbf{k}) \\ C^{\mathrm{SV},\downarrow}(\mathbf{k}) \end{pmatrix}, \tag{1.3.22}$$

where $\epsilon^{\mathrm{FV}}_{\mathbf{k}} := (\epsilon^{\mathrm{FV}}_{1\mathbf{k}}, \epsilon^{\mathrm{FV}}_{2\mathbf{k}}, ..., \epsilon^{\mathrm{FV}}_{n\mathbf{k}})^{\mathrm{T}}$. $\mathbb{1}$ denotes the identity matrix, and $b_{\mathrm{eff}}(\mathbf{k})$ the Fourier transform of the effective magnetic field expressed as a matrix in the FV basis. In summary, the SV method reduces the computational cost by using a truncated basis constructed from a non-spin-polarized calculation, while still accounting for spin effects accurately. As a consequence it creates an inherent dependence on the number of FV eigenstates for numerical accuracy. In other words, the number of empty states n_{empty} becomes a convergence-parameter for spin-polarized calculations in the SV and therefore `exciting`.

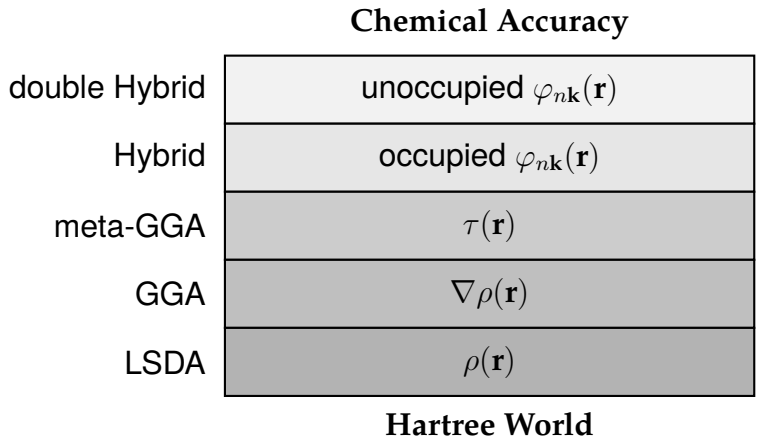

Figure 1.2: "Jacob's Ladder" as introduced by J.P. Perdew and coworkers in Ref. [15]. Five rungs of density-functional approximations ascend from "Hartree World" toward "Chemical Accuracy". Inside the rungs the added dependency to the functional, with the corresponding class of functionals on the left. For more information on double hybrid functionals see the original reference.

1.4 Exchange-correlation functionals

The most important aspect of a DFT-based approach is the necessity of approximations to the exchange-correlation energy functional $E_{\text{xc}}[\rho]$, from now on also simply called the *functional*. The goal of this work is the investigation of specifically these approximations to the functional, which are outlined in the following section. In it, the functionals are organized hierarchically by *Jacob's ladder*, a conceptual framework introduced by J.P. Perdew and coworkers in Ref. [15], which relates accuracy and complexity of the functionals. First, a reformulation within the collinear approximation is made:

$$E_{\text{xc}}[\rho_\uparrow, \rho_\downarrow] = \int \rho(\mathbf{r})\, \varepsilon\big(\mathbf{r}, [\rho_\uparrow, \rho_\downarrow]\big)\, \mathrm{d}\mathbf{r}\,. \tag{1.4.1}$$

The functional is expressed through the exchange-correlation energy density per electron ε, to which add more and more "ingredients", quantities of the system, are added. Within the image of Jacob's ladder, these ingredients are what achieves chemical accuracy and escapes "Hartree World". This work will have the specific focus of magnetic properties of cobalt and La_2CuO_4, and the functionals are introduced with that focus in mind. Figure 1.2 shows the classes of functionals as introduced in Ref. [15], with the corresponding main quantity of the KS system. The class of double hybrid functionals is included, though it is not relevant for this thesis. For deeper investigations of this classification of functionals, see Refs. [33–37].

1.4.1 Local and semi-local functionals

The lowest rank includes only an explicit dependence on the density at a single point within ϵ_{xc}. This is called the local-density approximation, or local-spin-density approximation (LSDA) for the purposes of this thesis. Explicitly:

$$\varepsilon_{\text{LSDA}} = \varepsilon_{\text{xc}}^{\text{unif}}\big(\rho_\sigma(\mathbf{r})\big) \,. \tag{1.4.2}$$

Within the LSDA this function is approximated by the corresponding relationship in the homogeneous electron gas $\varepsilon_{\text{xc}}^{\text{unif}}$ [38–42]. The exchange energy of the gas is known analytically, while the correlation part follows the parametrization of J.P. Perdew and Y. Wang of Ref. [43] is used in later chapters. By design, this approximation is intended for systems with only very slowly varying density over space. It can, however, also be applied to a wider range of materials with rather good results for properties such as lattice constants, bulk moduli, and vibrational frequencies [44–46]. One specific drawback, which will be repeatedly referenced for the following functionals as well, is the self-interaction error (SIE) discussed in Section 1.1.1, *i.e.*, spurious Coulomb repulsion of an electron with itself. While the exchange of the true functional cancels this interaction out, the LSDA-exchange notably does not. This repulsion of an electron density with itself causes a delocalization ("puffing up") of an electronic state and, among other things, underestimated band gaps for semiconductors [47].

Attempts to improve upon this approximation led to the development of the generalized gradient approximation (GGA), which tries to better capture the effect of varying density profiles by including a dependence on the gradient of the density:

$$\varepsilon_{\text{GGA}} = \varepsilon_{\text{GGA}}\big(\rho_\sigma(\mathbf{r}), \nabla\rho_\sigma(\mathbf{r})\big) \,. \tag{1.4.3}$$

The most common GGA functional used for solid-state computations is the one introduced by J. P. Perdew, K. Burke and M. Ernzerhof (PBE) in Ref. [48]. This will also be the only GGA functional used in this work. It is worthwhile to highlight one feature of the PBE functional in more detail: The gradient-dependent exchange enhancement. The exchange energy is written as:

$$E_{\text{x}}^{\text{GGA}} = \int \rho(\mathbf{r})\, \varepsilon_{\text{x}}^{\text{unif}}(\rho_\sigma)\, F_{\text{x}}(s)\, \mathrm{d}\mathbf{r} \,, \tag{1.4.4}$$

where $\varepsilon_{\text{x}}^{\text{unif}}$ is the exchange energy per particle of the uniform electron gas, and $F(s)$ is the exchange enhancement depending on a dimensionless density

gradient $s = |\nabla\rho|/(2k_F\,\rho)$. The enhancement obeys the uniform limit, that is it reproduces the uniform-gas exchange $F \to 1$ as $s \to 0$ with $F \geq 1$, among other constraints. In comparison to LSDA, the PBE functional reduces the SIE and the increased exchange in regions of strongly varying density generally improves the total energies for magnetic metals and their lattice constants [49, 50]. Overall, PBE is considered a stable functional suitable for a wide range of materials. It still underestimates band gaps [51] and overall struggles with strongly correlated systems [52].

It is important to note that both the LSDA and PBE functional were specifically formulated with the assumption of collinear spin. One popular method of extension, to also allow non-collinear calculation, is the method introduced by J. Kübler and coworkers in Ref. [53]. In this method, the scalar magnetization density $m(\mathbf{r})$ that enters into the functionals is replaced by the norm of the non-collinear vector valued magnetization density $|\mathbf{m}(\mathbf{r})|$. This method was, however, not specifically designed for GGA functionals and suffers from numerical instability when applied to them and alternatives are still the subject of current research [54].

1.4.2 Meta-GGA functionals

Continuing this procedure of development leads to the meta-GGA (mGGA) functionals. Together with the gradient of the density, now also the local kinetic-energy density, $\tau_\sigma(\mathbf{r})$, goes into the exchange-correlation functional:

$$\varepsilon_{\text{mGGA}} = \varepsilon_{\text{mGGA}}\big(\rho_\sigma(\mathbf{r}), \nabla\rho_\sigma(\mathbf{r}), \tau_\sigma(\mathbf{r})\big)\,, \tag{1.4.5}$$

where τ_σ can be obtained via the occupied KS orbitals:

$$\tau_\sigma(\mathbf{r}) = \frac{1}{2}\sum_{n}^{N}\sum_{\mathbf{k}}^{\text{BZ}} |\nabla\varphi^\sigma_{n\mathbf{k}}(\mathbf{r})|^2 \tag{1.4.6}$$

and the total kinetic-energy density is given by $\tau(\mathbf{r}) = \tau_\uparrow(\mathbf{r}) + \tau_\downarrow(\mathbf{r})$, similar to the electronic density $\rho(\mathbf{r})$. Some mGGA functionals [55] also include the Laplacian of the density $\Delta\rho_\sigma(\mathbf{r})$, though these functionals are not considered here. This class of functionals is, as previously, in principle only formulated for the collinear case. Even further, the kinetic energy density depends only implicitly, through the orbitals, on ρ_σ. While this includes previously ignored non-local effects, the functional derivative v_{xc} is more intricate than for previous functionals. This results in the implementation of the mGGA often not

involving the KS equations, but rather the so-called generalized Kohn-Sham scheme, see Ref. [56].

One of the first mGGA and still a popular functional, is the one introduced in Ref. [57] by J. Tao, J. P. Perdew, V. N. Staroverov, and G. E. Scuseria (TPSS). A consideration in the design of GGA and mGGA functionals are *constraints*, *i.e.*, certain properties the true exchange-correlation functional satisfies. Fitting a mGGA functional to these constraints led to the development of the *strongly constrained and appropriately normed* (SCAN) functional [58, 59], which is generally considered to be the gold standard for mGGA functionals with regard to accuracy [8]. As was done for PBE, a closer look at the exchange energy of those two functionals is had, to highlight the inclusion of the kinetic-energy density and how the different mGGA functionals implement it. The mGGA-exchange makes use of an dimensionless *isolated-orbital indicator* α in the exchange enhancement:

$$F_{\mathrm{x}}(s) \to F_x(s, \alpha) \; . \tag{1.4.7}$$

The mGGA differ both in form of α and their dependency on the parameter. TPSS implements a simple ratio between the kinetic energy density and the Weizsäcker kinetic energy density $\tau^{\mathrm{W}} = (1/8)|\nabla\rho|^2/\rho$, explicitly $\alpha = \tau^{\mathrm{W}}/\tau$. In the original paper, this parameter is denoted z, but for uniformity α is used here. The non-polarized expression suffices, see Ref. [57]. SCAN on the other hand takes the ratio with the kinetic energy density of the uniform electron gas, $\alpha = (\tau - \tau^{\mathrm{W}})/\tau^{\mathrm{unif}}$, where $\tau^{\mathrm{unif}} = (3/10)(3\pi^2)^{2/3}\rho^{5/3}$. This choice is considered the more useful one, when conformity to constrains is concerned [60]. A downside of SCAN in this regard, which is not apparent here, is the major numerical instability the SCAN exchange enhancement causes. This is specifically caused by the sharp dependency on α, causing both a slower convergence in the number of **k**-points and numerical noise, due to sharp edges in F_{x}. This motivated attempts at revising the functional, making it more stable by regularizing $F_{\mathrm{x}}(s, \alpha)$, while keeping the accuracy [61, 62]. Most noteworthy for this works purposes is the r2SCAN functional (SCAN twice revised), which generally achieves its goal by sacrificing less accuracy than rSCAN.

1.4.3 Hybrid functionals

Hartree-Fock theory provides an exact, self-interaction free form of the exchange energy. Hybrid functionals exploit this, by "mixing" this exact, non-local, exchange $E_{\mathrm{x}}^{\mathrm{NL}}$ with the local exchange-correlation energy $E_{\mathrm{xc}}^{\mathrm{L}}$ of Section 1.4.1, as Hartree-Fock does not offer the according correlation energy. The mixing takes the form:

$$E_{\mathrm{xc}}^{\mathrm{hyb}} = E_{\mathrm{xc}}^{\mathrm{L}} + \beta \left(E_{\mathrm{x}}^{\mathrm{NL}} - E_{\mathrm{x}}^{\mathrm{L}} \right) . \tag{1.4.8}$$

Above, $E_{\mathrm{x}}^{\mathrm{L}}$ denotes the exchange of local nature. Furthermore, β is called the mixing parameter and the exact-exchange energy is given by:

$$E_{\mathrm{x}}^{\mathrm{NL}} = -\frac{1}{2} \sum_{\sigma,n,n',\mathbf{k}} \iint \frac{\varphi_{n\mathbf{k}}^{\sigma *}(\mathbf{r})\, \varphi_{n'\mathbf{k}}^{\sigma}(\mathbf{r})\, \varphi_{n'\mathbf{k}}^{\sigma *}(\mathbf{r}')\, \varphi_{n\mathbf{k}}^{\sigma}(\mathbf{r}')}{|\mathbf{r} - \mathbf{r}'|} \, \mathrm{d}\mathbf{r}\mathrm{d}\mathbf{r}' . \tag{1.4.9}$$

Such is the approach for the PBE0 functional, in which the local correlation and exchange are taken from PBE with a mixing parameter of $\beta = 0.25$ [63, 64].

When using PBE0 for crystals, though it is only mixed-in, the exact exchange is still rather "harsh", resulting in for example overestimated band gaps [51]. One improvement upon this, is using a *screened* Coulomb potential in the exchange energy, separating the interaction into a short-range and long-range part. This is done in the functional introduced by J. Heyd, G. E. Scuseria, and M. Ernzerhof (HSE) in Ref. [65]:

$$E_{\mathrm{xc}}^{\mathrm{HSE}}(\omega) = E_{\mathrm{xc}}^{\mathrm{PBE}} + \beta \left(E_{\mathrm{x}}^{\mathrm{NL,SR}}(\omega) - E_{\mathrm{x}}^{\mathrm{PBE,SR}}(\omega) \right) . \tag{1.4.10}$$

The essence is the following separation in the Coulomb kernel using the error function ($r = |\mathbf{r}|$):

$$\frac{1}{r} = \frac{\mathrm{erfc}(\omega r)}{r} + \frac{\mathrm{erf}(\omega r)}{r} =: v^{\mathrm{LR}}(r) + v^{\mathrm{SR}}(r) = v(r) . \tag{1.4.11}$$

Used in the following is HSE06 ($\omega = 0.11$), from now on just called HSE. The screening affects the exchange energy by replacing $v(r)$ with $v^{\mathrm{SR}}(r)$ [66].

The 6-dimensional integral in Eq. (1.4.9) drastically increases the computational cost of hybrid functionals with respect to the previous rungs of Jacob's ladder. The main benefit, is SIE-free exchange, whereas the previous rungs could only lessen its impact through exchange enhancement.

1.5 Spin-polarized hybrid functionals in `exciting`

This section outlines a perspective method of calculating a spin-polarized non-local potential in the **exciting** code. As was outlined in Section 1.3.4, spin effects in **exciting** are exclusively treated within the SV scheme. Prior to this this work however, the non-local potential used in hybrid-functional calculations was constructed using only FV states and had no contribution to the SV Hamiltonian. The following methodology extends hybrid-functional calculations to collinear-spin systems by incorporating spin-dependent contributions of the non-local exchange into the SV framework. Although no final results could be obtained using this implementation, it is included here to document the theoretical groundwork and strategy, which may serve as a foundation for future development and studies.

1.5.1 Current construction of the non-local potential

To begin, the focus will be on the current methodology of hybrid functionals implemented in **exciting**. In a hybrid-functional calculation, the so-called non-local potential, see also Section 1.4.3 for the definition of the non-local exchange energy, is included in the FV Hamiltonian with the mixing parameter β [67]:

$$\sum_{\mathbf{G}'} \left[H_{\mathbf{G}\mathbf{G}'}(\mathbf{k}) + \beta\, V^{\mathrm{NL}}_{\mathbf{G}\mathbf{G}'}(\mathbf{k}) \right] C^{\mathrm{FV}}_{\mathbf{G}'n}(\mathbf{k}) = \epsilon^{\mathrm{FV}}_{n\mathbf{k}} \sum_{\mathbf{G}'} S_{\mathbf{G}\mathbf{G}'}(\mathbf{k})\, C^{\mathrm{FV}}_{\mathbf{G}'n}(\mathbf{k})\,. \tag{1.5.1}$$

Here, the non-local potential $V^{\mathrm{NL}}_{\mathbf{G}\mathbf{G}'}(\mathbf{k})$ is included in LAPW+lo basis. Within **exciting** however, it is first constructed in KS basis (*i.e.*, FV) and is obtained by a sum over all occupied states and BZ sampling points $\mathbf{q}$ of a six-dimensional integral:

$$V^{\mathrm{NL}}_{nn'}(\mathbf{k}) = -\sum_{n''}^{\mathrm{occ}} \sum_{\mathbf{q}} \int \frac{\varphi^*_{n\mathbf{k}}(\mathbf{r})\, \varphi_{n''\mathbf{q}}(\mathbf{r})\, \varphi^*_{n''\mathbf{q}}(\mathbf{r}')\, \varphi_{n'\mathbf{k}}(\mathbf{r}')}{|\mathbf{r}-\mathbf{r}'|} \mathrm{d}\mathbf{r}\mathrm{d}\mathbf{r}'\,. \tag{1.5.2}$$

As the direct solution of the integral appearing in Eq. (1.5.1) for the given KS orbitals would be exceedingly computationally demanding, **exciting** employs a new basis set. This new basis set is constituted of products of two KS wave functions and is called the mixed-product basis (MPB) [68]:

$$\varphi_{n\mathbf{k}}(\mathbf{r})\, \varphi^*_{n'\mathbf{k}-\mathbf{q}}(\mathbf{r}) =: \sum_I M^I_{nn'}(\mathbf{k},\mathbf{q})\, \chi^{\mathbf{q}}_I(\mathbf{r})\,, \tag{1.5.3}$$

where $\chi_I^{\mathbf{q}}$ encapsulates product of two LAPW+lo functions and $M^I_{nn'}$ are the MPB coefficients. These are calculated through the integral:

$$M^I_{nn'}(\mathbf{k},\mathbf{q}) = \langle \chi^{\mathbf{q}} \varphi_{n'\mathbf{k}-\mathbf{q}} | \varphi_{n\mathbf{k}} \rangle \tag{1.5.4}$$

$$= \int \left[\chi_I^{\mathbf{q}}\, \varphi_{n'\mathbf{k}-\mathbf{q}}(\mathbf{r})\right]^* \varphi_{n\mathbf{k}}(\mathbf{r})\, \mathrm{d}\mathbf{r}\,. \tag{1.5.5}$$

Using the MPB, the non-local potential can then be evaluated as [64]:

$$V^{\mathrm{NL}}_{nn'}(\mathbf{k}) = -\sum_{n''}^{\mathrm{occ}} \sum_{\mathbf{q}} \sum_{IJ} \omega_{\mathbf{k}-\mathbf{q}}\, M^{I*}_{nn''}(\mathbf{k},\mathbf{q})\, v_{IJ}(\mathbf{q})\, M^J_{n'n''}(\mathbf{k},\mathbf{q}) \tag{1.5.6}$$

$$= -\sum_{n''}^{\mathrm{occ}} \sum_{\mathbf{q}} \sum_{IJ} \omega_{\mathbf{k}-\mathbf{q}}\, \langle \varphi_{n\mathbf{k}} | \varphi_{n''\mathbf{k}-\mathbf{q}}\, \chi_I^{\mathbf{q}} \rangle\, v_{IJ}(\mathbf{q})\, \langle \chi_J^{\mathbf{q}}\, \varphi_{n''\mathbf{k}-\mathbf{q}} | \varphi_{n'\mathbf{k}} \rangle \tag{1.5.7}$$

$$=: \langle \varphi_{n\mathbf{k}} |\, \hat{V}^{\mathrm{NL}}(\mathbf{k})\, | \varphi_{n'\mathbf{k}} \rangle\,. \tag{1.5.8}$$

The tetrahedron integration weights $\omega_{\mathbf{k}-\mathbf{q}}$ are explicitly included here. Furthermore, v_{IJ} describes the so-called bare Coulomb potential, though it is not relevant for further considerations, as it is purely basis-function dependent. It is typically absorbed into the MPB coefficients:

$$\tilde{M}^I_{nn'}(\mathbf{k},\mathbf{q}) = \sum_J v_{IJ}^{\frac{1}{2}}(\mathbf{q}) M^J_{nn'}(\mathbf{k},\mathbf{q})\,, \tag{1.5.9}$$

which allows for the non-local potential to be simplified to

$$V^{\mathrm{NL}}_{nn'}(\mathbf{k}) = -\sum_{n''}^{\mathrm{occ}} \sum_{\mathbf{q}} \sum_{IJ} \omega_{\mathbf{k}-\mathbf{q}}\, \tilde{M}^{I*}_{nn''}(\mathbf{k},\mathbf{q})\, \tilde{M}^J_{n'n''}(\mathbf{k},\mathbf{q}) \tag{1.5.10}$$

Before adding the non-local potential to the FV Hamiltonian, it is translated into the LAPW+lo basis:

$$V^{\mathrm{NL}}_{\mathbf{G}\mathbf{G}'}(\mathbf{k}) = \sum_{nn'} \left[\sum_{\mathbf{G}''} S^\dagger_{\mathbf{G}\mathbf{G}''}(\mathbf{k})\, C^{\mathrm{FV}}_{\mathbf{G}''n}(\mathbf{k})\right] V^{\mathrm{NL}}_{nn'}(\mathbf{k}) \left[\sum_{\mathbf{G}''} C^{\mathrm{FV},\dagger}_{n'\mathbf{G}''}(\mathbf{k})\, S_{\mathbf{G}''\mathbf{G}'}(\mathbf{k})\right]. \tag{1.5.11}$$

1.5.2 Extension to the second variation

For a spin-resolved treatment of hybrid functionals in the second variation, the non-local operator $\hat{V}^{\mathrm{NL}}$ has to be constructed using the spin-resolved states. These are given through a linear combination of the FV eigenstates (the basis)

and SV eigenvectors (the coefficients):

$$|\varphi^{\mathrm{SV},\sigma}_{n\mathbf{k}}\rangle = \sum_i C^{\mathrm{SV},\sigma}_{in}(\mathbf{k})\,|\varphi^{\mathrm{FV}}_{i\mathbf{k}}\rangle \equiv \sum_i C^{\mathrm{SV},\sigma}_{in}(\mathbf{k})\,|\varphi_{i\mathbf{k}}\rangle\ . \tag{1.5.12}$$

With this, the non-local potential becomes (with the abbreviation $\mathbf{p} := \mathbf{k} - \mathbf{q}$):

$$V^{\mathrm{NL},\sigma}_{nn'}(\mathbf{k}) = -\sum_{n'',\mathbf{q},IJ,ij} \omega^\sigma_{\mathbf{p}}\, C^{\mathrm{SV},\sigma}_{in''}(\mathbf{p}) \langle\varphi_{n\mathbf{k}}|\varphi^\sigma_{i\mathbf{p}}\,\chi^{\mathbf{q}}_I\rangle\, v_{IJ}(\mathbf{q})\, \langle\varphi_{j\mathbf{p}}\,\chi^{\mathbf{q}}_J|\varphi_{n'\mathbf{k}}\rangle\, C^{\mathrm{SV},\sigma *}_{jn''}(\mathbf{p})\ . \tag{1.5.13}$$

The integration weights $\omega^\sigma_{\mathbf{p}}$ need to be spin-dependent, as for ferromagnetic materials the majority and minority bands below the Fermi level may differ for different $\mathbf{k}$-points. To be precise, the number of occupied states (the summation limit for n'' above, may differ for different spin-channels and $\mathbf{k}$-points. Furthermore, only the "inner" states, the ones constituting the non-local operator defined in Eq. (1.5.6), are spin-polarized. The "outer" states serve simply to project onto the FV eigenstates, the basis of the SV Hamiltonian, and must stay unchanged. To simplify and highlight the changes, Eq. (1.5.13) is brought again to the form of Eq. (1.5.10). The SV eigenvector matrices absorbed into the now spin-polarized MPB coefficients:

$$\tilde{M}^{I\sigma}_{nn'}(\mathbf{k},\mathbf{q}) = \sum_i \tilde{M}^I_{ni}(\mathbf{k},\mathbf{q}) C^{\mathrm{SV},\sigma *}_{in'}(\mathbf{p})\ , \tag{1.5.14}$$

which leads the final form of the non-local potential in SV:

$$V^{\mathrm{NL},\sigma}_{nn'}(\mathbf{k}) = -\sum_{n''}^{\mathrm{occ}} \sum_{\mathbf{q}} \sum_{IJ} \omega^\sigma_{\mathbf{p}}\, \tilde{M}^{I\sigma *}_{nn''}(\mathbf{k},\mathbf{q})\, \tilde{M}^{J\sigma}_{n'n''}(\mathbf{k},\mathbf{q}) \tag{1.5.15}$$

These two spin-resolved non-local potentials may then be transformed (see Section 1.3.3) to the total non-local potential and a "non-local magnetic field":

$$V^{\mathrm{NL}}_{nn'}(\mathbf{k}) = \frac{1}{2}\left(V^{\mathrm{NL},\uparrow}_{nn'}(\mathbf{k}) + V^{\mathrm{NL},\downarrow}_{nn'}(\mathbf{k})\right) \tag{1.5.16}$$

$$B^{\mathrm{NL}}_{nn'}(\mathbf{k}) = \frac{1}{2}\left(V^{\mathrm{NL},\uparrow}_{nn'}(\mathbf{k}) - V^{\mathrm{NL},\downarrow}_{nn'}(\mathbf{k})\right)\ , \tag{1.5.17}$$

which are then included in the FV and SV Hamiltonian respectively, where additional attention to the basis expansion is necessary. The FV Hamiltonian $H^{\mathrm{FV}}_{\mathrm{GG}'}$ is constructed in LAPW+lo basis. The SV Hamiltonian is constructed from the resulting eigenfunctions of the FV diagonalization. The hybrid-functional SCF cycle in `exciting` is constructed as a *nested loop*. That means, that the non-local potential is calculated, and with that potential a full,

inner cycle is completed until convergence. Following that, is the construction of another non-local potential (the next step in the *outer* cycle), with another inner cycle. This is continued until the changes between the charge densities from two outer-cycle steps is converged. This is done to reduce the number of constructions of the non-local potential, which is by far the most computationally demanding step in a hybrid-functional calculation. $V^{\mathrm{NL}}_{\mathbf{GG'}}$ is included in the state-independent LAPW+lo basis. $B^{\mathrm{NL}}_{nn'}$ however, has to be included in the SV Hamiltonian, expressed in the KS basis that changes every iteration. To guarantee the correct basis, B^{NL} can also be expanded into the LAPW+lo basis and "frozen" (*i.e.*, saved to memory) when constructed, as is V^{NL}. Then, at every construction of the SV Hamiltonian, it is expanded back into the new KS basis. Explicitly, these transformations are:

$$B^{\mathrm{NL}}_{\mathbf{GG'}}(\mathbf{k}) = \sum_{nn'} \left[\sum_{\mathbf{G''}} S^{\dagger}_{\mathbf{GG''}}(\mathbf{k})\, C^{\mathrm{FV}}_{\mathbf{G''}n}(\mathbf{k}) \right] B^{\mathrm{NL}}_{nn'}(\mathbf{k}) \left[\sum_{\mathbf{G''}} C^{\mathrm{FV},\dagger}_{n'\mathbf{G''}}(\mathbf{k})\, S_{\mathbf{G''G'}}(\mathbf{k}) \right] , \tag{1.5.18}$$

$$B^{\mathrm{NL}}_{nn'}(\mathbf{k}) = \sum_{\mathbf{GG'}} C^{\mathrm{FV},\dagger}_{n\mathbf{G}}(\mathbf{k})\, B^{\mathrm{NL}}_{\mathbf{GG'}}(\mathbf{k})\, C^{\mathrm{FV}}_{\mathbf{G'}n'}(\mathbf{k}) \ . \tag{1.5.19}$$

This methodology is currently being compared to literature results of the transition metals iron and cobalt [12, 69]. The schematics of the SCF cycle with this approach are shown in Figure 1.3.

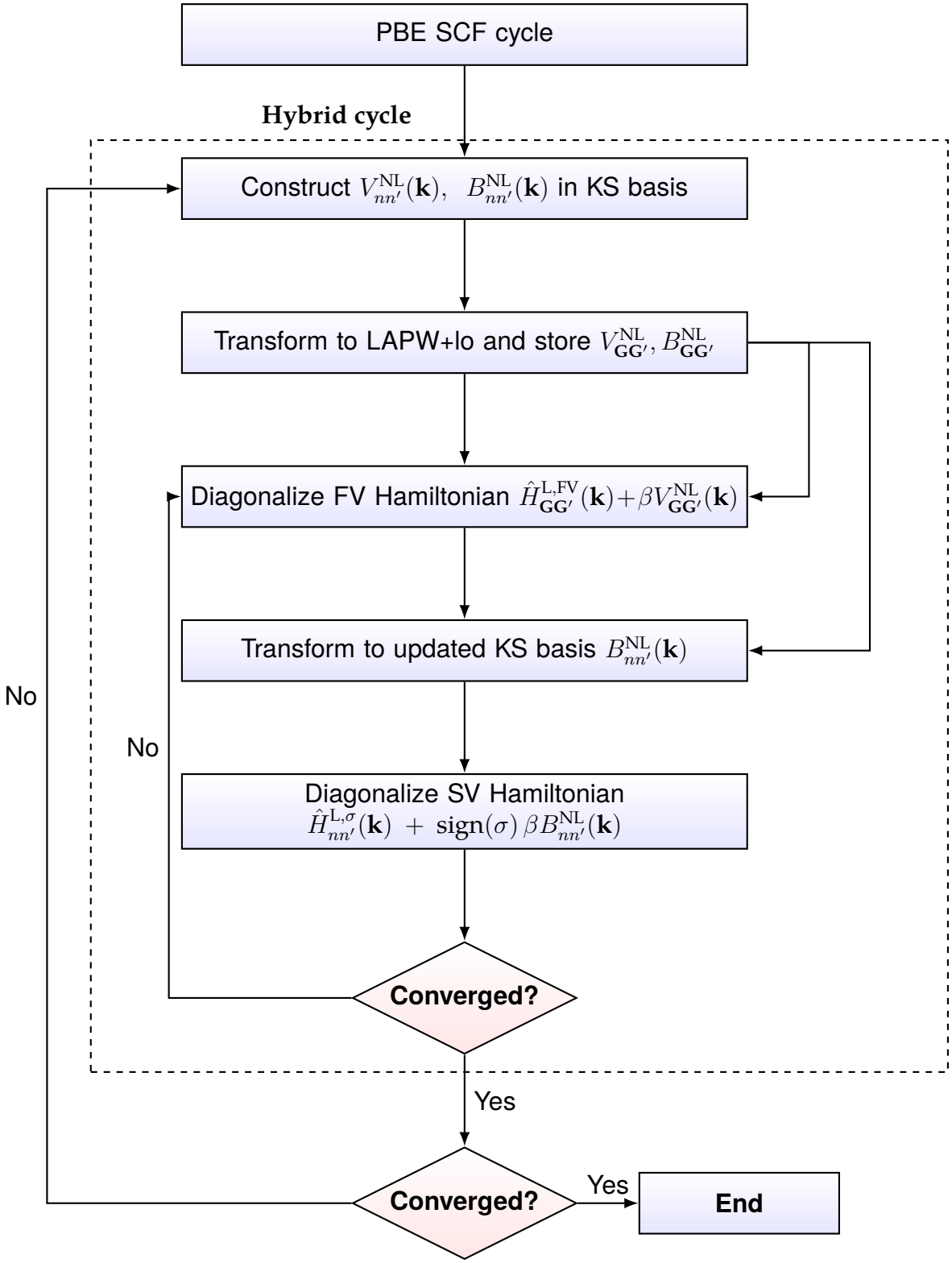

Figure 1.3: Proposed hybrid-functional SCF cycle with nested convergence checks to include spin-effects. Starting point is the density of a PBE SCF cycle.

Chapter 2

The itinerant Ferromagnet Cobalt

This chapter presents a study of the electronic and magnetic structure of bulk cobalt (Co). In the **exciting** code, mGGA functionals have only recently been implemented [11] and thus have not been verified on a complex magnetic system like La_2CuO_4. Similarly, hybrid functionals have not been used in the study of metallic systems in **exciting**. Therefore, Co serves as a more simple material to verify the implementations via cross-reference with **FHI-aims**, in which the calculations are repeated. Magnetic and electronic properties are of particular interest, and thus the ferromagnetic phase (FM) and nonmagnetic phase (NM) are investigated. For this purpose, the equilibrium unit-cell volume is determined through the equation of state (EoS) with the PBE, SCAN, and TPSS functionals. As a direct comparison for the (KS) electronic structure, the density of states (DoS) and band structures are calculated at the equilibrium geometry. For the HSE functional, the band structure and DoS of Co are calculated at a reference unit-cell volume. The calculations performed using PBE here serve as a gauge, both for the differences in results between the two codes **exciting** and **FHI-aims** (see Ref. [70] for a general study on reproducibility in DFT calculations), but also to highlight the effects of mGGA and hybrid functionals on the ground state of the ferromagnetic metal Co.

2.1 Computational details

Elemental cobalt crystallizes in the hexagonal close-packed geometry [71] at low temperatures. However, the face-centered cubic (fcc) unit-cell is chosen here for simplicity, as it requires only one basis atom and is classified by only one lattice constant. The computational parameters were chosen to converge the total energy up to < 0.01 eV per atom and the magnetization $< 0.01\,\mu_B$.

A sampling grid of $32\times32\times32$ **k**-points was used in the BZ for mGGA and PBE functionals. In the case of HSE, this had to be reduced to a number of $16\times16\times16$ **k**-points. The plane-wave cutoff for **exciting** was $R_{\text{MT}}\,G_{\text{max}} = 10$ for all calculations, with $n_{\text{empty}} = 200$ empty states included. The mGGA calculations required the inclusion of additional local orbitals in the species file to achieve numerical convergence, though these were not found to affect the ground state of PBE. Similarly, the angular momentum and plane-wave cutoff for potential and density were increased to $l_{\text{max}} = 12$ and $G_{\text{maxVR}} = 25$. For **FHI-aims**, the "tight" species default was used for cobalt. As a means of achieving occupation numbers, for PBE and mGGA functionals, Gaussian energy broadening [72] with a width of 0.005 Ha was used in both codes. For **exciting**-HSE calculations, the tetrahedron method of Ref. [73] is mandatory. The muffin-tin radius for **exciting** was $R_{\text{MT}} = 2.00\,a_{\text{B}} \approx 1.058$ Å. The majority (minority) spin is set to be spin-up (spin-down). The **exciting** species files, together with all input and output files are available in a NOMAD repository [74] at https://dx.doi.org/10.17172/NOMAD/2025.07.03-1.

The equilibrium unit-cell volume V_0 is obtained through a Birch-Munarghan fit of the EoS [75]. The fit specifcies on top of V_0 also the energy minimum E_0, and other properties such as the bulk modulus, which can be found in Appendix A.2.1. A final ground-state calculation is performed at the obtained equilibrium lattice constant a_0. Due to the nature of the HSE functional and its computational cost, the geometry optimization was not performed using this functional. Instead, the equilibrium lattice constant of similar calculations from Ref. [12] is taken and a single ground-state calculation at this volume was performed in both codes. As the non-local potential used in hybrid-functional calculations is not implemented with spin-polarization currently in **exciting**, only the NM phase is considered for HSE. An implementation of the non-local potential in SV was sketched in Section 1.5.

2.2 Comparison of exciting and FHI-aims

Before addressing the effects of different exchange-correlation approximations, the results of **exciting** and **FHI-aims** are benchmarked against each other. Table 2.1 summarizes the results of the volume optimization for all functionals are and Figure 2.1 shows the EoS for the PBE functional. All functionals in both codes predict a stable FM phase, with an increased lattice constant when compared to the NM phase. While with **exciting** a slightly larger lattice constant of up to 0.01 Å is found for both phases and all functionals,

the EoS is in good agreement, as can be seen in Figure 2.1 for PBE. The energy gap between the magnetic phases agrees within the considered energy accuracy. When using the code-respective equilibrium geometry, the magnetization agrees up to the converged accuracy of $0.01\ \mu_B$. Specifically, PBE results in a unit cell magnetization of $1.65\ \mu_B$ for both codes, TPSS finds 1.67 and $1.66\ \mu_B$ in **exciting** and **FHI-aims** respectively. SCAN predicts the largest moments of the three functionals, $1.80\ \mu_B$ in **exciting** and $1.82\ \mu_B$ in **FHI-aims**. A more detailed discussion on this takes place in the following Section 2.3.

Table 2.1: Equilibrium volume V_0, lattice constant a_0, phase energy difference ΔE_M and unit cell magnetization m_0 of fcc Co in **exciting** and **FHI-aims** for PBE, TPSS, and SCAN. Here, $\Delta E_M = E^0_{FM} - E^0_{NM}$ is the difference between the energy per atom at the respective equilibrium lattice constant a_0 for the two phases. Similarly m_0 is taken from the ground state at equilibrium lattice constant.

Functional	Code	Phase	V_0 [Å^3]	a_0 [Å]	ΔE_M [eV]	m_0 [μ_B]
PBE	**exciting**	NM	10.337	3.458	-	-
	FHI-aims	NM	10.295	3.453	-	-
	exciting	FM	10.966	3.527	0.19	1.65
	FHI-aims	FM	10.914	3.521	0.19	1.65
TPSS	**exciting**	NM	10.015	3.422	-	-
	FHI-aims	NM	9.958	3.415	-	-
	exciting	FM	10.615	3.489	0.19	1.67
	FHI-aims	FM	10.562	3.483	0.18	1.66
SCAN	**exciting**	NM	9.836	3.401	-	-
	FHI-aims	NM	9.788	3.396	-	-
	exciting	FM	10.836	3.513	0.52	1.80
	FHI-aims	FM	10.745	3.503	0.51	1.82

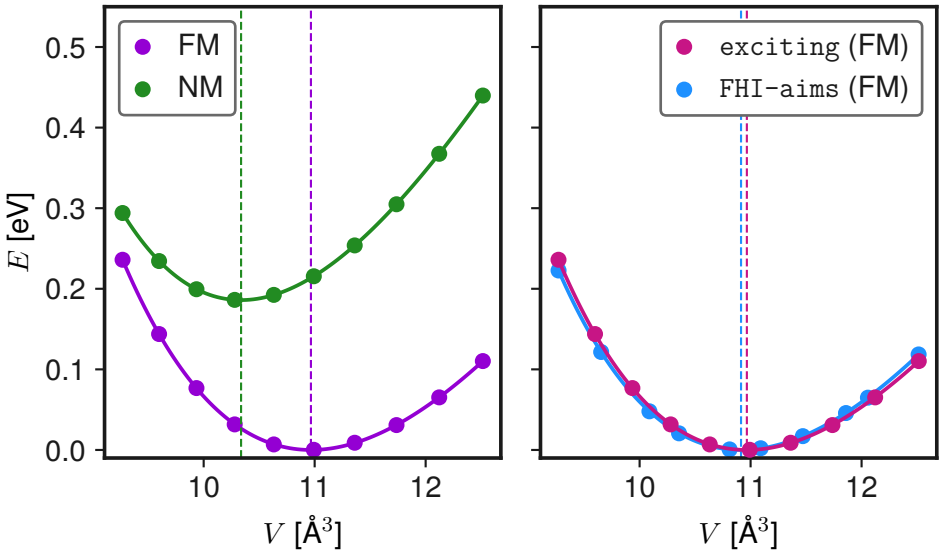

Figure 2.1: EoS of fcc Co using the PBE functional. On the left is a comparison of the two magnetic phases in `exciting`, on the right is a comparison of the FM EoS of `exciting` and `FHI-aims`. Solid lines represent the fit obtained using the Birch-Munarghan EoS (see Appendix A.2.1). The dashed lines mark the respective equilibrium volume.

A more detailed picture requires a comparison of the electronic band structure and DoS. The focus of this work is on magnetic structures, therefore most attention will be given to the FM phase. The comparison of the band structure and DoS of the NM phase between the two codes, except for HSE, can be found in Appendix A.1.1. The results for the FM phase are compared in Figure 2.2. For the PBE functional, the dispersion and the DoS overlap nearly perfectly. The same can be said for the data of the TPSS calculations, which also agree very well between the two codes. A larger discrepancy can be seen in the SCAN figure. Here, there exists a noticeable shift upwards in energy of the `exciting` bands compared to the `FHI-aims` results, which affects the unoccupied spin-down and occupied spin-up states. Still, the minority spin states below the Fermi level overlap nearly identically. Therefore, it is not a constant shift in all states, which could be caused by an incomplete basis set or unconverged Fermi energy. A possible reason for the differences could be the larger discrepancy in lattice constant between the codes for SCAN (0.010 Å) when compared to TPSS (0.006 Å) and PBE (0.006 Å). When viewed alongside the previously discussed results, these deviations observed in the results of SCAN remain modest.

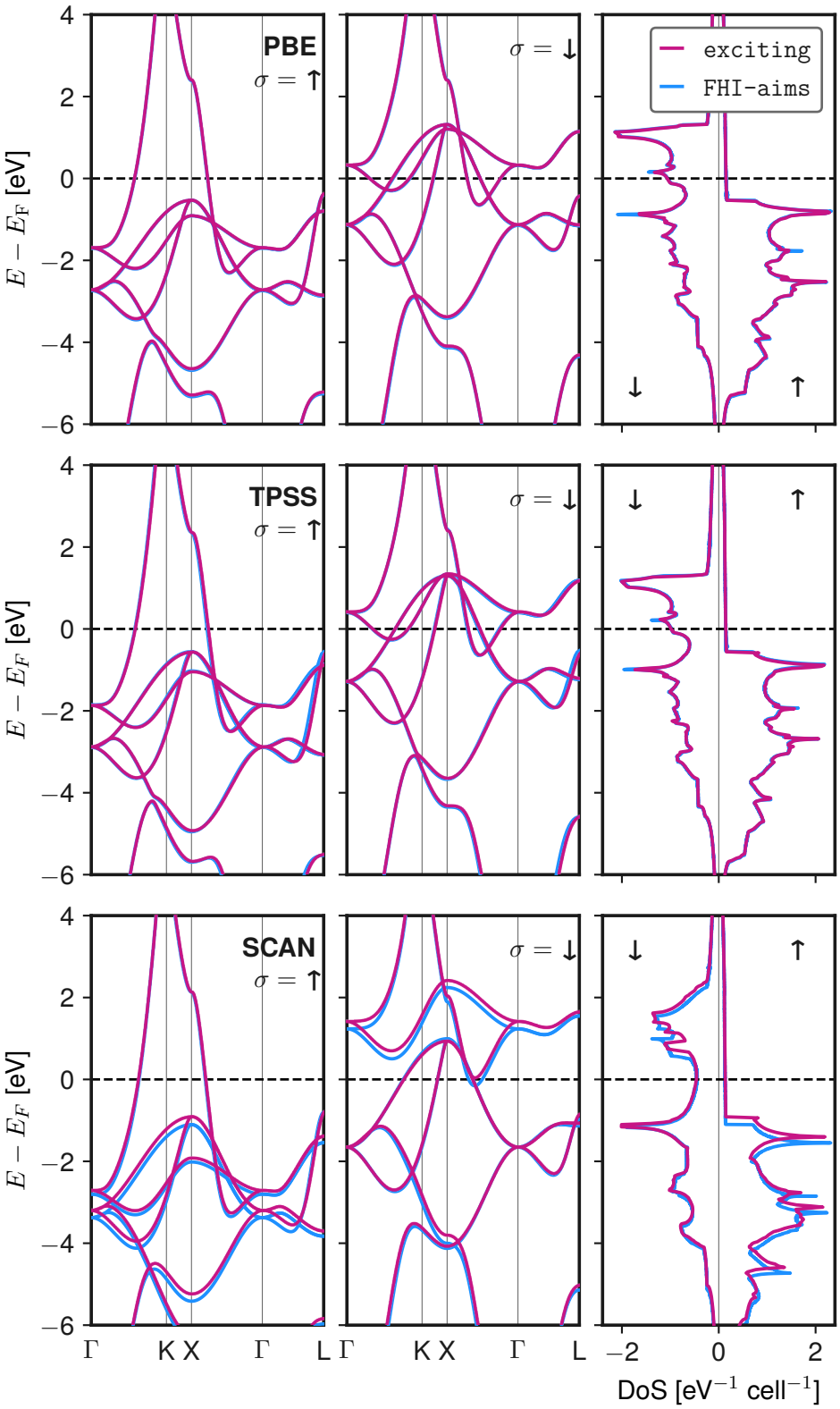

Figure 2.2: Band structure and DoS for FM Co obtained with the PBE (upper panels), TPSS (central panels), and SCAN (lower panels) functional in both `exciting` and `FHI-aims`. The left panels show the spin-up band structure, the ones in the middle the spin-down. The DoS corresponding to spin-down electrons is set negative. The calculations were performed at the equilibrium volume. The dashed line marks the Fermi level.

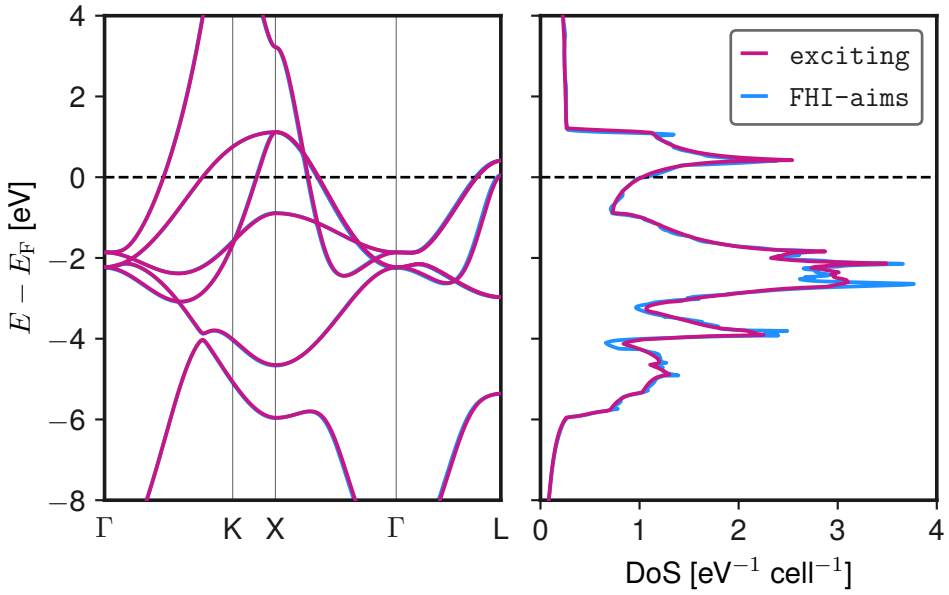

Figure 2.3: Band structure and DoS for NM Co obtained using the HSE functional in both `exciting` and `FHI-aims`. The Calculations were done at the equilibrium volume from Ref. [12], $a_0 = 3.391$ Å. The dashed line marks the Fermi level.

For the HSE functional, the band structure and DoS are compared for the NM phase. The calculation of the DoS especially requires a dense grid of **k**-points in the BZ. In turn, this means that the construction of the non-local potential must be done in a large number of **k**-points, which is not computationally feasible. The electronic structure is thus revolved instead, through the *Wannier interpolation method* [76]. This method uses maximally-localized Wannier functions to interpolate the spectrum of the Hamiltonian. In `FHI-aims` this method is not implemented and the DoS had to be calculated with a reduced grid of **k**-points in reciprocal space. The results are shown in Figure 2.3. The band structure, which is calculated along the same density of **k**-points per path segment as for the other functionals, agrees very nicely. It is the density of states where minor discrepancies become apparent, specifically in the peaks. As the dispersion relation overlaps to such an extent, these deviations are best attributed to the numerical procedure used to construct the DoS, rather than to any genuine difference in the electronic states predicted by the two codes.

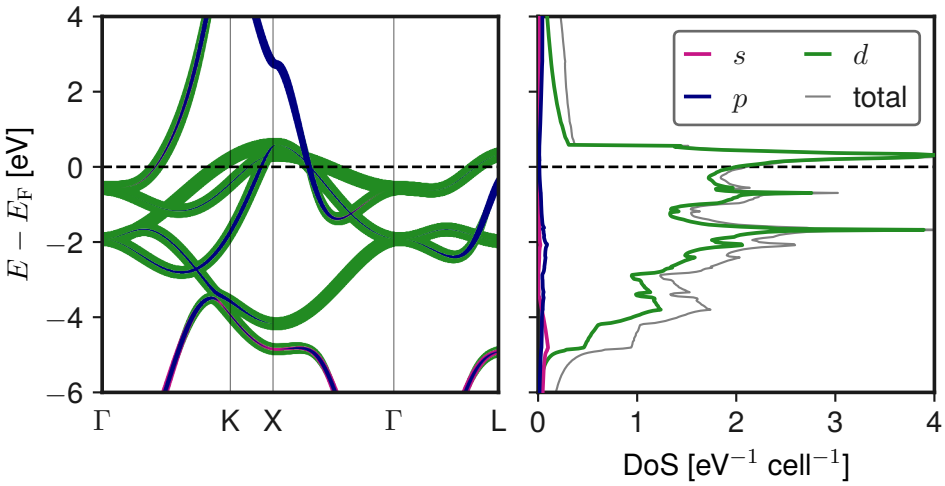

Figure 2.4: Band structure and DoS for NM Co obtained using the PBE functional in `exciting`. The electronic states are l-resolved onto specified orbitals. The dashed line marks the Fermi level.

2.3 Exchange effects on the magnetization

In this section, the effects of different exchange-correlation functionals on the ground-state properties of fcc Co are analyzed. Specifically, the results obtained using PBE, TPSS, SCAN, and HSE are compared within the `exciting` code. To prepare for this, the NM PBE structure of Co is analyzed and prepared as a reference. The corresponding electronic structure at equilibrium volume is visualized in Figure 2.4 through the dispersion relation and density of states, which are additionally l-resolved. As expected from the electronic configuration of Co, the outer d electrons dominate the DoS in the relevant range around the Fermi energy. These bands flatten out partially, causing a peak right above the Fermi level.

Cobalt can be well understood as an itinerant ferromagnet through the picture of Stoner magnetism [77]. The Stoner criterion [78] can aid in the analysis of the magnetic structure. Its claim is that under the condition:

$$I\, D(E_F) > 1\,, \tag{2.3.1}$$

ferromagnetic order is energetically beneficial. Here, I is the Stoner parameter and $D(E_F)$ denotes the NM density of states at the Fermi level. The Stoner parameter can be understood as intra-atomic exchange between electrons [79]. In other words, a large I indicates a larger exchange-energy gain by spin-aligned electrons. This energy "competes" with the kinetic-energy cost of

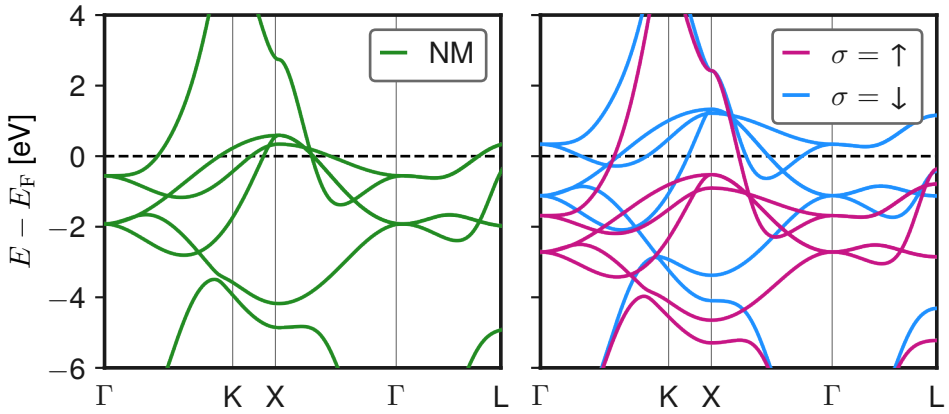

Figure 2.5: Band structure for NM (left) and FM (right) Co obtained using the PBE functional in `exciting`. Both calculations done at respective equilibrium volume. The dashed line marks the Fermi level.

the associated band splitting, which is inversely propotional to $D(E_F)$. The semi-local PBE functional, "aided" by self-interaction error (SIE), captures the highly delocalized d wave functions well. The functional predicts narrow d-bands through the Fermi level that cause the large $D(E_\mathrm{F})$. The KS band structures of both phases are shown in Figure 2.5. The comparison visualizes the spin splitting of the bands, minority-spin states are being partially pushed above the Fermi level, while majority-spin states are lowered in energy. The total unit-cell magnetization of $1.65\,\mu_\mathrm{B}$ is constituted by a magnetization in the interstitial region of $-0.08\,\mu_\mathrm{B}$ and a magnetization of $1.73\,\mu_\mathrm{B}$ within the muffin tin.

Going back to the data of Table 2.1 in order to compare the mGGA and PBE results, it can be seen that the mGGA functionals predict smaller lattice constants for both magnetic phases. SCAN finds a larger magnetization $(1.80\,\mu_\mathrm{B})$ compared to PBE $(1.65\,\mu_\mathrm{B})$ and a larger energy difference between the two phases $(0.52$ eV for SCAN, 0.19 eV for PBE$)$. To simplify, SCAN predicts a "stronger" magnetic phase than PBE or TPSS, and the latter two do not differ meaningfully in terms of magnetization or phase energy difference. TPSS predicts the smallest FM lattice constants, SCAN the smallest NM lattice constant. A complete collection of the NM electronic structure is omitted in this chapter and can be found in Appendix A.1.1, as most arguments can be made with the FM structures. The KS band structure and DoS of the FM phase are seen in Figure 2.6. The data shown in the figure confirms that the TPSS ground state does not differ significantly from the one calculated using PBE.

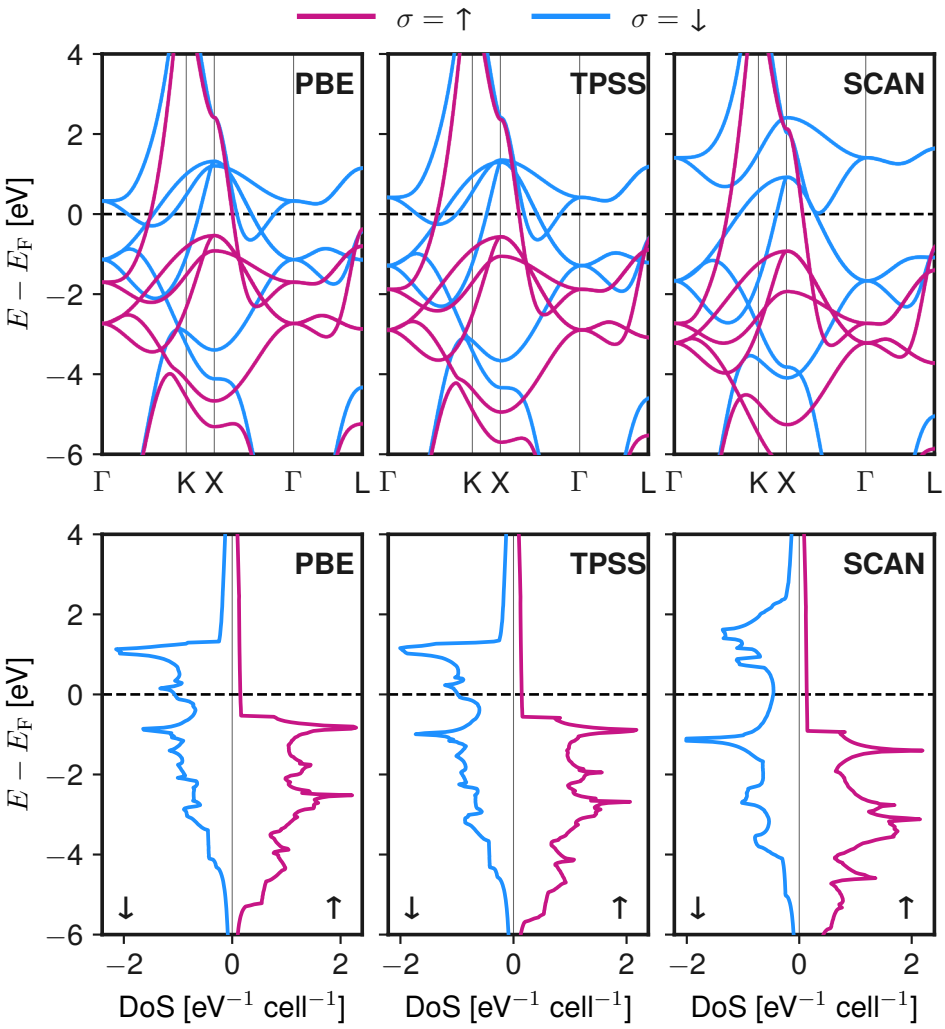

Figure 2.6: Comparison of the spin-resolved band structure (upper panel) and DoS (lower panel) for FM Co using the PBE, TPSS, and SCAN functionals (from left to right) in `exciting` at respective equilibrium volume. States correponding to pin-down electrons are set negative in the DoS. The dashed line marks the Fermi level.

SCAN on the other hand does produce qualitative differences (on top of the quantitative ones mentioned above) to the PBE electronic structure. The spin-up states are again almost uniformly shifted to lower energies, stronger than for TPSS. On the other hand, the minority-spin states are partly shifted upwards. More specifically, they are shifted away from the Fermi level: Occupied bands go lower and unoccupied go higher. For example, the lower of the two conduction bands originating in Γ on the Γ-K section is partially occupied for PBE. In the SCAN results it is consistently larger than 0 eV in energy. This also shifts the peak in the DoS right above the Fermi level to around 0.5 eV. Within the Stoner picture, the bands near the Fermi level are clearly the flat-

test for PBE and the bands of SCAN are noticeably more spread out over a larger energy window. This contributes to a lower $D(E_F)$, which would suggest a weakened FM phase, contrary to the previous observations. A possible explanation the apparent increase of the Stoner parameter I: The stronger exchange effects of SCAN cause a larger energy split between spin-up and spin-down states. "Stronger exchange" refers to the isolated-orbital based exchange enhancement of the mGGA functionals, which is more pronounced in SCAN than in TPSS. This could lessen the (for this material) "benefitial" electronic delocalization due to the SIE.

To complete the analysis of exchange effects, the NM phase is calculated using HSE. The NM electronic structure is compared between the results of the HSE functional with those of PBE and SCAN in Figure 2.7. Compared to both PBE and SCAN, the unoccupied bands of HSE again shift away from the Fermi level. Especially the majority of relevant occupied states is significantly lower in energy as those of even SCAN. This was already a key distinction in the electronic structure of SCAN compared to PBE, where the SCAN functional resulted in a stronger magnetic phase. The low $D(E_F)$ indicates a larger kinetic-energy cost for spin-alignment. Likely this goes along with an increase in exchange-energy gain via an increased Stoner parameter I, though this cannot be judged alone from the NM electronic structure. A FM calculation in `FHI-aims` yielded a unit cell magnetization of $m = 1.86\,\mu_B$ using HSE, an increase when compared to SCAN. Therefore, the spin splitting "wins" the competition with the kinetic energy, *i.e.*, the energy gain of spin-symmetry breaking (represented by I) increased more than the associated band-energy cost, which is inversely proportional to $D(E_F)$.

Preparing for the study of the much more complex La_2CuO_4, it is worthwhile to draw an internally consistent conclusion of the effects of the different functionals. TPSS appears to only slightly increase magnetization in comparison to PBE. SCAN and HSE noticeably increase energy differences between bands and lower the DoS at the Fermi level. Apparently the cause of this, is the strengthening of exchange interaction between the electrons of the same atom, making spin splitting more energetically beneficial and spreading flat bands out over a larger window. As experimental reference of the magnetization, the fcc unit cell magnetization of cobalt was measured to $1.64\,\mu_B$ [80] at 704 K. At this temperature, the hexagonal cobalt transitions to the fcc unit cell. Caution is needed when comparing this value to the ground-state DFT results, as the magnetization was observed to be temperature dependent. PBE

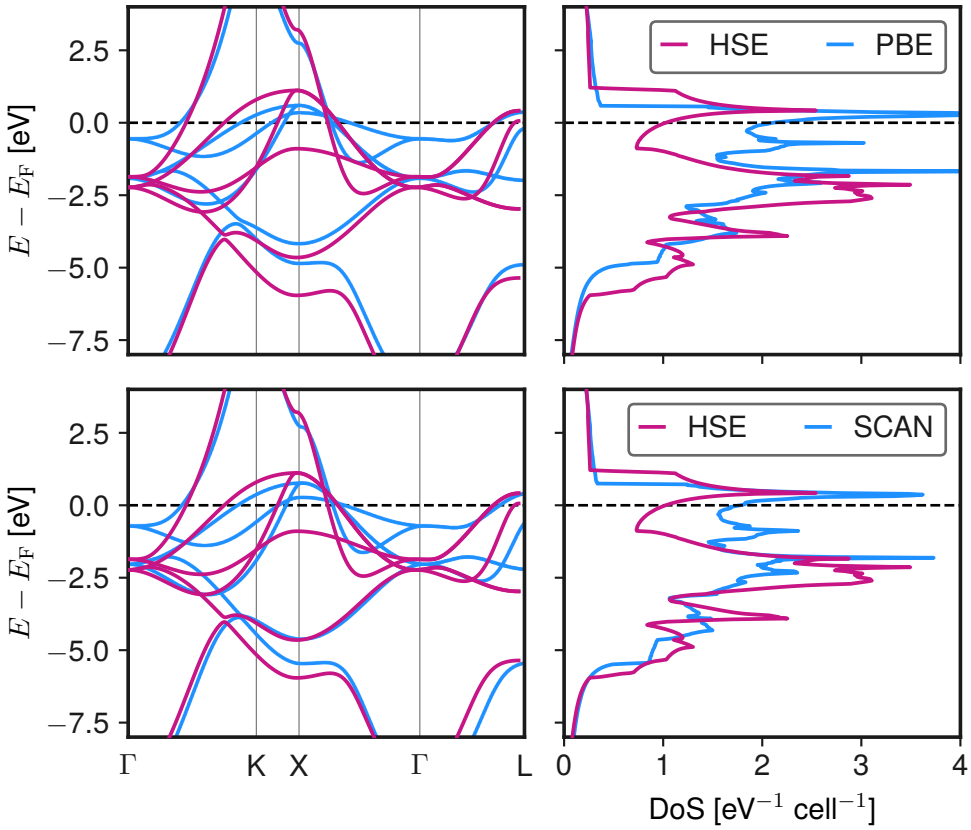

Figure 2.7: Comparison of the NM band structure and DoS of the ground states using the HSE, PBE and SCAN functional in `exciting`. The calculations were performed at equilibrium lattice constants for SCAN and PBE, $a = 3.391$ Å is used for HSE.

and TPSS agree with that value, and PBE has been shown to also capture the magnetization of hexagonal cobalt well [12]. SCAN and HSE both overestimate the magnetization through an increase in intra-atomic exchange energy. It can be argued, that the SIE is a "happy accident" for cobalt: It aids the delocalization of the $3d$ bands, pulling the bands closer together in energy (*i.e.*, towards the Fermi level, as seen in the band structures) and thus giving better results for the magnetization.

Chapter 3

La_2CuO_4 at the PBE level

La_2CuO_4 (LCO) represents the more intricate system addressed in this thesis, combining a larger unit cell with richer geometric, electronic, and magnetic substructure than elemental cobalt. To manage this complexity, the discussion is divided into two parts. This chapter focuses on the practical aspects of the calculations and on reference results obtained with the PBE functional, while the influence of more advanced exchange–correlation functionals is analysed in Chapter 4. The computational workflow largely follows the same methodology established for cobalt in Chapter 2. The geometry is again optimized through the equation of state, and the KS electronic structure is analyzed via the band structure and DoS. The antiferromagnetic ground state of LCO is analyzed with the intent of creating a reference for other functionals.

3.1 Crystal structure

Before electronic or magnetic properties may be studied, it is necessary to get an overview about the structural properties of LCO. Characteristic for the geometric structure and physical properties of LCO as a cuprate are the CuO_2 planes formed by corner-sharing CuO_6 octahedra that constitute the crystal. Layered between the copper-oxide planes, are insulating multilayers of LaO (different for other cuprate compounds). In doped cuprates, where La is partially replaced by for example Sr or Ba, these spacer layers act as charge reservoirs, controlling the hole density in the CuO_2 planes and causing both conventional and superconductivity [81]. The present work, however, focuses exclusively on the undoped parent compound La_2CuO_4.

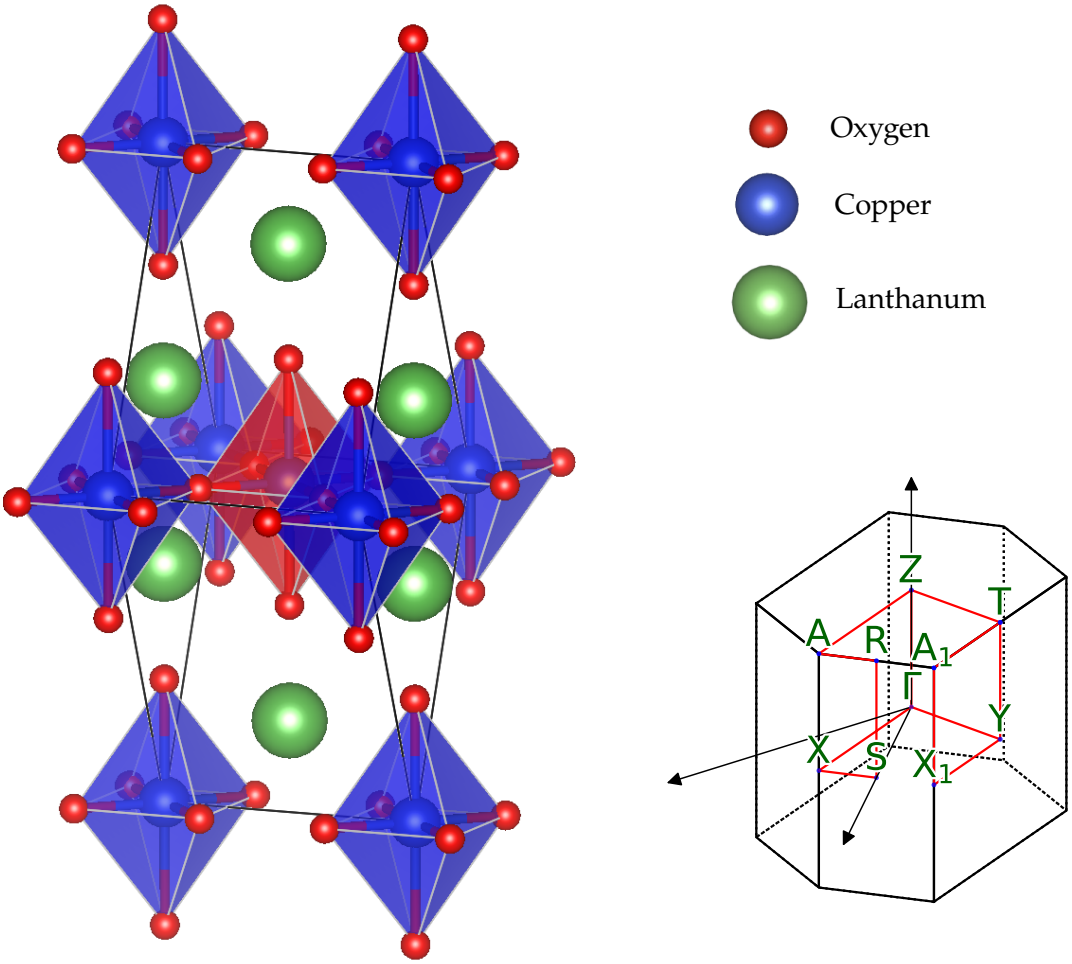

Figure 3.1: Left: Orthorhombic supercell of HTT La_2CuO_4. Blue / red CuO_6 octahedra belong to the two antiferromagnetic sub-lattices. Right: First Brillouin zone and special-point path of the orthorhombic HTT supercell, as suggested in Ref. [82].

The work presented in Ref. [83] investigates structural transitions of LCO with respect to temperature and outlines specifically three geometric phases. Historically [84] LCO was first found to crystallize in a tetragonal K_2NiF_4-type structure of space group $I4/mmm$. The referenced study reaffirms the later finding, that this is a high temperature (tetragonal) phase (HTT), which has two lower temperature counterparts. One is the meta-stable T'-phase of the same space group. It differs from the other tetragonal phase by a larger unit cell volume and shifted oxygen positions. The T' phase was synthesized and measured at 312 K via X-ray powder diffraction. Upon temperature increase, T' was found to transition to HTT at 723 K. When cooled to around 323 K it underwent another transition, now to an orthorhombic unit cell of space group $Cmce$, the low temperature orthorhombic (LTO) phase. Characteristic for it is the tilting of the octahedra in the yz-plane against each other.

This work focuses on the study of La_2CuO_4 in the HTT crystal structure, as time constraints demand a focus on one of the phases. While T' is a specific focus of research [85–87] due to its possibility of electron doping, the LTO phase with its hole doping has historically been the more investigated phase. The reason why HTT is still chosen over the LTO phase is mainly computational. Specifically for DFT calculations, the tilting of the octahedra taking place in the LTO phase causes no qualitative changes in electronic and magnetic structure of the system, with reference to the findings of Ref. [8]. What LTO does cause, is an increase in computational cost — the unit cell of LTO requires two copper basis atoms to faciliate the tilting, for HTT one copper atom suffices. As each copper atom needs four corresponding oxygen and two lanthanum atoms, LTO calculations require twice the number of atoms as HTT. This is exacerbated by the fact, that the material is an antiferromagnet. Because of this, the unit cell consists of two identical sub-lattices with opposing spin. Together, this means that the HTT unit cell for the antiferromagnetic phase is made up of 14 atoms in total, whereas LTO requires 28. The cost of this outweighs any insight gained through the included geometric tilting. To capture the physical antiferromagnetic ordering, an orthorhombic super cell is used instead of the conventional cubic cell. Figure 3.1 visualizes the HTT crystal structure used for calculations in this chapter, together with the BZ path and spin ordering. In Chapter 4, HSE calculations are conducted in the primitive 7-atom unit cell.

3.2 Computational details

The geometry was optimized using the 14-atom unit cell for both (NM and AFM) magnetic phases. The parameters were chosen to convergence the magnetic moments up to $0.01\,\mu_B$ and total energies up to 0.01 eV/atom. This leads to a **k**-point grid of $10\times10\times10$. Occupations were calculated through the tetrahedron method of Ref. [73], as it provided a more stable and faster convergence of the magnetic phase than Gaussian broadening. As a plane-wave cutoff $R_{MT}G_{max} = 8$ was chosen, with $G_{maxVR} = 22$ stabilizing this value. The second-variational treatment of spin required 500 empty states for convergence. Species, input, and output files of all performed calculations are also included in the NOMAD repository that is available under the following link: https://dx.doi.org/10.17172/NOMAD/2025.07.03-1. As muffin tin radii for lanthanum, copper and oxygen the values 2.20, 2.00 and $1.45\,a_B$ were used. The equilibrium volume of the unit cell is again found via a Birch-Munarghan

fit in the equation of state. Following this, at the equilibrium volume, the ratio of the two lattice constants a and c is varied. Through a polynomial fit, the energy-minimizing ratio is found. Different as in Co, there are atomic positions in the LCO unit cell that are not fixed by crystal symmetry. Thus, atomic forces become a relevant part of the optimization, and the atomic positions are fully relaxed in every calculation. Such a force relaxation employs repeated SCF cycles at varying geometries within `exciting`, with a subsequent optimization for total energy. These cycles are done in succession, with the previous density serving as the starting point. In the case of one of those trial geometries destabilizing the AFM phase, a new set of magnetic fields is applied at every new SCF cycle.

3.3 Unit-cell optimization

Different magnetic phases typically induce a different equilibrium geometry, as was seen for example in Section 2.2 for cobalt. Though the analysis of the nonmagnetic equilibrium geometry is typically not included in recent DFT studies of the system [8, 88, 89], its inclusion could add more details to the understanding of both the magnetic and the electronic structure of LCO. Figure 3.2 shows the geometry optimization for the unit cell. Details regarding the magnetic and electronic KS structure are not included in this section and are treated later in the chapter. Noticeable in the results, is the rather small effect magnetization appears to have on the geometry. The minimized energies of the two phases only have a difference of $\Delta E_{\mathrm{M}} \approx 0.06$ eV (per cell), and thus below the converged energy range of 0.01 eV / atom. The AFM phase obtained by PBE can therefore not be said to be stable. This is further supported by the detailed results summarized in Table 3.1 — the optimized geometry of both magnetic phases are practically identical. The table includes DFT results from a `VASP` study of the AFM system from Ref. [88]. The `exciting` lattice constants are slightly larger, though no more than 0.007 Å. When comparing this to experimental data published in 2011 in Ref. [83], `exciting` results are slightly underestimating the unit-cell size. It is important to notice, that the experimental measurements were conducted at a temperature of 1073 K, which might explain a larger unit cell. Another relevant quantity for characterizing the geometry of the system is the Cu-O distance d. Again, results from `exciting` are slightly larger than the `VASP` counterpart. However, the experimental value of Ref. [83] is actually more than 0.2 Å smaller than the theoretical ones.

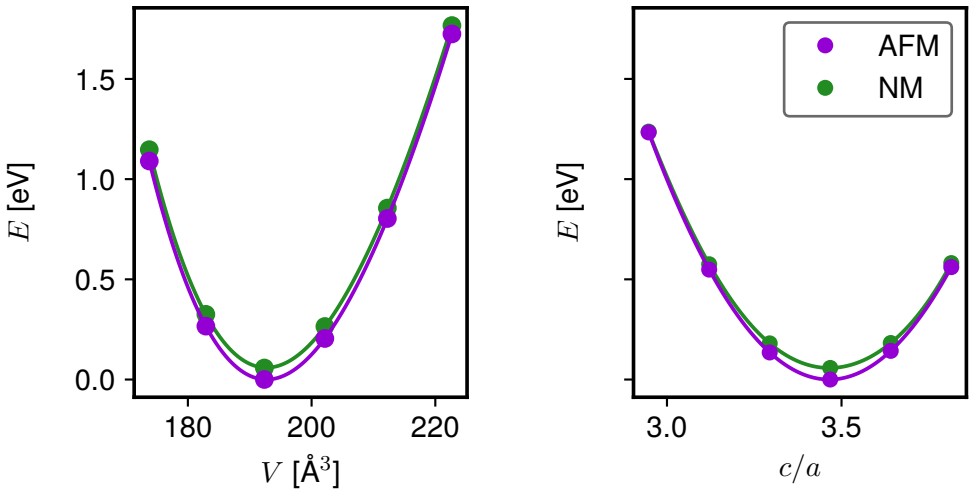

Figure 3.2: Geometry optimization of the LCO unit cell obtained with **exciting** using the PBE functional. Left panel: EoS for the two magnetic phases. Calculated data are fitted with Birch-Munarghan EoS. Right panel: Optimization of the c/a ratio. Here, a polynomial fit of 5th order is used. The fit parameters are found in Appendix A.2.2.

Table 3.1: Resulting equilibrium geometries for LCO in **exciting** for both magnetic phases using the PBE functional. Compared are the equilibrium lattice constants a_0, c_0 and their ratio c_0/a_0, the 14 atom unit cell volume V_0, as well as the copper-oxygen distance d_0. Results are compared with another DFT study of the AFM phase using the **VASP** code also using PBE Ref. [88] as well as to experimental data from Ref. [83].

Phase	Method	a_0 [Å]	c_0 [Å]	c_0/a_0	V_0 [Å^3]	d_0 [Å]
NM	**exciting**	3.817	13.227	3.466	192.70	2.462
AFM	**exciting**	3.817	13.226	3.465	192.71	2.459
	VASP [88]	3.810	13.220	3.470	192.08	2.431
	Expt. [83]	3.833	13.313	3.473	195.58	2.277

3.4 The nonmagnetic phase

The focus shits onto electronic structure in this section. As a compound material, insights can be gained by separating electronic contributions from the different elements. A species-resolved band structure is contained in Figure 3.3. For a deeper investigation, the l-resolved bands and DoS are also included in the figure. The figure validates several statements about the nature of LCO. The lanthanum states form flat bands about 3 eV above E_F with little contribution from neither Cu nor O.

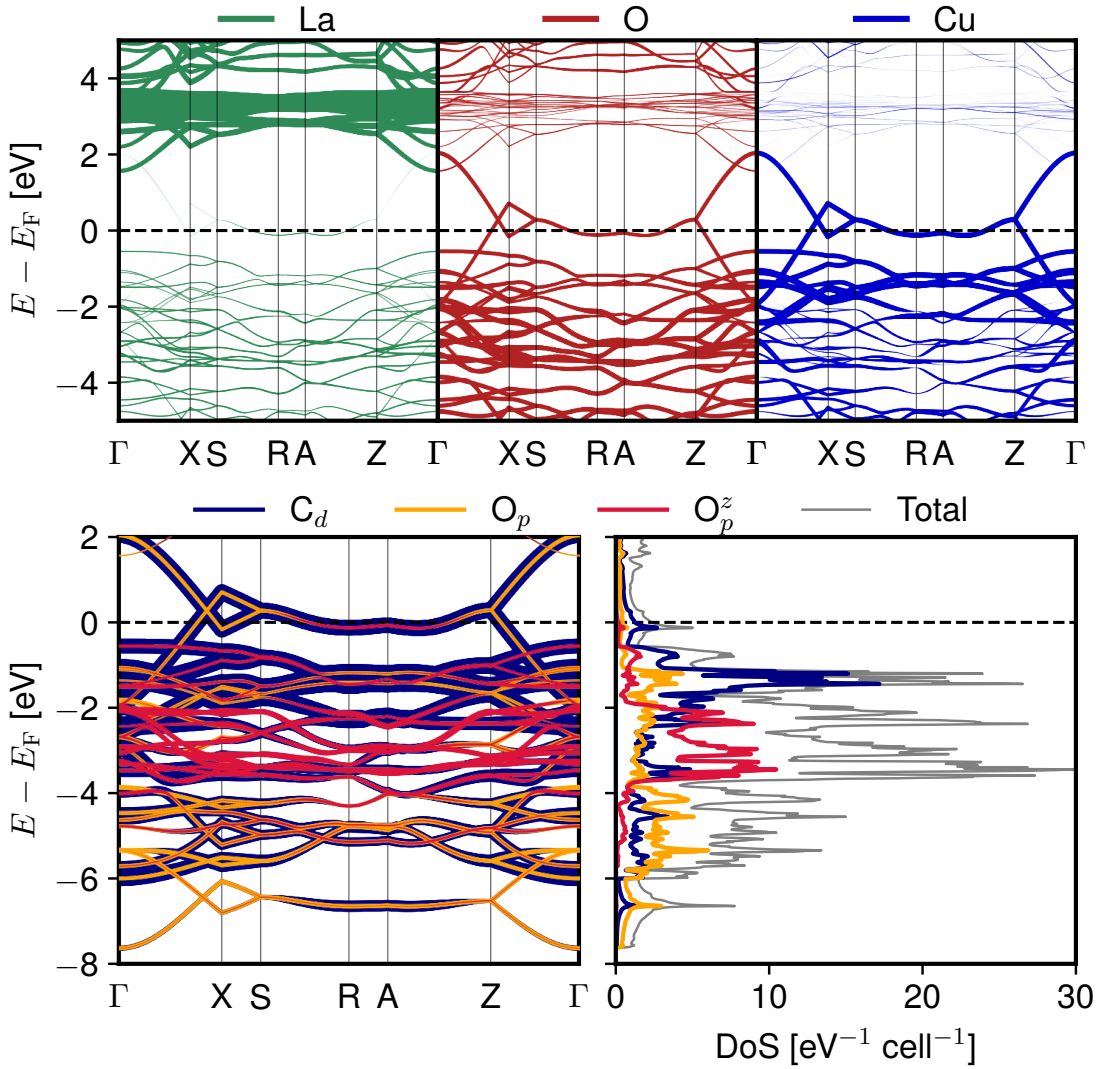

Figure 3.3: Electronic structure of nonmagnetic LCO at equilibrium geometry (see Section 3.3) using the PBE functional. Upper panel: Species-projected band structure through a reduced path (linewidth scales with contribution weight). Lower panel: Density of states and band structure projected onto O and Cu atoms with selected l-channels; planar and apical oxygen atoms are distinguished, the latter denoted O^z.

Specifically, the La states bond very little with either and therefore justify the classification of La as a charge reservoir. Additionally, the nature of LCO as an antiferromagnetic Mott insulator can be recognized most easily by looking a the band passing through the Fermi level. It is the spin-splitting of this half-filled d-copper band, that opens up the electronic band gap in the AFM phase. Precisely, this band corresponds to the hybridization of the copper $3d_{x^2-y^2}$ orbital with the oxygen $2p_{xy}$ orbital, see Ref. [90]. The band flattens out through the S-Z path, highlighting the anisotropy of the material, as in Γ-X it disperses across 4 eV. As an additional detail, a distinction is made be-

tween planar oxygen, and apical atoms O^z, the corresponding character in the p-channel is also included in Figure 3.3. The band crossing the Fermi-level is dominated by planar oxygen contributions in the NM case, though the apical oxygen also has non-negligible contribution.

3.5 The antiferromagnetic phase

Through opposing, local magnetic fields inside the muffin tin regions, an AFM order is induced in the structure. A magnetic moment can be assigned to the individual copper atoms (or any other) through integration of the spin-resolved densities inside the muffin-tin radii. This creates ambiguity, as a different integration radius could change the value of the magnetization. However, K. Pokharel and coworkers (Ref. [8]) have shown that for radii within 1-3 Å, the integration radius has little impact on the resulting magnetization of the copper atoms. For reference, the muffin-tin radius for copper was chosen as $R_{\mathrm{MT}} = 2.0\,a_{\mathrm{B}} \approx 1.06$ Å, which falls into the investigated range.

The resulting dispersion of the magnetic calculation is compared to the previous, NM case in Figure 3.4. The half-filled Cu_d band now splits, causing the Fermi level to be actually unoccupied, with a small band gap of 0.06 eV opening up. The valence band maximum (VBM) and conduction-band minimum (CBM) are highlighted, the CBM notably being positioned slightly off of the high-symmetry point A. Aside from this, the electronic structure remains largely unchanged. The sensitive band structure around the Fermi energy demonstrates the necessity for a high resolution of the spectrum in energy space, as too large energy broadening would "smear over" the gap and result in metallic behavior. Similarly, both the eigenvalues and E_{F} need to be well converged, which demands a dense **k**-point density. Copper carries the most significant amount of magnetization, a magnetic moment of $m_{\mathrm{Cu}} = 0.28\,\mu_{\mathrm{B}}$. The magnetization of lanthanum is negligible at $\approx 0.001\,\mu_{\mathrm{B}}$, while the planar oxygen atoms are not magnetized at all. The apical oxygen on the other hand carry a small moment of $m_{\mathrm{O}^z} = 0.01\,\mu_{\mathrm{B}}$, aligned in opposition to their corresponding copper atom. Consistent with the conclusion of Section 3.3, PBE produces only a weak AFM phase, as in a small band gap, and fails to describe a true Mott insulator. Instead, LCO is predicted to be closer to a semimetal, with the underestimated gap stemming from insufficient spin splitting, a possible sign of underestimated exchange interactions. Based on the increased exchange splitting observed with mGGA and hybrid functionals in Chapter 2, these functionals are likely to provide a more accurate description.

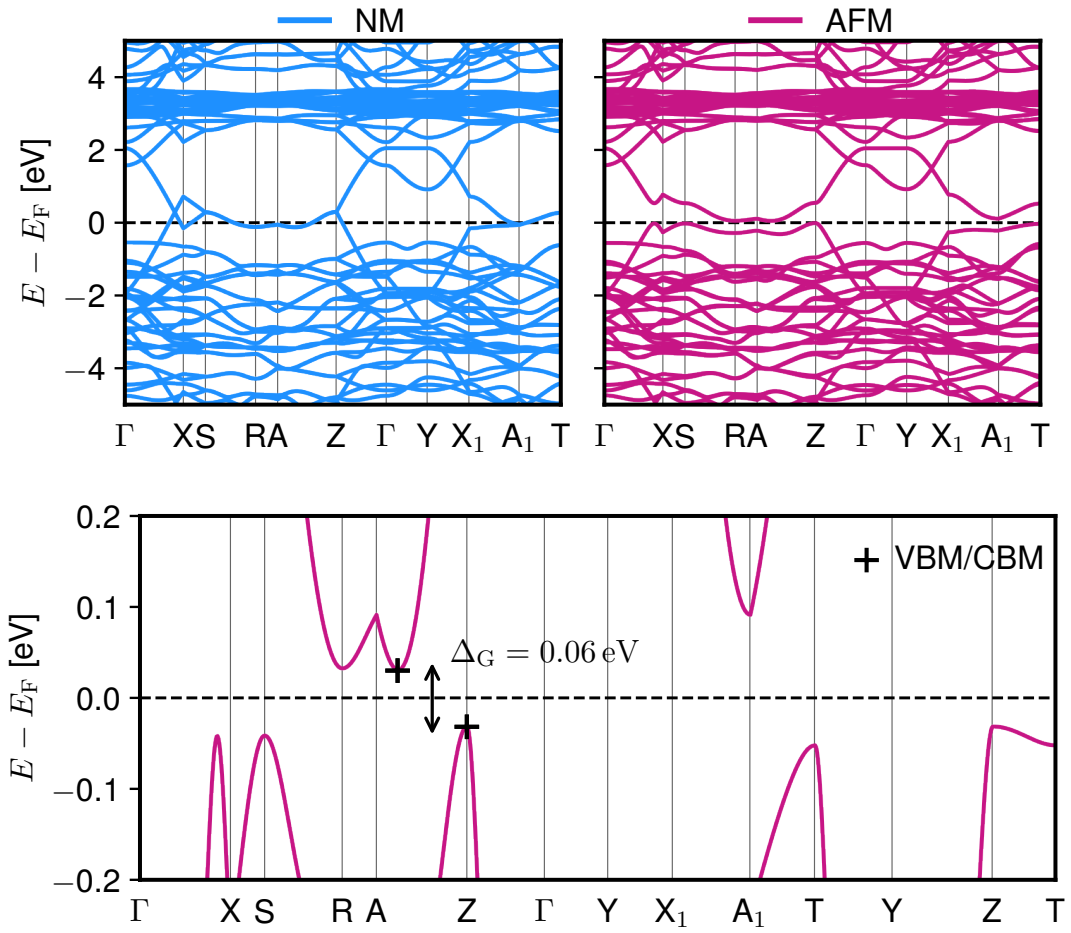

Figure 3.4: Upper panel: Comparison of the band structure of the NM (left) and AFM (right) phase of LCO at the respective equilibrium geometries using the PBE functional. The spin degree of freedom is suppressed due to the symmetry between spin channels. Lower panel: AFM band structure in an energy window near the band gap, highlighted with VBM and CBM. The dashed line marks the Fermi level.

Chapter 4

La_2CuO_4 towards the Top of Jacob's Ladder

This chapter extends the analysis of La_2CuO_4 (LCO) to include exchange-correlation (XC) effects. A similar set of functionals as in Chapter 2 is used, with LSDA and r2SCAN now included, to investigate specifically the magnetic structure of the AFM ground state. Previously, it was the exchange enhancement of SCAN, or the non-local exact exchange, leading to an overestimation of exchange splitting. Different than for cobalt, the magnetism of LCO cannot be understood through a band picture and requires an almost microscopic view of individual bonds, as will be argued throughout this chapter.

The main observables for the LCO system, besides its geometry, are the electronic band gap and the copper magnetic moments. Regarding the latter, this work will use the value featured in Ref. [91] of $(0.60 \pm 0.05)\,\mu_B$ as the experimental value, which was obtained by neutron diffraction and scattering [92–94]. The value chosen for the band gap is explained a bit further. Optical-absorption experiments report a gap of about 2 eV [95, 96]. In the referenced papers, the first peak in the absorption spectrum is reported as the gap. S. Ono and coworkers measured the band gap via the Hall coefficient at 0.89 eV [97]. The authors argue, that the inital onset of the absorption spectrum is a better measure for the fundamental gap of the material. When adjusting for the temperature, the authors state range of 0.9-1.3 eV for the band-edge gap. Accordingly, and in line with other recent DFT studies of LCO [8, 88], this will also be the referenced experimental range in this chapter. Unless stated otherwise, the same computational parameters for DFT calculations as in Chapter 3 are used.

4.1 LSDA, Delocalization, and SOC

The LSDA struggles with correctly describing the highly localized (in real space), isolated (in energy space) copper $d_{x^2-y^2}$ band of LCO [7, 98]. The SIE inherent to the functional causes delocalization to be energetically beneficial, favoring an over-hybridized state with the $d_{x^2-y^2}$ orbital "bleeding over" into the oxygen ligands. This in turn decreases the magnitude of copper moments (if a stable magnetic order is even predicted), as it is the copper-$3d$ orbitals that polarize, as shown in Section 3.5. Furthermore, the weakened on-site Coulomb interaction pulls the split copper conduction and valence band of Figure 3.4 together, resulting in an occupied Fermi level. Figure 4.1 shows the corresponding electronic structure. The final copper moment of the calculation is $m_{\mathrm{Cu}} = 0.15\ \mu_{\mathrm{B}}$, lower than the PBE moments of $m_{\mathrm{Cu}} = 0.28\ \mu_{\mathrm{B}}$. While PBE also suffers from SIE, its gradient-dependent exchange enhancement, see Section 1.4.1, improves the results compared to LSDA. The reduction in total energy by the AFM phase is negligible for both functionals. For the LSDA the reduction is 0.02 eV compared to the 0.06 eV (per cell) for PBE, which corresponds to an energy difference less than the converged 0.01 eV/atom for both functionals.

A particular advantage of studying LSDA over PBE and other GGA functionals in this context, is its compatibility with the inclusion of SOC effects. GGA functionals suffer from numerical instability when extended to the non-collinear spin treatment, as argued in Section 1.4.1. Nevertheless, these effects are typically included in DFT calculations of the LCO system [8, 88, 89] conducted in other code packages. For the `exciting` calculation, LSDA offers the possibility of showcasing SOC effects on the material. Figure 4.1 shows that the only the $4f$ La bands change meaningfully upon the inclusion of SOC, with the bands widening slightly. Magnetic copper moments slightly decrease to $0.14\ \mu_{\mathrm{B}}$ (without SOC $0.15\ \mu_{\mathrm{B}}$), the total energy of the ground state decreases by 1.25 eV ≈ 0.09 eV/atom, larger than the convergence threshold used for the total energy of 0.01 eV/atom. This change in total energy could affect the EoS and its fit, and thus also affect the geometry. However, the lattice constants calculated in Section 3.3 were in good agreement with the referenced, SOC-included, data. This suggests a uniform shift in total energy in the EoS. As there is no substantial impact on the electronic or magnetic structure, as argued above, SOC effects may be disregarded in this study.

Before turning to the more advanced functionals, it is constructive to briefly consider how the limitations of the LSDA have been adressed in the literature.

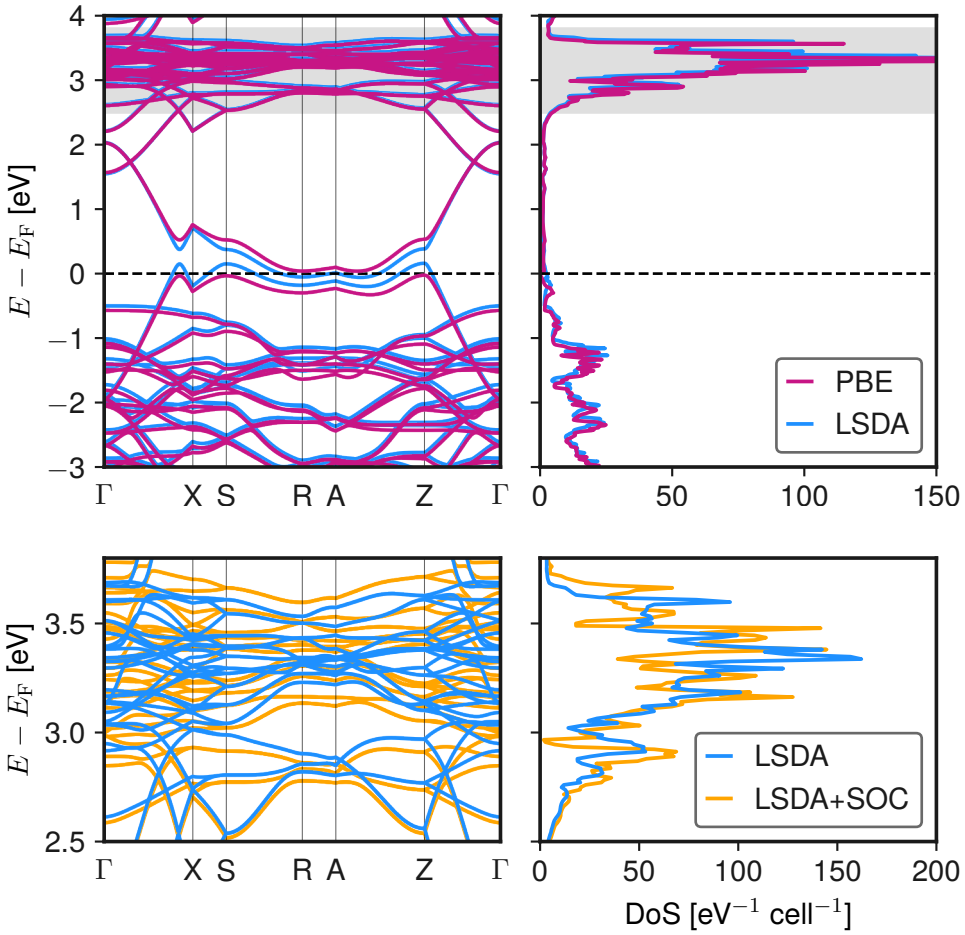

Figure 4.1: Band structure and DoS of AFM LCO obtained using `exciting`. Compared are LSDA, PBE and LSDA with SOC effects. Top panel: LSDA and PBE. Bottom panel: LSDA including spin-orbit coupling within the shaded energy range. The dashed line marks the Fermi level.

This exploration will help to both draw conclusion from the various predictions of different functionals, and make arguments about the resulting electronic and magnetic structure. Various methods that offer remedies to the described issues related to the LSDA have been proposed. One approach is to include an on-site Hubbard U interaction term in the DFT+U scheme [99]. The additional exchange energy localizes the $3d$ orbitals at the copper site and helps open the band gap. The authors of Ref. [99] report a gap of 1.65 eV and a copper moment of $0.62\,\mu_B$. A similar, energy-focussed approach, is correcting the SIE for the individual orbitals as outlined in Ref. [100]. Numerical methods, that constraining the calculation to enforce localizhation, such as a Gaussian basis set, also have shown success in describing the ground state. The results of these approaches are summarized Table 4.1.

Table 4.1: Band gap and copper magnetic moment for AFM LCO calculated in the present work using `exciting` with LSDA and PBE, as well as selected DFT literature results with different methodologies and experimental data.

Methodology	Δ_G [eV]	m_{Cu} [μ_B]
`exciting`@LSDA	0.00	0.15
`exciting`@PBE	0.06	0.28
Self-interaction corrected LSDA [100]	1.04	0.47
Gaussian orbital basis + LSDA [101]	0.60	0.43
LSDA+U [102]	1.65	0.62
Expt. [91, 97]	1.1 ± 0.2	0.60 ± 0.05

This summary supports, that an opened band gap and localized $3d$ bands go hand-in-hand. And while the mentioned procedures improve the situation for the LSDA for the specific properties of LCO, it is their specificity which makes them useful for understanding hand-picked properties of materials. The same specificity makes them not practical for general applications, and thus they serve tools for analyzing, and finding, more modern exchange-correlation functionals.

4.2 Meta-GGA functionals and isolated orbitals

The potential benefit of mGGA functionals in this study, is the mitigation of the inherent SIE to (semi-)local functionals for isolated states. The discussed mGGA functionals achieve this, by defining an isolated-orbital indicator α, based on the kinetic energy density, which determines compensatory exchange energy. In the context of LCO, this can have similar effects to the localization methods showcased in the previous section. The unstable nature of mGGA functionals, specifically regarding this indicator α, made adjustments to the SCF cycle necessary. The convergence criterion is modified to be based exclusively on total-energy changes, specifically requiring only a difference smaller than $5 \cdot 10^{-4}$ Ha $\approx$ 1 meV between iterations to end the SCF cycle. This modification will be validated in Section 4.3.

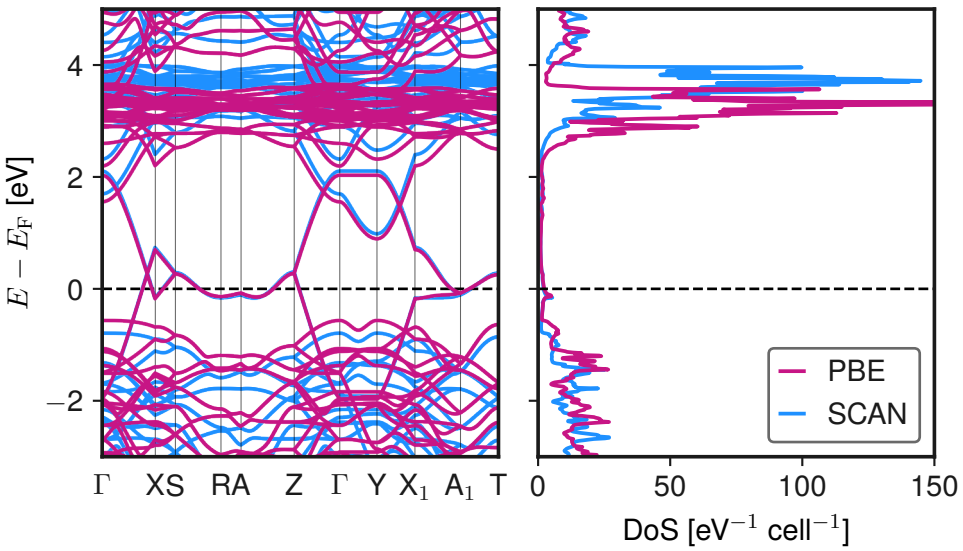

Figure 4.2: Band structure and DoS of NM LCO at the PBE and SCAN level at equilibrium geometry. The dashed line marks the Fermi level.

The effects of exchange-enhancement are most clear in the comparison of results between SCAN and PBE. The effect can already be seen in the NM phase (see the band structure in Figure 4.2). SCAN pushes the conduction band up and valence band down, isolating the band crossing the Fermi-level. This, in turn, makes confinement to the copper site more energetically viable, with the described consequences for the real-space extent of the orbitals. Lastly, the spin-induced symmetry breaking increases electronic band gap by, as described previously, splitting the $3d$ band.

In addition to SCAN, antiferromagnetic calculations are done also for TPSS and r2SCAN. The band gap, magnetic moments, as well as energy difference between the AFM and NM phase of LCO are summarized in Table 4.2.

Table 4.2: Band gap, Δ_G, copper magnetic moment, m_{Cu}, and energy difference between the phases, ΔE, for AFM LCO calculated with `exciting` for different functionals. ΔE is computed between NM and AFM at respective optimized geometry. Also included are band transition energies between select **k**-points. $\widetilde{A}$ denotes the position of the CBM of PBE and TPSS, $\widetilde{A}_1$ the VBM of SCAN and r2SCAN.

XC	Δ_G [eV]	m_{Cu} [μ_B]	ΔE [eV/atom]	Z→$\widetilde{A}$ [eV]	$\widetilde{A}_1$→R [eV]
LSDA	0.00	0.15	< 0.01	< 0.0	< 0.0
PBE	0.06	0.28	< 0.01	0.06	0.16
SCAN	1.08	0.54	0.02	1.19	1.08
TPSS	0.34	0.38	0.02	0.34	0.39
r2SCAN	0.82	0.49	0.02	0.88	0.82
Expt. [91, 97]	1.1 ± 0.2	0.60 ± 0.05			

For the purposes of this analysis, the biggest distinguishing feature of the three different mGGA functionals is the methodology of isolated-orbital detection, see Section 1.4.2. For the cobalt system in Chapter 2, TPSS predicted results more comparable to PBE than to SCAN, due to a smaller impact of the exchange enhancement. For the LCO system on the other hand, TPSS already makes a significant improvement upon PBE. Though the copper moments of $0.38\,\mu_B$ are only modestly increased over the PBE moments of $0.28\,\mu_B$, the band gap significantly opens up to a value of 0.34 eV. r2SCAN regularizes the dependence of the SCAN exchange on α, which weakens its effect. Both the copper moments, $0.49\,\mu_B$, and electronic band gap, 0.82 eV, are smaller than the experimental ones, though significantly improved upon TPSS and PBE. The values of these properties obtained using SCAN, 1.08 eV and $0.54\,\mu_B$, can be considered to agree best with experiment overall. When it comes to the energy difference between the two magnetic phases, all three mGGA functionals greatly increase the total-energy difference between AFM and NM to 0.02 eV/atom, and thus stabilize the AFM ground state. Figure 4.3 shows the electronic structure with the positions of the VBM and the CBM highlighted. To be noted, is that the position of both changes for the SCAN functionals with respect to TPSS and PBE, who share the positioning. Similar DFT investigations find a CBM or VBM off of high-symmetry points for the HTT structure. The transition energies for the two pairs of CBM and VBM for the four functionals are also found in Table 4.2.

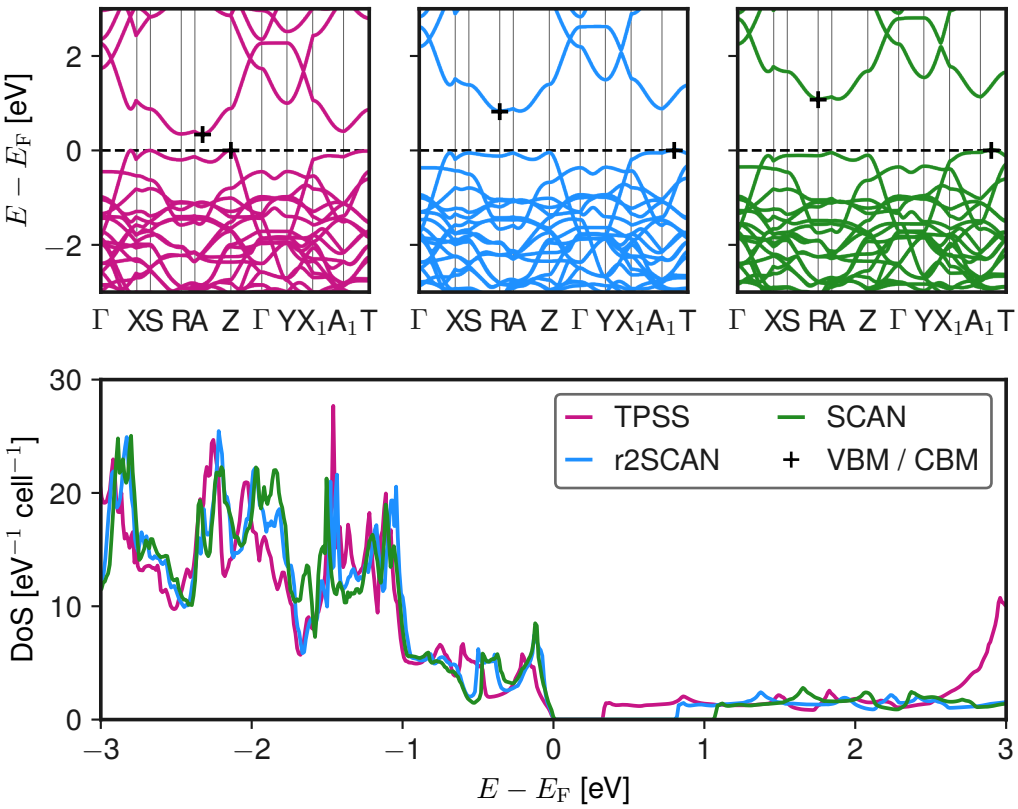

Figure 4.3: Band structure (upper panel) and DoS (lower panel) of AFM LCO obtained with the TPSS, r2SCAN, and SCAN functional in `exciting`. The Fermi energy is set at the VBM.

4.3 Benchmark of the results using `FHI-aims`

The sensitive nature of the LCO ground state warrants precautions when trying to generalize the findings of the past two sections to the discussed functionals. Furthermore, the adaptations that had to be made to the convergence criteria of the SCF cycle, in order to achieve convergence of the mGGA functionals, require justification. Mirroring the procedure of Chapter 2, the results of Section 4.2 for LCO are validated via repetition of the calculations in `FHI-aims`. Focus will be given to the AFM ground state, specifically the two observables used for its quantification: The electronic band gap and copper magnetic moments. The r2SCAN functional was not implemented with the available version of `FHI-aims` and therefore is not included.

The mentioned data is summarized in Table 4.3. The `FHI-aims` band gaps qualitatively confirm the `exciting` results. The band gap of TPSS (SCAN) is slightly smaller (larger) using `FHI-aims` when compared to the `exciting` values, 0.29 vs. 0.34 eV (1.11 vs. 1.08 eV). The LSDA could not stabilize an

Table 4.3: Band gap and copper magnetic moment of AFM LCO calculated with `exciting` and `FHI-aims` for several functionals.

XC	Code	Δ_G [eV]	m_{Cu} [μ_B]
LSDA	`exciting`	0.00	0.14
	`FHI-aims`	0.00	0.00
PBE	`exciting`	0.06	0.28
	`FHI-aims`	0.06	0.26
TPSS	`exciting`	0.34	0.38
	`FHI-aims`	0.29	0.34
SCAN	`exciting`	1.08	0.54
	`FHI-aims`	1.11	0.50
Expt. [91, 97]		1.1 ± 0.2	0.60 ± 0.05

AFM order in `FHI-aims`. A possible explanation for discrepancies may lie in the definition of the copper magnetic moments itself. As outlined in the previous chapter, there is ambiguity in terms of the region of space that constitutes the copper atom and how a magnetization is assigned to it. Once decided on a muffin tin radius, the spin-resolved densities are integrated in `exciting`, the difference amounting to the moment. `FHI-aims` does not partition space into muffin-tin radii and interstitial region. Instead, the moments are calculated through a Mulliken population analysis [103]. This method is explicitly basis-set dependent through the overlap matrix, and could account for the discrepancy in moments. The two dispersion relations shown in Figure 4.4 agree remarkably well for such a complex system, even for SCAN. This analysis validates the reduction in accuracy in SCF convergence criteria with respect to the the observed quantities.

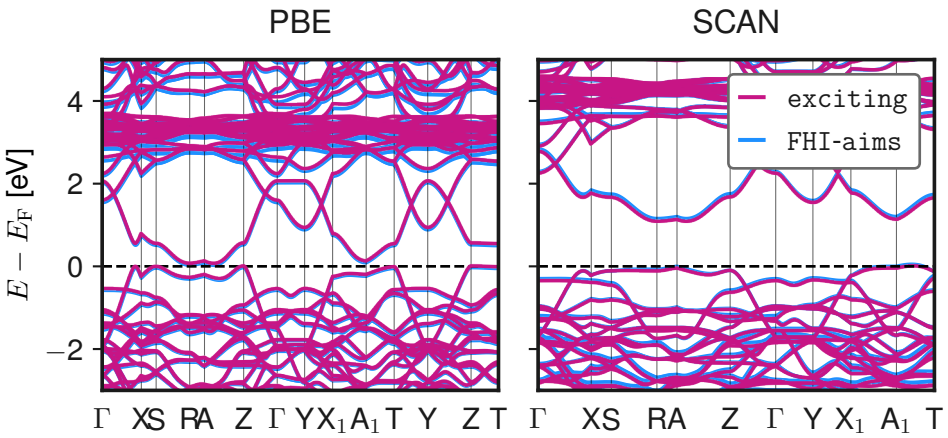

Figure 4.4: Band structure of AFM LCO obtained using **exciting** and **FHI-aims** calculated with PBE (left) and SCAN (right) at the **exciting** equilibrium geometry. The dashed line marks the Fermi level.

4.4 Hybrid-functional calculations

The perspective of this chapter thus far has been centered on the localization of the copper orbitals. Hybrid functionals offer a portion of exact, SIE-free exchange *mixed* into the functional. This leads to the prediction that HSE should find a strong magnetic insulating phase for LCO. Not only should the non-local exchange induce localization, the introduction of a fraction of derivative discontinuity into the exchange-correlation functional should greatly open up the band gap. As has been mentioned, the SV non-local potential is not yet implemented in **exciting**. Therefore, this cannot be explicitly tested in this code package. Moreover, as the 14 atom unit cell required for AFM calculations of LCO poses a great computational cost. On top of this, the non-local potential is found to possess a slower **k**-point convergence compared to PBE. A silver lining could be, that the insulating HSE ground state might not be as sensitive to the position of the Fermi level, as was the case for PBE and its semi-metallic ground state.

To still investigate the HSE functionals ground state, the unit cell is reduced to the primitive 7-atom cell for NM calculations in **exciting**. A **k**-mesh of 6×6×6 was enough to converge the band structure and DoS qualitatively. As total energy is not a concern, $R_{\text{MT}}G_{\text{max}} = 7$ was enough to provide the electronic structure. Specific to hybrid functionals, the number of empty bands required convergence also for the NM phase. The value $n_{\text{empty}} = 600$ was shown to converge the HSE electronic structure qualitatively. Similarly to Co, the Wannier interpolation method is used to construct the band struc-

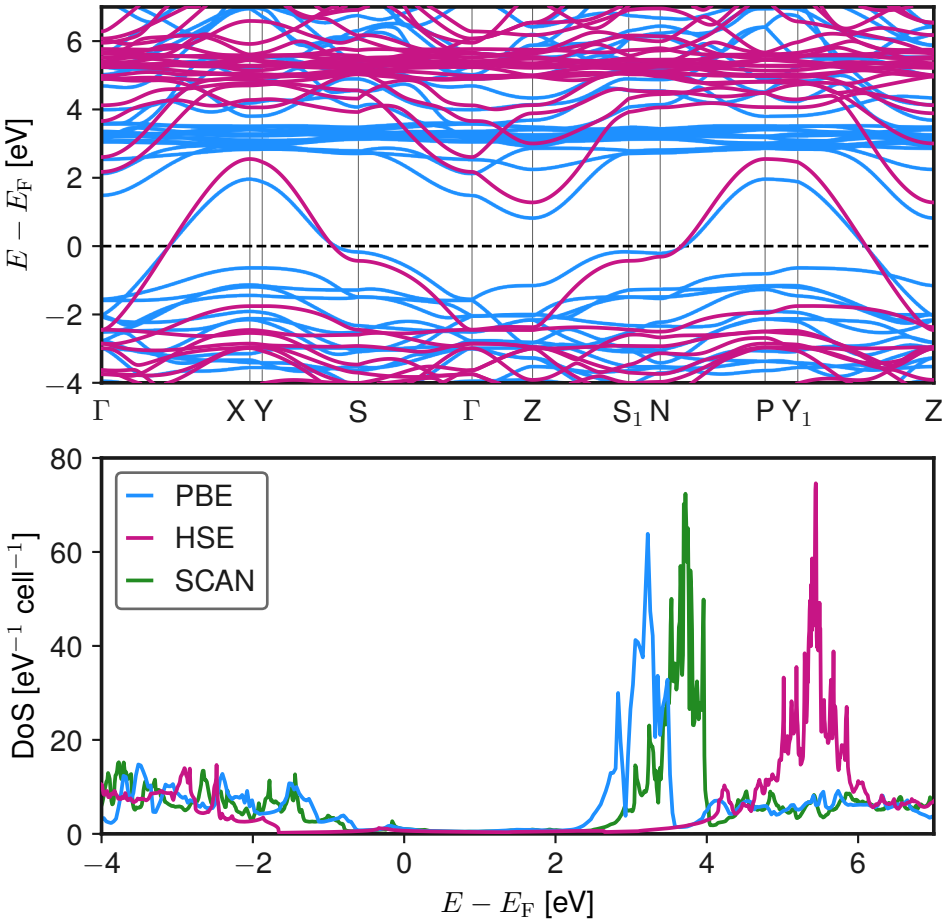

Figure 4.5: Upper panel:Band structure of NM LCO obtained wtih `exciting` using PBE and HSE. The dashed line marks the Fermi level. Lower panel: DoS of NM LCO calculated in `exciting` with PBE, HSE, and SCAN. The SCAN data was calculated in the 14 atom unit cell, the HSE and PBE data in the primitive 7 atom unit cell.

ture and DoS, shown in Figure 4.5. A striking feature in the spectrum is the isolation of the copper band crossing the Fermi level. The lanthanum states are pushed up by 2-3 eV in the HSE calculation compared to PBE, while the copper-oxygen valence edge is lowered by about 2 eV. The PBE calculation is performed at the same numeric parameters as the HSE one. As a further comparison, a SCAN DoS is included. SCAN was not able to be numerically converged the calculation at these parameters, the DoS included is calculated from the NM 14 atom unit cell. The DoS in fact underlines the pattern of this chapter: The higher up Jacob's ladder, the bigger the gap between the lanthanum bands and the leading copper-oxygen band edge.

The AFM phase at the HSE level was investigated within the **FHI-aims** code. There were no numerical adjustments, the same $10\times10\times10$ **k**-mesh as for the other functionals was used, with a 0.001 Ha Gaussian smearing width. The NM investigation suggested an even increased band gap as compared to the mGGA level, with potentially even larger magnetic moments. This can be confirmed, with the gap growing to 2.85 eV and with the magnetic moments amounting to $0.62\,\mu_\mathrm{B}$. HSE thus leads to an overestimated electronic band gap, while the magnetic moments are firmly in the experimental range.

This completes the investigation of the highest rung of Jacob's ladder included in this work. As a final summary, all values for the band gap and magnetic moments calculated in this work are part of a histogram in Figure 4.6, with literature **VASP** results [8, 89] being added for further reference. The HSE band gap is a clear outlier in the results. Hybrid functionals recreate the PBE ground state in the limit of the mixing parameter $\beta \to 0$. Given continuity, an appropriate mixing parameter exist, for which the band gap is in the experimental range. The magnetic moments were shown to behave less sensitive to the localization. Still, it is not clear whether a suitable β (and ω in the case of HSE) exists, for which both quantities agree with experiment.

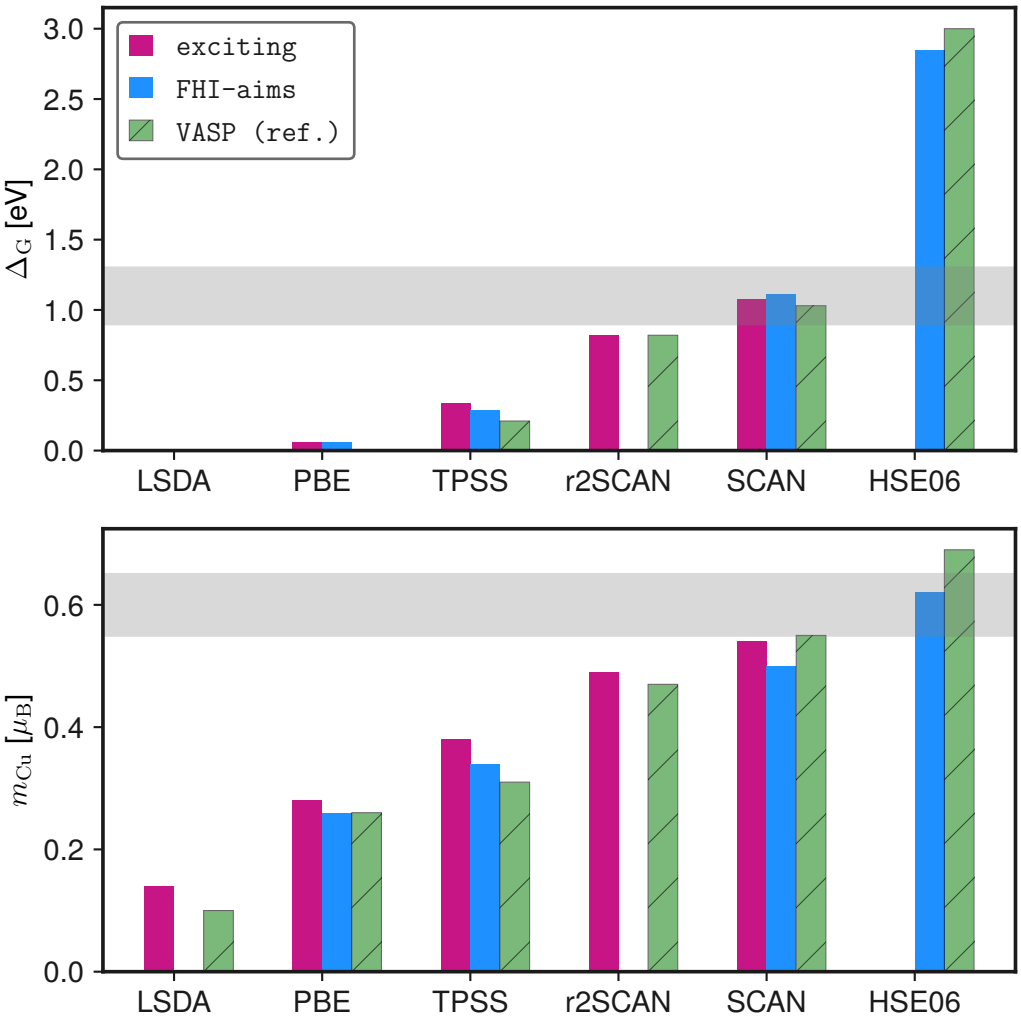

Figure 4.6: Summary of electronic band gap and copper magnetic moment for LCO for several functionals. Included are the results obtained using **`exciting`** (red) and **`FHI-aims`** (blue) calculations performed in the present work, as well as literature values (green) from Ref. [8] and Ref. [89] for **`VASP`**. The shaded region highlights the experimental values [91, 97].

Conclusions and Outlook

Through a detailed study of ground-state DFT calculations, this work painted a coherent picture of exchange-correlation functionals applied to two, starkly different, magnetic systems. The itinerant ferromagnet cobalt and the Mott-insulating antiferromagnet La_2CuO_4 served as subjects of investigation, with both materials characterized by very different magnetic interactions. In particular, the current study focused the dependence of magnetic properties on the approximations to the exchange-correlation energy functional, specifically with regard to the exchange-energy component. The implementation of mGGA functionals in `exciting` was successfully benchmarked via comparison to DFT results from the literature and to `FHI-aims` calculations performed within this work. Particularly for the complex 14 atom material La_2CuO_4, the results agreed well and the sensitive magnetic structure was reproduced.

The fcc unit cell of cobalt was optimized for PBE, SCAN, and TPSS, with good agreement between the two codes in the lattice constants. In `exciting`, PBE was found to produce a unit-cell magnetization of $1.65\,\mu_B$, TPSS and SCAN a magnetization of $1.67\,\mu_B$ and $1.80\,\mu_B$ respectively. The Stoner mechanism of ferromagnetism was highlighted, and through its lens the magnetic interaction in cobalt was analyzed. The exchange enhancement of the mGGA functionals, and the non-local exact exchange of hybrids, were identified as a key factor in excessively increasing exchange splitting in cobalt, thereby overestimating unit-cell magnetization. Future studies in this regard could expand on quantitative analysis through a fixed-spin-moment investigation of the energy dependence on the magnetization. This would then allow for the determination of the Stoner parameter as a measure of exchange-splitting [79]. Furthermore, the investigation of cobalt using HSE06 within `exciting` could be expanded to the ferromagnetic phase. Specifically the purely computational part, a new formulation is proposed for the implementation of collinear hybrid-functional calculations in an LAPW+lo basis set using a mixed-product basis in second variation. Work is in progress to include this formulation in the `exciting` code.

While mGGA and hybrid functionals were shown to overestimate magnetic effects in cobalt, their exchange components were determined to be essential in stabilizing the antiferromagnetic and insulating ground state of tetragonal La_2CuO_4. SCAN was found to agree well with experimental data, predicting a band gap of 1.08 eV and copper magnetic moments of $0.54\,\mu_B$. The isolated-orbital indication, as enabled by inclusion of the kinetic-energy density, was argued to be a vital part of the mGGA functional in the context of La_2CuO_4. The HSE06 functional was shown to overestimate the band gap in particular, with calculations using `FHI-aims` finding a value of 2.85 eV. Nonmagnetic calculations were performed in `exciting` and the resulting electronic structure was analyzed. The correct description of the ground state at near GGA cost using mGGA functionals allows for the expansion of the unit cell to the orthorhombic structure, the experimental geometry of La_2CuO_4. This lays the groundwork for the investigation of the doping-induced transition to a metallic, superconducting phase. Furthermore, the variable nature of the amount of exact exchange in a hybrid functional raises the question for an appropriate mixing and screening parameter for the HSE functional, similar to the question of an optimal isolated-orbital indicator α in mGGA functionals.

To conclude this thesis, a final metaphor is offered. The concept of Jacob's ladder was the guiding principle in the investigations of the two magnetic systems. The mGGA functionals may appear as basically superior to hybrids in this study: They yield less over-magnetization for cobalt, with experimental band gaps and copper moments for La_2CuO_4 at significantly lower computational cost than the over-insulating HSE06 functional. This conclusion requires a more detailed picture however: TPSS did not significantly improve upon the localization of PBE for La_2CuO_4, while TPSS was specifically the one mGGA functional that performed well for cobalt. On the other hand, it was SCAN with its sharp isolated-orbital detection that dealt well with the cuprate, while producing HSE-like results for the magnetization in the itinerant ferromagnet. This result is not unique to this investigation [13]. When (de-)localization plays a key role in the magnetic structure, mGGA functionals could greatly improve upon GGA ones — or they could do the opposite. They, it could be argued, also fit the image of a special-purpose tool, as did the LSDA-based methodologies of localization in La_2CuO_4. Hybrid functionals on the other hand offer the unique possibility of a fundamental advancement in exchange-correlation functionals, and along with that the free choice of their position along this presented "localization-tipping-scale", as in the limit the PBE ground state can always be recovered.

Appendix A

For the sake of completeness, figures and other materials not immediately necessary for the arguments of the main work are collected in this appendix. This material was mentioned in the main part, and thus the computational parameters used here are to be taken from the corresponding sections. Specifically, this appendix includes NM Co electronic band structures and DoS figures, NM LCO mGGA results, and the description of the fit functions used for the equations of state used in the optimization of the unit cells.

A.1 Additional figures

Collected in this section are figures containing the nonmagnetic electronic structure of Co and LCO. In the case of Co, the comparison between `FHI-aims` and `exciting` could be suitably made with only the FM data, and for LCO the effects of the mGGA functionals on the ground state were well visible in the AFM structure alone.

A.1.1 Nonmagnetic Cobalt: Electronic Structure

Specifically the nonmagentic results for cobalt were omitted from Chapter 2. The benchmark between `FHI-aims` and `exciting` of the NM phase (the FM counterpart in Section 2.2) can be seen in Figure A.7. Great overlap in the disperion relation can be seen for all functionals, notably also for SCAN, whereas the FM phase showed a minor discrepancy here. Figure A.8 shows the comparison of NM Co for different functionals in `exciting`. This is done analogously to the comparison of the FM phase in Section 2.3. The same pattern of a spread out $3d$-band, with a lowered $D(E_F)$ is observable in the SCAN data. Compared to the FM phase the impacts of the exchange-correlation functional are minor and therefore omitted from the main chapter.

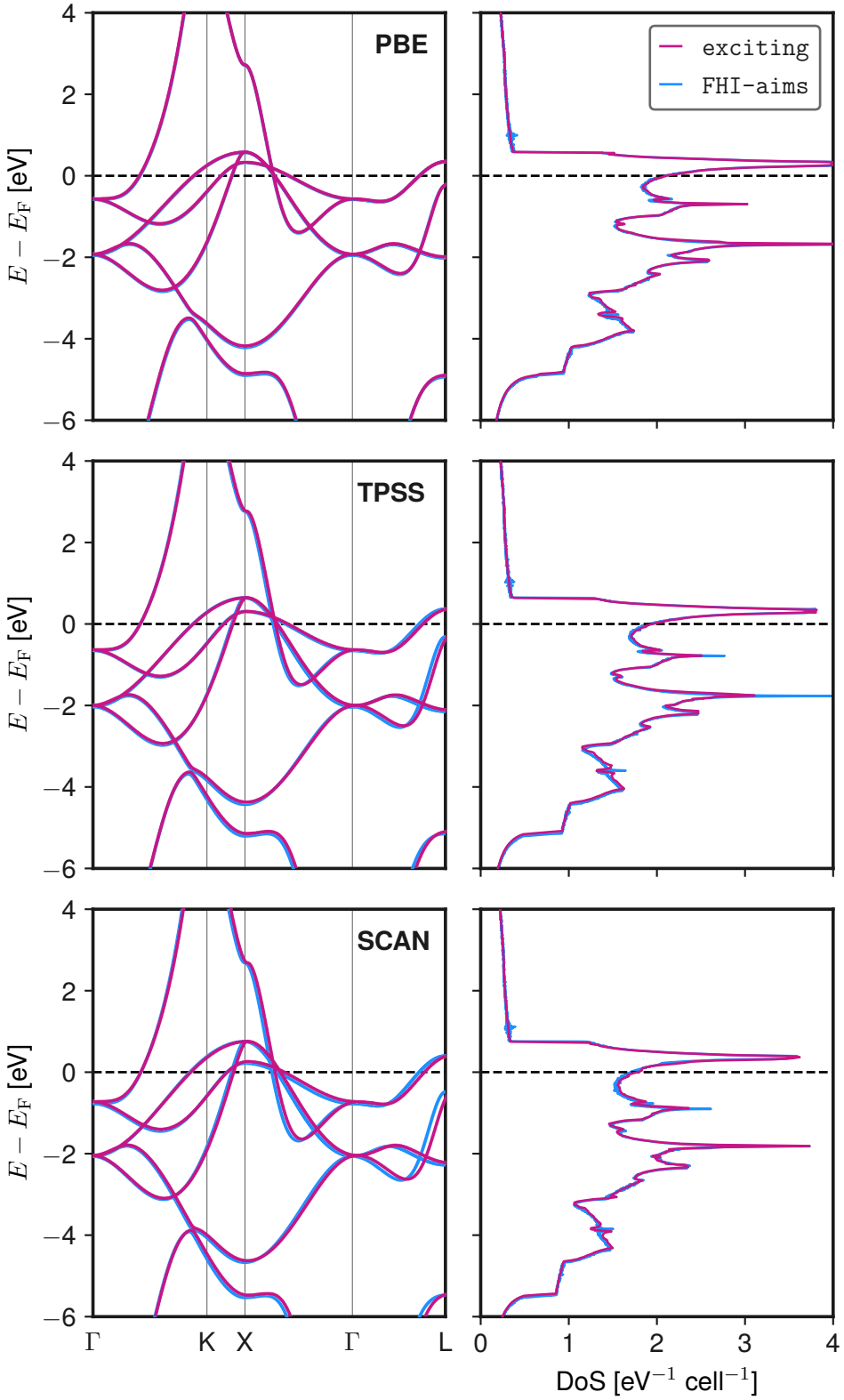

Figure A.7: Band structure (left panels) and DoS (right panels) of NM Co with the PBE, TPSS, and SCAN functional perfomed using both `exciting` and `FHI-aims`. Calculations are done at the respective equilibrium unit-cell volume. The dashed line marks the Fermi level.

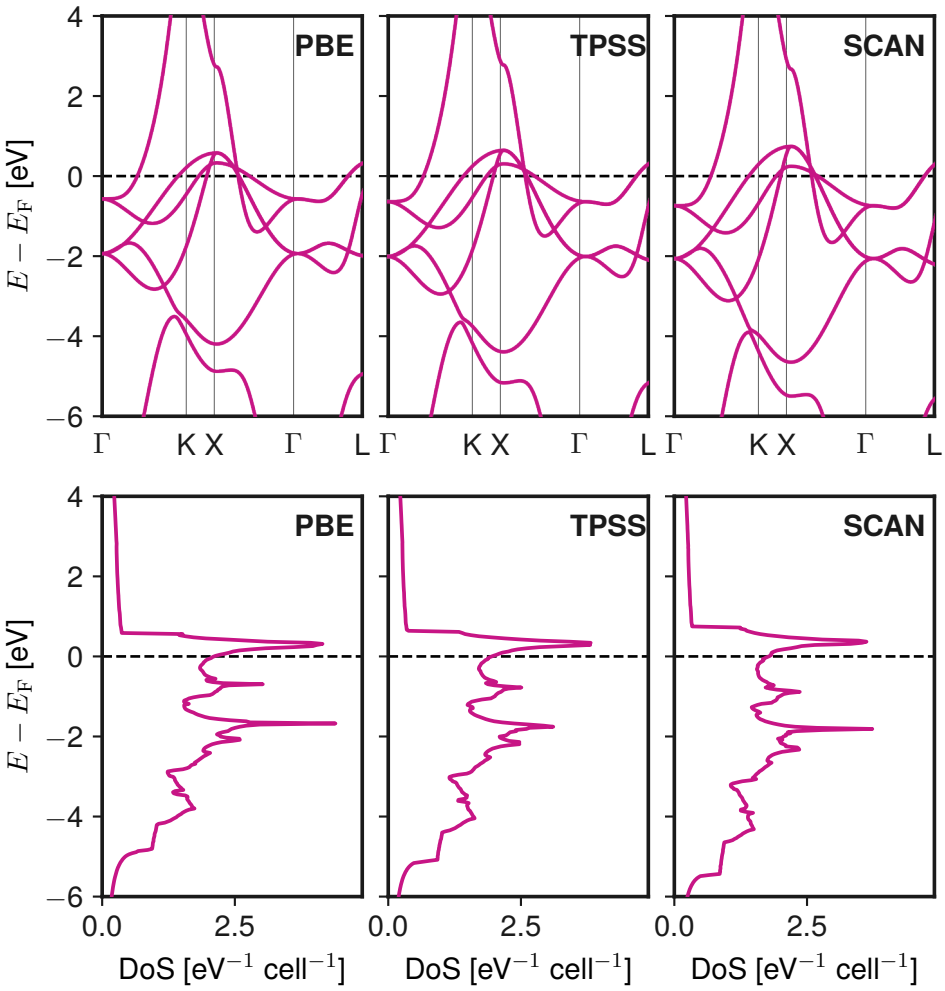

Figure A.8: Band structure (upper panels) and DoS (lower panels) of NM Co obtained using the `exciting` code with PBE, TPSS, and SCAN. Calculations are done at the respective equilibrium unit cell volume. The dashed line marks the Fermi level.

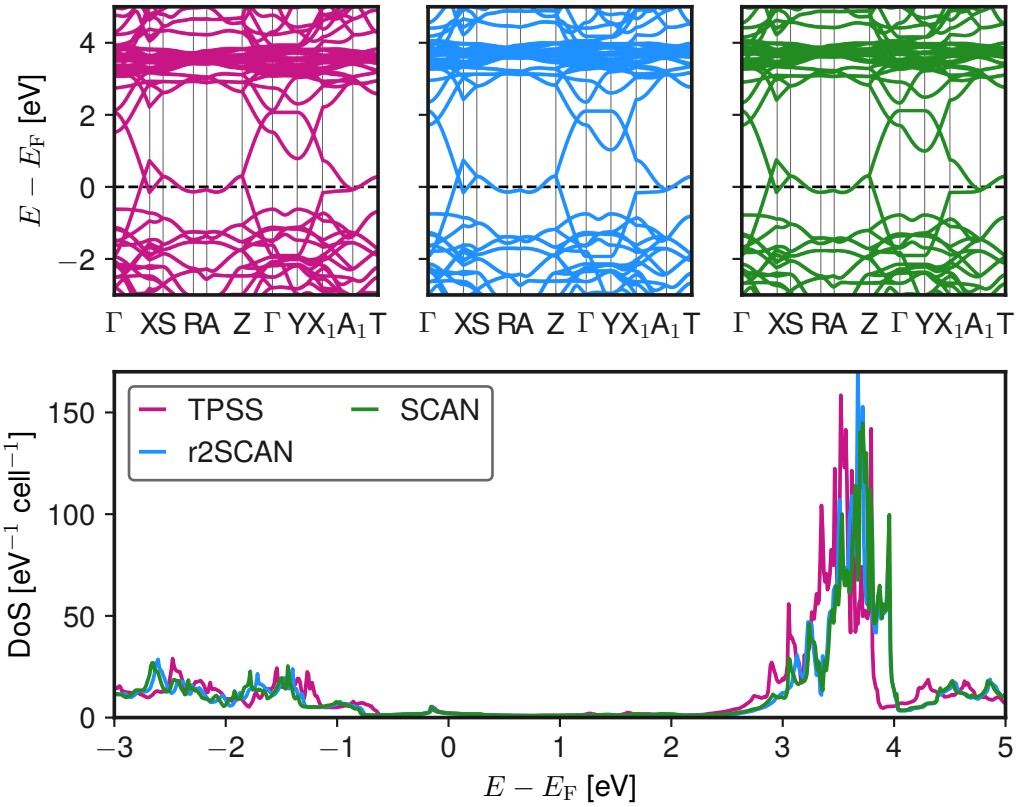

Figure A.9: Band structure (upper panels) and DoS (lower panel) of NM LCO with the TPSS, r2SCAN and SCAN functional obtained using `exciting`. The dashed line marks the Fermi level.

A.1.2 Nonmagnetic La_2CuO_4: mGGA Electronic Structure

In Figure A.9 the comparison of the electronic structure of NM LCO with the different mGGA functionals is shown. This corresponds to the NM version of Figure 4.3. The energy range was increased to highlighted differences in higher-energy states. The $3d$ copper band crossing the Fermi level agrees qualitatively. The lower, occupied bands are shifted up in the TPSS-obtained data compared to the SCAN functionals. In other words, the $3d$ band is more isolated for the SCAN functionals, as the La states at 3-4 eV are also lower for in energy for TPSS.

A.2 Fit functions

The equations of state in this work were fitted with the internal energy given by the third order Birch-Munarghan equation of state [75]. In the following equation, B_0 denotes the Bulk modulus of the unit cell and B_0' its derivative:

$$E(V) = E_0 + \frac{9\,V_0\,B_0}{16}\left\{\left[\left(\frac{V_0}{V}\right)^{\frac{2}{3}} - 1\right]^3 B_0' + \left[\left(\frac{V_0}{V}\right)^{\frac{2}{3}} - 1\right]^2 \left[6 - 4\left(\frac{V_0}{V}\right)^{\frac{2}{3}}\right]\right\}. \tag{A.2.1}$$

The dependence of the ratio c/a was determined through a fit with a fifth-order polynomial:

$$E\left(\frac{c}{a}\right) = \sum_{i=0}^{5} \gamma_i \left(\frac{c}{a}\right)^i. \tag{A.2.2}$$

A.2.1 Equation of state of Cobalt

The parameters of the Birch-Munarghan fit are collected in Table A.4. The bulk modulus has not been discussed in Chapter 2. The FM lowers B_0 for all three functionals, together with an increase in unit-cell volume.

Table A.4: Equilibrium unit-cell volume V_0, total energy per cellE_0, bulk modulus B_0, and its derivative B_0' of fcc Co using `exciting` and `FHI-aims` for PBE, TPSS, and SCAN, as obtained from the Birch-Munarghan fit of the EoS.

Functional	Code	Phase	V_0 [Å^3]	E_0 [eV]	B_0 [eV/Å^{-3}]	B_0'
PBE	`exciting`	NM	10.337	−37918.47	0.534	1.948
	`FHI-aims`	NM	10.295	−38073.66	0.537	1.882
	`exciting`	FM	10.966	−37918.66	0.436	2.473
	`FHI-aims`	FM	10.914	−38073.85	0.441	2.413
TPSS	`exciting`	NM	10.015	−37925.82	0.582	1.237
	`FHI-aims`	NM	9.958	−38080.68	0.599	1.642
	`exciting`	FM	10.615	−37926.01	0.473	3.157
	`FHI-aims`	FM	10.562	−38080.86	0.483	3.019
SCAN	`exciting`	NM	9.836	−37927.61	0.608	1.378
	`FHI-aims`	NM	9.788	−38082.16	0.624	1.546
	`exciting`	FM	10.836	−37928.13	0.435	2.077
	`FHI-aims`	FM	10.745	−38082.66	0.456	1.896

A.2.2 Geometry optimization of La_2CuO_4

As was discussed in Chapter 3, the two magnetic phases of LCO yield virtually identical geometries. The parameters of both of the Birch-Munarghan fits are summarized in Table A.5. The derivative of the bulk modulus shows a minor decrease in the AFM compared to NM, this is however the only substantial difference in parameters. The c/a ratio polynomial coefficients of Table A.6 mirror this behaviour. The higher-order parameters of the AFM phase are smaller in magnitude, indicating a flatter energy landscape.

Table A.5: Equilibrium unit-cell volume V_0, total energy per cell E_0, bulk modulus B_0, and its derivative B_0' of LCO using `exciting` with PBE, as obtained from the Birch-Munarghan fit of the EoS.

Phase	V_0 [Å^3]	E_0 [eV]	B_0 [eV/Å^{-3}]	B_0'
NM	192.701	−1 031 409.62	0.322	1.912
AFM	192.712	−1 031 409.68	0.324	1.558

Table A.6: Coefficients of the polynomial fit for the lattice-constant-ratio c/a of LCO with PBE using `exciting` given in eV.

Phase	γ_0	γ_1	γ_2	γ_3	γ_4	γ_5
NM	−1 033 202.07	3 878.74	−3 317.64	1 407.45	−297.06	25.02
AFM	−1 031 488.83	224.61	−206.46	85.89	−17.04	1.35

List of Figures

List of Tables

Bibliography

[1] J. G. Bednorz and K. A. Müller, "Possible high T_C superconductivity in the BaLaCuO system," *Zeitschrift für Physik B Condensed Matter*, vol. 64, no. 2, pp. 189–193, Jun 1986. [Online]. Available: https://doi.org/10.1007/BF01303701

[2] L. Gao, Y. Y. Xue, F. Chen, Q. Xiong, R. L. Meng, D. Ramirez, C. W. Chu, J. H. Eggert, and H. K. Mao, "Superconductivity up to 164 K in $HgBa_2Ca_{m-1}Cu_mO_{2m+2+\delta}$ (m=1, 2, and 3) under quasihydrostatic pressures," *Phys. Rev. B*, vol. 50, pp. 4260–4263, Aug 1994. [Online]. Available: https://link.aps.org/doi/10.1103/PhysRevB.50.4260

[3] J. Bardeen, L. N. Cooper, and J. R. Schrieffer, "Theory of superconductivity," *Phys. Rev.*, vol. 108, pp. 1175–1204, Dec 1957. [Online]. Available: https://link.aps.org/doi/10.1103/PhysRev.108.1175

[4] H. Okamoto, T. Miyagoe, K. Kobayashi, H. Uemura, H. Nishioka, H. Matsuzaki, A. Sawa, and Y. Tokura, "Photoinduced transition from mott insulator to metal in the undoped cuprates Nd_2CuO_4 and La_2CuO_4," *Phys. Rev. B*, vol. 83, p. 125102, Mar 2011. [Online]. Available: https://link.aps.org/doi/10.1103/PhysRevB.83.125102

[5] P. Hohenberg and W. Kohn, "Inhomogeneous electron gas," *Phys. Rev.*, vol. 136, pp. B864–B871, Nov 1964. [Online]. Available: https://link.aps.org/doi/10.1103/PhysRev.136.B864

[6] W. Kohn and L. J. Sham, "Self-consistent equations including exchange and correlation effects," *Phys. Rev.*, vol. 140, pp. A1133–A1138, Nov 1965. [Online]. Available: https://link.aps.org/doi/10.1103/PhysRev.140.A1133

[7] C. Ambrosch-Draxl and K. Schwarz, "Local-spin-density calculations of antiferromagnetic $YBa_2Cu_3O_6$ and La_2CuO_4," *Solid State Commu-*

nications, vol. 77, no. 1, pp. 45–48, 1991. [Online]. Available: https://www.sciencedirect.com/science/article/pii/003810989190423S

[8] K. Pokharel, C. Lane, J. W. Furness, R. Zhang, J. Ning, B. Barbiellini, R. S. Markiewicz, Y. Zhang, A. Bansil, and J. Sun, "Sensitivity of the electronic and magnetic structures of cuprate superconductors to density functional approximations," *npj Computational Materials*, vol. 8, no. 1, p. 31, Feb 2022. [Online]. Available: https://doi.org/10.1038/s41524-022-00711-z

[9] D. J. Singh and W. E. Pickett, "Gradient-corrected density-functional studies of $CaCuO_2$," *Phys. Rev. B*, vol. 44, pp. 7715–7717, Oct 1991. [Online]. Available: https://link.aps.org/doi/10.1103/PhysRevB.44.7715

[10] A. Gulans, S. Kontur, C. Meisenbichler, D. Nabok, P. Pavone, S. Rigamonti, S. Sagmeister, U. Werner, and C. Draxl, "`exciting`: a full-potential all-electron package implementing density-functional theory and many-body perturbation theory," *Journal of Physics: Condensed Matter*, vol. 26, no. 36, p. 363202, aug 2014. [Online]. Available: https://dx.doi.org/10.1088/0953-8984/26/36/363202

[11] E. M. Stephan, "Implementation of meta-GGA functionals in the all-electron linearized augmented plane wave code `exciting`," Master's thesis, Humboldt-Universität zu Berlin, Institut für Physik, Berlin, Germany, October 2024, supervisors: Prof. Dr. Claudia Draxl and PD Dr. Denis Usvyat.

[12] Y.-R. Jang and B. Deok Yu, "Hybrid functional study of the structural and electronic properties of Co and Ni," *Journal of the Physical Society of Japan*, vol. 81, no. 11, p. 114715, 2012. [Online]. Available: https://doi.org/10.1143/JPSJ.81.114715

[13] F. Tran, G. Baudesson, J. Carrete, G. K. H. Madsen, P. Blaha, K. Schwarz, and D. J. Singh, "Shortcomings of meta-GGA functionals when describing magnetism," *Phys. Rev. B*, vol. 102, p. 024407, Jul 2020. [Online]. Available: https://link.aps.org/doi/10.1103/PhysRevB.102.024407

[14] J. Kübler, *Theory of Itinerant Electron Magnetism*. Oxford: Oxford University Press, 2000.

[15] J. P. Perdew and K. Schmidt, "Jacob's ladder of density functional approximations for the exchange-correlation energy," *AIP Conference Proceedings*, vol. 577, no. 1, pp. 1–20, 07 2001. [Online]. Available: https://doi.org/10.1063/1.1390175

[16] W. Kohn, "Nobel lecture: Electronic structure of matter—wave functions and density functionals," *Rev. Mod. Phys.*, vol. 71, pp. 1253–1266, Oct 1999. [Online]. Available: https://link.aps.org/doi/10.1103/RevModPhys.71.1253

[17] M. Born and R. Oppenheimer, "Zur Quantentheorie der Molekeln," *Annalen der Physik*, vol. 389, no. 20, pp. 457–484, 1927. [Online]. Available: https://onlinelibrary.wiley.com/doi/abs/10.1002/andp.19273892002

[18] L. N. David J. Singh, *Planewaves, Pseudopotentials, and the LAPW Method*. Springer New York, NY, 11 2005. [Online]. Available: https://doi.org/10.1007/978-0-387-29684-5

[19] F. Bloch, "Über die Quantenmechanik der Elektronen in Kristallgittern," *Zeitschrift für Physik*, vol. 52, no. 7, pp. 555–600, Jul 1929. [Online]. Available: https://doi.org/10.1007/BF01339455

[20] O. K. Andersen, "Linear methods in band theory," *Phys. Rev. B*, vol. 12, pp. 3060–3083, Oct 1975. [Online]. Available: https://link.aps.org/doi/10.1103/PhysRevB.12.3060

[21] G. K. H. Madsen, P. Blaha, K. Schwarz, E. Sjöstedt, and L. Nordström, "Efficient linearization of the augmented plane-wave method," *Phys. Rev. B*, vol. 64, p. 195134, Oct 2001. [Online]. Available: https://link.aps.org/doi/10.1103/PhysRevB.64.195134

[22] E. Sjöstedt, L. Nordström, and D. Singh, "An alternative way of linearizing the augmented plane-wave method," *Solid State Communications*, vol. 114, no. 1, pp. 15–20, 2000. [Online]. Available: https://www.sciencedirect.com/science/article/pii/S0038109899005773

[23] A. Gulans, A. Kozhevnikov, and C. Draxl, "Microhartree precision in density functional theory calculations," *Phys. Rev. B*, vol. 97, p. 161105, Apr 2018. [Online]. Available: https://link.aps.org/doi/10.1103/PhysRevB.97.161105

[24] V. Blum, R. Gehrke, F. Hanke, P. Havu, V. Havu, X. Ren, K. Reuter, and M. Scheffler, "Ab initio molecular simulations with numeric atom-centered orbitals," *Computer Physics Communications*, vol. 180, no. 11, pp. 2175–2196, 2009. [Online]. Available: https://www.sciencedirect.com/science/article/pii/S0010465509002033

[25] K. Lejaeghere, G. Bihlmayer, T. Björkman, P. Blaha, S. Blügel, V. Blum, D. Caliste, I. E. Castelli, S. J. Clark, A. D. Corso, S. de Gironcoli, T. Deutsch, J. K. Dewhurst, I. D. Marco, C. Draxl, M. Dułak, O. Eriksson, J. A. Flores-Livas, K. F. Garrity, L. Genovese, P. Giannozzi, M. Giantomassi, S. Goedecker, X. Gonze, O. Grånäs, E. K. U. Gross, A. Gulans, F. Gygi, D. R. Hamann, P. J. Hasnip, N. A. W. Holzwarth, D. Iuşan, D. B. Jochym, F. Jollet, D. Jones, G. Kresse, K. Koepernik, E. Küçükbenli, Y. O. Kvashnin, I. L. M. Locht, S. Lubeck, M. Marsman, N. Marzari, U. Nitzsche, L. Nordström, T. Ozaki, L. Paulatto, C. J. Pickard, W. Poelmans, M. I. J. Probert, K. Refson, M. Richter, G.-M. Rignanese, S. Saha, M. Scheffler, M. Schlipf, K. Schwarz, S. Sharma, F. Tavazza, P. Thunström, A. Tkatchenko, M. Torrent, D. Vanderbilt, M. J. van Setten, V. V. Speybroeck, J. M. Wills, J. R. Yates, G.-X. Zhang, and S. Cottenier, "Reproducibility in density functional theory calculations of solids," *Science*, vol. 351, no. 6280, p. aad3000, 2016. [Online]. Available: https://www.science.org/doi/abs/10.1126/science.aad3000

[26] S. R. Jensen, S. Saha, J. A. Flores-Livas, W. Huhn, V. Blum, S. Goedecker, and L. Frediani, "The elephant in the room of density functional theory calculations," *The Journal of Physical Chemistry Letters*, vol. 8, no. 7, pp. 1449–1457, Apr 2017. [Online]. Available: https://doi.org/10.1021/acs.jpclett.7b00255

[27] W. P. Huhn and V. Blum, "One-hundred-three compound band-structure benchmark of post-self-consistent spin-orbit coupling treatments in density functional theory," *Phys. Rev. Mater.*, vol. 1, p. 033803, Aug 2017. [Online]. Available: https://link.aps.org/doi/10.1103/PhysRevMaterials.1.033803

[28] A. Gulans and C. Draxl, "Influence of spin-orbit coupling on chemical bonding," 2022. [Online]. Available: https://arxiv.org/abs/2204.02751

[29] L. Lin, S. Shao, and W. E, "Efficient iterative method for solving the Dirac–Kohn–Sham density functional theory," *Journal of Computational*

Physics, vol. 245, p. 205–217, Jul. 2013. [Online]. Available: http://dx.doi.org/10.1016/j.jcp.2013.03.030

[30] E. v. Lenthe, E. J. Baerends, and J. G. Snijders, "Relativistic regular two-component Hamiltonians," *The Journal of Chemical Physics*, vol. 99, no. 6, pp. 4597–4610, 09 1993. [Online]. Available: https://doi.org/10.1063/1.466059

[31] E. van Lenthe, E. J. Baerends, and J. G. Snijders, "Relativistic total energy using regular approximations," *The Journal of Chemical Physics*, vol. 101, no. 11, pp. 9783–9792, 12 1994. [Online]. Available: https://doi.org/10.1063/1.467943

[32] E. Engel and R. M. Dreizler, *Foundations of Density Functional Theory: Existence Theorems*. Berlin, Heidelberg: Springer Berlin Heidelberg, 2011, pp. 11–56. [Online]. Available: https://doi.org/10.1007/978-3-642-14090-7_2

[33] S. Sousa, P. Fernandes, and M. Ramos, "General performance of density functionals," *The journal of physical chemistry. A*, vol. 111, pp. 10 439–52, 11 2007.

[34] F. Tran, J. Stelzl, and P. Blaha, "Rungs 1 to 4 of DFT Jacob's ladder: Extensive test on the lattice constant, bulk modulus, and cohesive energy of solids," *The Journal of Chemical Physics*, vol. 144, no. 20, May 2016. [Online]. Available: http://dx.doi.org/10.1063/1.4948636

[35] D. Fritsch and S. Schorr, "Climbing jacob's ladder: A density functional theory case study for $Ag_2ZnSnSe_4$ and $Cu_2ZnSnSe_4$," *Journal of Physics: Energy*, vol. 3, no. 1, p. 015002, November 2020. [Online]. Available: https://dx.doi.org/10.1088/2515-7655/abc07b

[36] I. Y. Zhang and X. Xu, "On the top rung of Jacob's ladder of density functional theory: Toward resolving the dilemma of sie and nce," *WIREs Computational Molecular Science*, vol. 11, no. 1, p. e1490, 2021. [Online]. Available: https://wires.onlinelibrary.wiley.com/doi/abs/10.1002/wcms.1490

[37] N. Mardirossian and M. Head-Gordon, "Thirty years of density functional theory in computational chemistry: an overview and extensive assessment of 200 density functionals," *Molecular Physics*,

vol. 115, no. 19, pp. 2315–2372, 2017. [Online]. Available: https://doi.org/10.1080/00268976.2017.1333644

[38] S. H. Vosko, L. Wilk, and M. Nusair, "Accurate spin-dependent electron liquid correlation energies for local spin density calculations: a critical analysis," *Canadian Journal of Physics*, vol. 58, no. 8, pp. 1200–1211, 1980. [Online]. Available: https://doi.org/10.1139/p80-159

[39] D. M. Ceperley and B. J. Alder, "Ground state of the electron gas by a stochastic method," *Phys. Rev. Lett.*, vol. 45, pp. 566–569, Aug 1980. [Online]. Available: https://link.aps.org/doi/10.1103/PhysRevLett.45.566

[40] J. P. Perdew and A. Zunger, "Self-interaction correction to density-functional approximations for many-electron systems," *Phys. Rev. B*, vol. 23, pp. 5048–5079, May 1981. [Online]. Available: https://link.aps.org/doi/10.1103/PhysRevB.23.5048

[41] G. Ortiz and P. Ballone, "Correlation energy, structure factor, radial distribution function, and momentum distribution of the spin-polarized uniform electron gas," *Phys. Rev. B*, vol. 50, pp. 1391–1405, Jul 1994. [Online]. Available: https://link.aps.org/doi/10.1103/PhysRevB.50.1391

[42] D. M. Ceperley and B. J. Alder, "Ground state of the electron gas by a stochastic method," *Phys. Rev. Lett.*, vol. 45, pp. 566–569, Aug 1980. [Online]. Available: https://link.aps.org/doi/10.1103/PhysRevLett.45.566

[43] J. P. Perdew and Y. Wang, "Accurate and simple analytic representation of the electron-gas correlation energy," *Phys. Rev. B*, vol. 45, pp. 13 244–13 249, Jun 1992. [Online]. Available: https://link.aps.org/doi/10.1103/PhysRevB.45.13244

[44] J. Grotendorst, S. Blügel, and D. Marx, Eds., *Computational Nanoscience: Do It Yourself! ; NIC Winter School, 14 - 22 February 2006, Forschungszentrum Jülich, Germany - Lecture Notes*, ser. NIC series. Jülich: FZJ, John von Neumann Institute for Computing, 2006, vol. 31, record converted from VDB: 12.11.2012. [Online]. Available: https://juser.fz-juelich.de/record/51139

[45] R. O. Jones and O. Gunnarsson, "The density functional formalism, its applications and prospects," *Rev. Mod. Phys.*, vol. 61, pp. 689–746, Jul 1989. [Online]. Available: https://link.aps.org/doi/10.1103/RevModPhys.61.689

[46] M. Ernzerhof and G. E. Scuseria, "Assessment of the Perdew–Burke–Ernzerhof exchange-correlation functional," *The Journal of Chemical Physics*, vol. 110, no. 11, pp. 5029–5036, 03 1999. [Online]. Available: https://doi.org/10.1063/1.478401

[47] I. Yakovkin and P. Dowben, "The problem of the band gap in lda calculations," *Surface Review and Letters (SRL)*, vol. 14, pp. 481–487, 06 2007.

[48] J. P. Perdew, K. Burke, and M. Ernzerhof, "Generalized gradient approximation made simple," *Phys. Rev. Lett.*, vol. 77, pp. 3865–3868, Oct 1996. [Online]. Available: https://link.aps.org/doi/10.1103/PhysRevLett.77.3865

[49] B. Barbiellini, E. G. Moroni, and T. Jarlborg, "Effects of gradient corrections on electronic structure in metals," *Journal of Physics: Condensed Matter*, vol. 2, no. 37, p. 7597, sep 1990. [Online]. Available: https://dx.doi.org/10.1088/0953-8984/2/37/005

[50] D. J. Singh, W. E. Pickett, and H. Krakauer, "Gradient-corrected density functionals: Full-potential calculations for iron," *Phys. Rev. B*, vol. 43, pp. 11 628–11 634, May 1991. [Online]. Available: https://link.aps.org/doi/10.1103/PhysRevB.43.11628

[51] J.-W. Song, G. Giorgi, K. Yamashita, and K. Hirao, "Communication: Singularity-free hybrid functional with a gaussian-attenuating exact exchange in a plane-wave basis," *J Chem Phys*, vol. 138, no. 24, p. 241101, Jun. 2013.

[52] B.-L. Liu, Y.-C. Wang, Y. Liu, H.-F. Liu, and H.-F. Song, "Doubly screened coulomb correction approach for strongly correlated systems," *The Journal of Physical Chemistry Letters*, vol. 14, no. 40, pp. 8930–8939, Oct 2023. [Online]. Available: https://doi.org/10.1021/acs.jpclett.3c02035

[53] J. Kubler, K. H. Hock, J. Sticht, and A. R. Williams, "Density functional theory of non-collinear magnetism," *Journal of Physics F:*

Metal Physics, vol. 18, no. 3, p. 469, mar 1988. [Online]. Available: https://dx.doi.org/10.1088/0305-4608/18/3/018

[54] Z. Pu, N. Zhang, H. Jiang, and Y. Xiao, "Approach for noncollinear gga kernels in closed-shell systems," *Phys. Rev. B*, vol. 105, p. 035114, Jan 2022. [Online]. Available: https://link.aps.org/doi/10.1103/PhysRevB.105.035114

[55] J. P. Perdew and L. A. Constantin, "Laplacian-level density functionals for the kinetic energy density and exchange-correlation energy," *Phys. Rev. B*, vol. 75, p. 155109, Apr 2007. [Online]. Available: https://link.aps.org/doi/10.1103/PhysRevB.75.155109

[56] J. Doumont, F. Tran, and P. Blaha, "Implementation of self-consistent mgga functionals in augmented plane wave based methods," *Phys. Rev. B*, vol. 105, p. 195138, May 2022. [Online]. Available: https://link.aps.org/doi/10.1103/PhysRevB.105.195138

[57] J. Tao, J. P. Perdew, V. N. Staroverov, and G. E. Scuseria, "Climbing the density functional ladder: Nonempirical meta–generalized gradient approximation designed for molecules and solids," *Phys. Rev. Lett.*, vol. 91, p. 146401, Sep 2003. [Online]. Available: https://link.aps.org/doi/10.1103/PhysRevLett.91.146401

[58] J. Sun, J. P. Perdew, and A. Ruzsinszky, "Semilocal density functional obeying a strongly tightened bound for exchange," *Proceedings of the National Academy of Sciences*, vol. 112, no. 3, pp. 685–689, 2015. [Online]. Available: https://www.pnas.org/doi/abs/10.1073/pnas.1423145112

[59] J. Sun, A. Ruzsinszky, and J. P. Perdew, "Strongly constrained and appropriately normed semilocal density functional," *Phys. Rev. Lett.*, vol. 115, p. 036402, Jul 2015. [Online]. Available: https://link.aps.org/doi/10.1103/PhysRevLett.115.036402

[60] D. Mejia-Rodriguez and S. B. Trickey, "Deorbitalization strategies for meta-generalized-gradient-approximation exchange-correlation functionals," *Phys. Rev. A*, vol. 96, p. 052512, Nov 2017. [Online]. Available: https://link.aps.org/doi/10.1103/PhysRevA.96.052512

[61] A. P. Bartók and J. R. Yates, "Regularized scan functional," *The Journal of Chemical Physics*, vol. 150, no. 16, Apr. 2019. [Online]. Available: http://dx.doi.org/10.1063/1.5094646

[62] J. W. Furness, A. D. Kaplan, J. Ning, J. P. Perdew, and J. Sun, "Accurate and numerically efficient r2scan meta-generalized gradient approximation," *The Journal of Physical Chemistry Letters*, vol. 11, no. 19, pp. 8208–8215, 2020, pMID: 32876454. [Online]. Available: https://doi.org/10.1021/acs.jpclett.0c02405

[63] J. P. Perdew, M. Ernzerhof, and K. Burke, "Rationale for mixing exact exchange with density functional approximations," *The Journal of Chemical Physics*, vol. 105, no. 22, pp. 9982–9985, 12 1996. [Online]. Available: https://doi.org/10.1063/1.472933

[64] M. Betzinger, C. Friedrich, and S. Blügel, "Hybrid functionals within the all-electron flapw method: Implementation and applications of pbe0," *Phys. Rev. B*, vol. 81, p. 195117, May 2010. [Online]. Available: https://link.aps.org/doi/10.1103/PhysRevB.81.195117

[65] J. Heyd, G. E. Scuseria, and M. Ernzerhof, "Hybrid functionals based on a screened Coulomb potential," *The Journal of Chemical Physics*, vol. 118, no. 18, pp. 8207–8215, 05 2003. [Online]. Available: https://doi.org/10.1063/1.1564060

[66] M. Schlipf, M. Betzinger, C. Friedrich, M. Levzai'c, and S. Blugel, "Hse hybrid functional within the flapw method and its application to gdn," *Physical Review B*, vol. 84, 2011. [Online]. Available: https://api.semanticscholar.org/CorpusID:53561469

[67] C. Vona, "Electronic excitations in hybrid perovskites," Dissertation (Dr. rer. nat.), Humboldt-Universität zu Berlin, Mathematisch-Naturwissenschaftliche Fakultät, Berlin, Germany, 2024, specialization: Theoretical Physics.

[68] H. Jiang, R. I. Gómez-Abal, X.-Z. Li, C. Meisenbichler, C. Ambrosch-Draxl, and M. Scheffler, "Fhi-gap: A gw code based on the all-electron augmented plane wave method," *Computer Physics Communications*, vol. 184, no. 2, pp. 348–366, 2013. [Online]. Available: https://www.sciencedirect.com/science/article/pii/S0010465512003049

[69] Z.-P. Shi, J. F. Cooke, Z. Zhang, and B. M. Klein, "Structural, magnetic, and electronic properties of fe/au monatomic multilayers," *Phys. Rev. B*, vol. 54, pp. 3030–3032, Aug 1996. [Online]. Available: https://link.aps.org/doi/10.1103/PhysRevB.54.3030

[70] K. Lejaeghere, G. Bihlmayer, T. Björkman, P. Blaha, S. Blügel, V. Blum, D. Caliste, I. E. Castelli, S. J. Clark, A. D. Corso, S. de Gironcoli, T. Deutsch, J. K. Dewhurst, I. D. Marco, C. Draxl, M. Dułak, O. Eriksson, J. A. Flores-Livas, K. F. Garrity, L. Genovese, P. Giannozzi, M. Giantomassi, S. Goedecker, X. Gonze, O. Grånäs, E. K. U. Gross, A. Gulans, F. Gygi, D. R. Hamann, P. J. Hasnip, N. A. W. Holzwarth, D. Iuşan, D. B. Jochym, F. Jollet, D. Jones, G. Kresse, K. Koepernik, E. Küçükbenli, Y. O. Kvashnin, I. L. M. Locht, S. Lubeck, M. Marsman, N. Marzari, U. Nitzsche, L. Nordström, T. Ozaki, L. Paulatto, C. J. Pickard, W. Poelmans, M. I. J. Probert, K. Refson, M. Richter, G.-M. Rignanese, S. Saha, M. Scheffler, M. Schlipf, K. Schwarz, S. Sharma, F. Tavazza, P. Thunström, A. Tkatchenko, M. Torrent, D. Vanderbilt, M. J. van Setten, V. V. Speybroeck, J. M. Wills, J. R. Yates, G.-X. Zhang, and S. Cottenier, "Reproducibility in density functional theory calculations of solids," *Science*, vol. 351, no. 6280, p. aad3000, 2016. [Online]. Available: https://www.science.org/doi/abs/10.1126/science.aad3000

[71] R. Sewak, C. C. Dey, and D. Toprek, "Temperature induced phase transformation in co," *Scientific Reports*, vol. 12, no. 1, p. 10054, 2022. [Online]. Available: https://doi.org/10.1038/s41598-022-14302-x

[72] C. L. Fu and K. M. Ho, "First-principles calculation of the equilibrium ground-state properties of transition metals: Applications to nb and mo," *Phys. Rev. B*, vol. 28, pp. 5480–5486, Nov 1983. [Online]. Available: https://link.aps.org/doi/10.1103/PhysRevB.28.5480

[73] P. E. Blöchl, O. Jepsen, and O. K. Andersen, "Improved tetrahedron method for brillouin-zone integrations," *Phys. Rev. B*, vol. 49, pp. 16 223–16 233, Jun 1994. [Online]. Available: https://link.aps.org/doi/10.1103/PhysRevB.49.16223

[74] C. Draxl and M. Scheffler, "The nomad laboratory: from data sharing to artificial intelligence," *Journal of Physics: Materials*, vol. 2, no. 3, p. 036001, may 2019. [Online]. Available: https://dx.doi.org/10.1088/2515-7639/ab13bb

[75] F. Birch, "Finite elastic strain of cubic crystals," *Phys. Rev.*, vol. 71, pp. 809–824, Jun 1947. [Online]. Available: https://link.aps.org/doi/10.1103/PhysRev.71.809

[76] S. Tillack, A. Gulans, and C. Draxl, "Maximally localized wannier functions within the (L)APW + LO method," *Phys. Rev. B*, vol. 101, p. 235102, Jun 2020. [Online]. Available: https://link.aps.org/doi/10.1103/PhysRevB.101.235102

[77] M. Shimizu, "Ferromagnetism in iron, cobalt, nickel and their alloys," *Physica B+C*, vol. 91, pp. 14–23, 1977. [Online]. Available: https://www.sciencedirect.com/science/article/pii/0378436377901620

[78] E. C. Stoner, "Collective electron ferromagnetism," *Proceedings of the Royal Society of London. Series A. Mathematical and Physical Sciences*, vol. 165, no. 922, pp. 372–414, 1938. [Online]. Available: https://royalsocietypublishing.org/doi/abs/10.1098/rspa.1938.0066

[79] S. L. Dudarev and P. M. Derlet, "Interatomic potentials for materials with interacting electrons," *Journal of Computer-Aided Materials Design*, vol. 14, no. 1, pp. 129–140, 2007. [Online]. Available: https://doi.org/10.1007/s10820-007-9073-x

[80] H. P. Myers and W. Sucksmith, "The spontaneous magnetization of cobalt," *Proceedings of the Royal Society of London. Series A. Mathematical and Physical Sciences*, vol. 207, no. 1091, pp. 427–446, 1951. [Online]. Available: https://royalsocietypublishing.org/doi/abs/10.1098/rspa.1951.0132

[81] *Cuprate Superconductors: An Overview*. John Wiley & Sons, Ltd, 2015, ch. 5, pp. 87–100. [Online]. Available: https://onlinelibrary.wiley.com/doi/abs/10.1002/9781118696644.ch5

[82] W. Setyawan and S. Curtarolo, "High-throughput electronic band structure calculations: Challenges and tools," *Computational Materials Science*, vol. 49, no. 2, pp. 299–312, 2010. [Online]. Available: https://www.sciencedirect.com/science/article/pii/S0927025610002697

[83] R. Hord, G. Cordier, K. Hofmann, A. Buckow, G. Pascua, H. Luetkens, L. Alff, and B. Albert, "Transitions between lanthanum cuprates: Crystal structures of t′, orthorhombic, and k2nif4-type la2cuo4," *Zeitschrift für anorganische und allgemeine Chemie*, vol. 637, no. 9, pp. 1114–1117, 2011. [Online]. Available: https://onlinelibrary.wiley.com/doi/abs/10.1002/zaac.201100176

[84] J. Longo and P. Raccah, "The structure of la2cuo4 and lasrvo4," *Journal of Solid State Chemistry*, vol. 6, no. 4, pp. 526–531, 1973. [Online]. Available: https://www.sciencedirect.com/science/article/pii/S0022459673800106

[85] M. I. Houchati, M. Ceretti, C. Ritter, and W. Paulus, "From t to t′-la2cuo4 via oxygen vacancy ordered la2cuo3.5," *Chemistry of Materials*, vol. 24, no. 19, pp. 3811–3815, 2012. [Online]. Available: https://doi.org/10.1021/cm302485q

[86] H. Das and T. Saha-Dasgupta, "Electronic structure of la_2cuo_4 in the t and $T^{'}$ crystal structures using dynamical mean field theory," *Phys. Rev. B*, vol. 79, p. 134522, Apr 2009. [Online]. Available: https://link.aps.org/doi/10.1103/PhysRevB.79.134522

[87] Y. Imai, M. Kato, Y. Takarabe, T. Noji, and Y. Koike, "Low-temperature synthesis of la2cuo4 with the t′-structure from molten hydroxides," *Chemistry of Materials*, vol. 19, no. 15, pp. 3584–3585, 2007. [Online]. Available: https://doi.org/10.1021/cm070203n

[88] C. Lane, J. W. Furness, I. G. Buda, Y. Zhang, R. S. Markiewicz, B. Barbiellini, J. Sun, and A. Bansil, "Antiferromagnetic ground state of la_2cuo_4: A parameter-free ab initio description," *Phys. Rev. B*, vol. 98, p. 125140, Sep 2018. [Online]. Available: https://link.aps.org/doi/10.1103/PhysRevB.98.125140

[89] J. W. Furness, Y. Zhang, C. Lane, I. G. Buda, B. Barbiellini, R. S. Markiewicz, A. Bansil, and J. Sun, "An accurate first-principles treatment of doping-dependent electronic structure of high-temperature cuprate superconductors," *Communications Physics*, vol. 1, no. 1, p. 11, 2018. [Online]. Available: https://doi.org/10.1038/s42005-018-0009-4

[90] C. Varma, S. Schmitt-Rink, and E. Abrahams, "Charge transfer excitations and superconductivity in "ionic" metals," *Solid State Communications*, vol. 62, no. 10, pp. 681–685, 1987. [Online]. Available: https://www.sciencedirect.com/science/article/pii/0038109887904078

[91] J. M. Tranquada, *Neutron Scattering Studies of Antiferromagnetic Correlations in Cuprates*. New York, NY: Springer New York, 2007, pp. 257–298. [Online]. Available: https://doi.org/10.1007/978-0-387-68734-6_6

[92] B. Keimer, A. Aharony, A. Auerbach, R. J. Birgeneau, A. Cassanho, Y. Endoh, R. W. Erwin, M. A. Kastner, and G. Shirane, "Néel transition and sublattice magnetization of pure and doped la_2cuo_4," *Phys. Rev. B*, vol. 45, pp. 7430–7435, Apr 1992. [Online]. Available: https://link.aps.org/doi/10.1103/PhysRevB.45.7430

[93] K. Yamada, E. Kudo, Y. Endoh, Y. Hidaka, M. Oda, M. Suzuki, and T. Murakami, "The effect of the heat treatments on the antiferromagnetism in la2cuo4-δ single crystals," *Solid State Communications*, vol. 64, no. 5, pp. 753–756, 1987. [Online]. Available: https://www.sciencedirect.com/science/article/pii/0038109887906934

[94] R. Coldea, S. M. Hayden, G. Aeppli, T. G. Perring, C. D. Frost, T. E. Mason, S.-W. Cheong, and Z. Fisk, "Spin waves and electronic interactions in la_2cuo_4," *Phys. Rev. Lett.*, vol. 86, pp. 5377–5380, Jun 2001. [Online]. Available: https://link.aps.org/doi/10.1103/PhysRevLett.86.5377

[95] S. Uchida, T. Ido, H. Takagi, T. Arima, Y. Tokura, and S. Tajima, "Optical spectra of $la_{2-x}sr_xcuo_4$: Effect of carrier doping on the electronic structure of the cuo_2 plane," *Phys. Rev. B*, vol. 43, pp. 7942–7954, Apr 1991. [Online]. Available: https://link.aps.org/doi/10.1103/PhysRevB.43.7942

[96] M. A. Kastner, R. J. Birgeneau, G. Shirane, and Y. Endoh, "Magnetic, transport, and optical properties of monolayer copper oxides," *Rev. Mod. Phys.*, vol. 70, pp. 897–928, Jul 1998. [Online]. Available: https://link.aps.org/doi/10.1103/RevModPhys.70.897

[97] S. Ono, S. Komiya, and Y. Ando, "Strong charge fluctuations manifested in the high-temperature hall coefficient of high-T_c cuprates," *Phys. Rev. B*, vol. 75, p. 024515, Jan 2007. [Online]. Available: https://link.aps.org/doi/10.1103/PhysRevB.75.024515

[98] W. M. Temmerman, Z. Szotek, and G. Y. Guo, "A local spin-density study of antiferromagnetism in La_2CuO_4 and $YBa_2Cu_3O_6$," *Journal of Physics C: Solid State Physics*, vol. 21, no. 23, p. L867, aug 1988. [Online]. Available: https://dx.doi.org/10.1088/0022-3719/21/23/002

[99] M. T. Czyżyk and G. A. Sawatzky, "Local-density functional and on-site correlations: The electronic structure of La_2CuO_4 and $LaCuO_3$,"

Phys. Rev. B, vol. 49, pp. 14 211–14 228, May 1994. [Online]. Available: https://link.aps.org/doi/10.1103/PhysRevB.49.14211

[100] A. Svane, "Electronic structure of La_2CuO_4 in the self-interaction-corrected density-functional formalism," *Phys. Rev. Lett.*, vol. 68, pp. 1900–1903, Mar 1992. [Online]. Available: https://link.aps.org/doi/10.1103/PhysRevLett.68.1900

[101] K. Shiraishi, A. Oshiyama, N. Shima, T. Nakayama, and H. Kamimura, "Spin-polarized electronic structures of La_2CuO_4," *Solid State Communications*, vol. 66, no. 6, pp. 629–632, 1988. [Online]. Available: https://www.sciencedirect.com/science/article/pii/0038109888902220

[102] T. C. Sterling and D. Reznik, "Effect of the electronic charge gap on LO bond-stretching phonons in undoped La_2CuO_4 calculated using LDA + U," *Phys. Rev. B*, vol. 104, p. 134311, Oct 2021. [Online]. Available: https://link.aps.org/doi/10.1103/PhysRevB.104.134311

[103] R. S. Mulliken, "Electronic population analysis on LCAO–MO molecular wave functions." *The Journal of Chemical Physics*, vol. 23, no. 10, pp. 1833–1840, 10 1955. [Online]. Available: https://doi.org/10.1063/1.1740588

Acknowledgments

"The struggle itself toward the heights is enough to fill a man's heart. One must imagine Sisyphus happy."
— Albert Camus

First and foremost, I thank Cecilia Vona for her supervision of my work. Starting off my work with near-zero experience in the realm of DFT computations, Cecilia always made sure that I not only see the next hurdle, but also make it past it. Without her spending countless hours with me, setting up HPC calculations, figuring out unit cell geometries, validating species files, connecting me to the right group members, working through **k**-point convergence week after week, and explaining every intricacy of hybrid functionals at least five times, this work would never have been possible. Many times have I caught myself, regretting not simply having listened to her advice earlier, and I am glad to have worked so closely with someone I could learn so much from.

Similarly, I must thank Pasquale Pavone, who welcomed me warmly into the group. No matter how busy the schedule, he always found time for working through another tutorial, an issue I had with my computations or with writing my results down. Without his keen eye, this thesis would have fallen much short of the quality it has now.

I owe the opportunity of this thesis to Claudia Draxl, and am grateful for her giving me this opportunity, both as a student and as a developer. Indirectly, she made possible the aid I received from the rest of the research group, most notably Elisa Stephan always helping me out with her meta-GGA implementation.

Of course, special thanks go out to my parents, Marika and Riccardo, without whose unwavering support I could have achieved nothing. Also, I would like to thank Robert Kühnen, who never failed to show me the limits of my tennis abilities.

Selbstständigkeitserklärung

Ich erkläre hiermit, dass ich die vorliegende Arbeit selbstständig verfasst und noch nicht für andere Prüfungen eingereicht habe. Sämtliche Quellen einschließlich Internetquellen, die unverändert oder abgewandelt wiedergegeben werden, insbesondere Quellen für Texte, Grafiken, Tabellen und Bilder, kenntlich gemacht. Mir ist bekannt, dass bei Verstößen gegen diese Grundsätze ein Verfahren wegen Täuschungsversuchs bzw. Täuschung eingeleitet wird.

Berlin den 22. Juli 2025, ...